

FROM WELLBORE TO RESERVOIR GEOMECHANICAL CHARACTERIZATION OF  
NATURALLY FRACTURED RESERVOIRS

A Dissertation

by

WENYU ZHANG

Submitted to the Office of Graduate and Professional Studies of  
Texas A&M University  
in partial fulfillment of the requirements for the degree of

DOCTOR OF PHILOSOPHY

Chair of Committee,	Ding Zhu
Co-Chair of Committee,	Nobuo Morita
Committee Members,	Jihoon Kim
	Frederick M. Chester
Head of Department,	Jeff Spath

December 2018

Major Subject: Petroleum Engineering

Copyright 2018 Wenyu Zhang

## ABSTRACT

In naturally fractured reservoirs, the performance of fractured wells is closely related to in-situ stress state and natural fracture distributions. The anisotropic geomechanical behavior of naturally fractured rock makes it difficult to appropriately evaluate the stress and geomechanical properties of the field. In this study, a wellbore-based, integrated geomechanics-seismic model is proposed aiming to improve stress field prediction and characterization of naturally fractured reservoirs.

The integrated approach, starting from a finite element based geomechanical model, which adopts anisotropic nonlinear elasticity to best capture the physical behavior of fractured rock. It is developed to estimate the current stress field at reservoir-scale. The apertures of natural fractures in the reservoir as well as the stiffness of the reservoir rocks are updated during the simulation. The constraints of the geomechanical model are the wellbore stress conditions and failure in the near wellbore region. To verify the geomechanical model results, the failure predicted by a borehole stability model under the simulated stress condition is compared to the measurement borehole breakouts based on well log interpretations. Comparing to conventional stability model, in which rock mass is assumed to be isotropic, the borehole stability model used in this study considers the elastic anisotropy to provide more reliable local stresses. Seismic anisotropy caused by open fractures is then calculated and serves as another calibration method to improve identifying open natural fractures.

In this work, a field study is presented. Given the estimated fracture spacing and aperture, the wellbore-based, integrated geomechanics-seismic model estimates a more homogenous maximum and minimum horizontal stress magnitude variations throughout the field comparing to an isotropic linear elastic geomechanical model. This also results in a narrower range for the

horizontal stress ratio. The different results in the magnitudes of horizontal stresses will also cause difference in predicted fracture apertures, which results in changes in fracture permeability and porosity in coupled flow-geomechanics reservoir simulation. Eventually, for this field study, the seismic velocity anisotropy is predicted based on the simulated stress condition.

## DEDICATION

To my parents, Min Zhang and Wanghua Zheng

## ACKNOWLEDGEMENTS

I would like to express my deepest gratitude to my advisor, Dr. Ding Zhu, for providing me the opportunity to pursue my Ph.D. studies at Texas A&M University and being incredibly supportive during my research project. Dr. Ding Zhu has been a constant source of inspiration and encouragement. Her invaluable guidance and assistance had significant impacts not only on this dissertation but also on my perception of research as a graduate student.

I would like to give special thanks to my co-advisor, Dr. Nobuo Morita, whose profound knowledge on geomechanics and rock mechanics helped me improve my research project. It is impossible for me to complete this research project successful without his generous support.

I would also like to express my greatest thanks to Dr. Jihoon Kim. His constructive suggestions and insights during my research greatly benefit my research project. His course on numerical methods in rock mechanics has been very helpful for the theoretical part of this study.

I would also like to thank Dr. Frederick M. Chester. His advices provide me the understanding of the fundamental perspectives on rock deformation.

I want to thank Ashley Knorr for helping me conduct six triaxial tests for my research project. My thanks also go to Yuhai Zhou, Jaeyoung Park, Elizabeth Da Silva and Jimmy Jin, my team members on the Tarim project for their collaboration. I also want to thank my colleagues and office mates for their supportive discussions and the time that we shared for the past three years.

## CONTRIBUTORS AND FUNDING SOURCES

This research study was supervised by a dissertation committee consisting of Dr. Ding Zhu (advisor), Dr. Nobuo Morita (co-advisor), and Dr. Jihoon Kim of the Department of Petroleum Engineering, and Dr. Frederick M. Chester of the Department of Geology and Geophysics.

The research project was financially supported by China National Petroleum Corporation (CNPC).

## NOMENCLATURE

$A$	Fracture surface area
$C$	Stiffness tensor
$C_{ij}$	Stiffness tensor in the Voigt notation
$D_{ij}$	Fracture stiffness matrix
$E$	Young's modulus
$F^b$	Body force
$F_{ext}$	External force
$F_{int}$	Internal force
$g$	Gravitational acceleration
$J$	Jacobian matrix
$JCS$	Joint wall compressive strength
$JRC$	Joint surface roughness coefficient
$K$	Stiffness matrix
$K_n$	Fracture normal stiffness
$K_{ni}$	Initial fracture normal stiffness
$K_s$	Fracture shear stiffness
$L_s$	Length of scanned image log
$N^k$	Shape function
$p_w$	Wellbore pressure
$R$	Residual force
$S$	Compliance tensor

$S_{ijkl}$	Forth-order compliance tensor
$\hat{S}_{ijkl}$	Forth-order compliance tensor in the local coordinate system
$\hat{S}_{ijkl}^I$	Intact rock compliance tensor in the local coordinate system
$\hat{S}_{ijkl}^J$	Fracture compliance tensor in the local coordinate system
$S_{ijkl}^0$	Forth-order compliance tensor at the reference state
$s_f$	Fracture spacing
$T$	Traction
$T_1$	Transformation matrix
$T_2$	Transformation matrix
$u$	Displacement
$u^k$	Nodal displacement
$\hat{u}^e$	Element displacement vector
$V_j$	Fracture closure
$V_m$	Maximum fracture closure
$\alpha, \alpha_s$	Fracture dip direction
$\alpha_b$	Borehole dip direction
$\beta, \beta_s$	Fracture inclination angle
$\beta_b$	Borehole inclination angle
$\beta_{ij}$	Direction cosine
$\gamma$	Shear strain
$\delta$	Fracture displacement



$\varepsilon$	Strain
$\varepsilon_{ij}$	Strain
$\theta$	Angle between fractures
$\lambda$	Lame constant
$\mu$	Lame constant
$\rho$	Density
$\sigma$	Stress
$\sigma^b$	Borehole-induced stress
$\sigma_1$	Maximum principal stress
$\sigma_3$	Minimum principal stress
$\sigma_{BCS}$	Stress in the wellbore coordinate system
$\sigma_{GCS}$	Stress in the global coordinate system
$\sigma_{PCS}$	Stress in the principal stress coordinate system
$\sigma_h, \sigma_{h,min}$	Minimum horizontal stress
$\sigma_H, \sigma_{H,max}$	Maximum horizontal stress
$\sigma_i$	Initial stress condition
$\sigma_n$	Normal stress
$\sigma'_n$	Effective normal stress
$\sigma_v$	Vertical stress
$\tau$	Shear stress
$\nu$	Poisson's ratio
$\phi'$	Mobilized friction angle

$\phi_b$

Friction angle

$\phi_r$

Residual friction angle

# TABLE OF CONTENTS

	Page
ABSTRACT .....	ii
DEDICATION .....	iv
ACKNOWLEDGEMENTS .....	v
CONTRIBUTORS AND FUNDING SOURCES .....	vi
NOMENCLATURE .....	vii
TABLE OF CONTENTS .....	xi
LIST OF FIGURES .....	xiii
LIST OF TABLES .....	xvii
CHAPTER I INTRODUCTION AND BACKGROUND .....	1
1.1 Overview and Motivation .....	1
1.2 Objectives and Focuses of the Study .....	3
CHAPTER II LITERATURE REVIEW .....	6
2.1 Experimental Observations and Empirical Models for Fractured Rock .....	6
2.2 Numerical analysis in Geomechanics .....	11
2.2.1 Constitutive equation and material symmetry .....	11
2.2.2 Deformation Analysis of Fractured Rock .....	14
2.3 Wellbore Stability Models .....	18
2.4 Fracture Characterization near Wellbore Using Well Logs .....	20
2.5 Experimental and theoretical studies on influence of fractures on seismic velocities .....	22
CHAPTER III DEVELOPMENT OF INTEGRATED APPROACH FOR GEOMECHANICAL CHARACTERIZATION .....	26
3.1 Equivalent Continuum Method .....	27
3.2 Finite-Element-Based Geomechanical Model .....	31
3.2.1 Finite-element formulation .....	32
3.2.2 Model validation with a single fracture .....	38
3.2.3 Model limitations .....	41
3.3 Wellbore Stability Model in Anisotropic Formations .....	41

3.3.1 Model development .....	41
3.3.2 Model validation .....	43
3.3.3 Model limitations .....	49
3.4 Seismic Velocity Anisotropy .....	49
CHAPTER IV FIELD CASE STUDY .....	52
4.1 Field Introduction.....	52
4.1.1 Geological description and tectonic actives of the Tazhong area.....	52
4.1.2 Experimental results from core samples .....	54
4.2 Well Data Acquisition and Interpretations .....	60
4.3 Reservoir-scale Geomechanical Modeling .....	64
4.3.1 Geostatistical modeling of reservoir properties .....	64
4.3.2 Stress analysis around borehole .....	66
4.3.3 Reservoir geomechanical modeling .....	70
4.3.4 Seismic velocity modeling.....	75
CHAPTER V CONCLUSIONS .....	77
REFERENCES .....	78
APPENDIX A DERIVATION OF STRESS DISTRIBUTION AROUND A BOREHOLE .....	88
APPENDIX B STRESS TRANSFORMATIONS.....	93

## LIST OF FIGURES

	Page
Figure 1.1 – Simulated hydraulic fracture network and fluid pressure in the domain with different horizontal stress anisotropy. Reprinted from Kresse et al. (2011) .....	2
Figure 2.1 – Experimental results on joint normal displacements under normal stresses for different types of rocks. Reprinted from Bandies et al. (1983) .....	8
Figure 2.2 – Material with different planes of symmetry a) Isotropic material. b) Transversely isotropic material. c) and d) Orthotropic material with two or three planes of symmetry. ....	14
Figure 2.3 – Rock mass intersecting with three non-orthogonal fracture sets .....	17
Figure 2.4 – Natural fracture, borehole breakout, and tensile failure identified from FMI. Reprinted from Trice (1999) .....	21
Figure 2.5 – Schematics for fracture spacing. a) Fractures intersecting the wellbore, b) Fractures are parallel to wellbore .....	22
Figure 2.6 – Illustration of shear wave splitting through an anisotropic medium .....	23
Figure 2.7 – a) Comparison of measured and computed velocities as a function of stress in Barre granite. (I) Hydrostatic stress. (II) Velocity in the direction of uniaxial stress. (III) Velocity perpendicular to stress. b) Comparison of measured and computed elastic anisotropy in Barre granite. Reprinted from Nur (1971) .....	24
Figure 3.1 – Workflow for the integrated approach .....	27
Figure 3.2 – Schematics of natural fracture in the global and local coordinate systems .....	28
Figure 3.3 – Illustration of space transformation of an 8-node element from the global coordinate to the transformed coordinate .....	34
Figure 3.4 – Illustration of iteration techniques for nonlinear finite element analysis. a) Full Newton-Raphson method. b) Modified Newton-Raphson method. c) Picard Iteration method. Reprinted from Reddy (2004) .....	38

Figure 3.5 – Simulated and analytical total displacement of the sample with a single fracture under uniaxial loading condition. The Full Newton-Raphson method is used for iteration. ....	40
Figure 3.6 – Simulated and analytical fracture normal displacement under increasing normal stress.....	40
Figure 3.7 –Geometry and model structure for wellbore stability analysis .....	42
Figure 3.8 – Laminated rock sample and differential stress at failure with respect to the inclination angles of the lamination. Reprinted from Saeidi et al. (2014). ....	42
Figure 3.9 – Stress distributions around wellbore in an isotropic formation (a) Comparison of numerical and analytical solutions for stress distribution at the borehole (b) Comparison of numerical and analytical solutions for stress distributions along the y-axis .....	45
Figure 3.10 – Stress distributions at the wellbore in an anisotropic formation (a) Fracture normal stiffness <b><math>Kn = 10 \text{ GPa/m}</math></b> (b) Fracture normal stiffness <b><math>Kn = 5 \text{ GPa/m}</math></b> (c) Fracture normal stiffness <b><math>Kn = 2 \text{ GPa/m}</math></b> and (d) Fracture normal stiffness <b><math>Kn = 1 \text{ GPa/m}</math></b> .....	47
Figure 3.11 – Stress distributions at the wellbore in an anisotropic formation (a) Fracture inclination angle <b><math>\beta = 90^\circ</math></b> (b) Fracture inclination angle <b><math>\beta = 60^\circ</math></b> (c) Fracture inclination angle <b><math>\beta = 30^\circ</math></b> and (d) Fracture inclination angle <b><math>\beta = 0^\circ</math></b> .....	48
Figure 3.12 – Polarization directions of P- and S- waves with respect to wave propagation direction $n$ .....	51
Figure 4.1 – Structure map of the Tazhong area in Tarim Basin and location of the TZ45 block in this field case study. Reprinted from Wang et al. (2013).....	54
Figure 4.2 – Correlation between dynamic and static Young’s Modulus.....	57
Figure 4.3 – Correlation between dynamic and static Poisson’s ratio.....	57
Figure 4.4 – Core sample for triaxial test a) before the test and b) after the test. Specimen dimension: 50 mm in height, 25 mm in diameter Microfracture can be observed in the sample .....	58
Figure 4.5 – Stress-strain curves from triaxial test .....	59
Figure 4.6 – Experimental results on compressive strength of the rock .....	59

Figure 4.7 – Location of Well ZG161 in the TZ45 block of the tight gas carbonate field.....	61
Figure 4.8– a) 6-arm caliper readings, b) sonic velocity logs, c) density log and d) sample image log from interval 6094m-6097m .....	62
Figure 4.9 – Elastic properties interpreted from well logs. a) Young’s modulus and shear modulus at the well, b) Poisson’s ratio and c) rock strength .....	63
Figure 4.10 –Young’s modulus distribution of the TZ45 block .....	64
Figure 4.11 – Shear modulus distribution of the TZ45 block.....	65
Figure 4.12 –Poisson’s ratio distribution of the TZ45 block .....	65
Figure 4.13 – Simulation domain for geomechanical modeling of Well ZG161 with a) top view and b) cross-sectional view .....	66
Figure 4.14 – Examples of natural fractures observed from image logs at intervals 6094m-6097m and 6221m-6224m .....	67
Figure 4.15 – a) ZG161 Breakouts intervals identified from image log showing as red lines. b) Rose diagram showing the azimuth of centers of borehole breakouts, 0° indicates north. ....	68
Figure 4.16 – Projected borehole failure area from simulation result with minimum horizontal stress $\sigma_h = 120MPa$ , maximum horizontal stress $\sigma_h = 130MPa$ , and vertical stress $\sigma_v = 140MPa$ (left) An example of borehole breakout interpretation from image log at interval 6096 m – 6099 m (middle) Caliper Measurement of the borehole at interval 6095 m – 6100 m (right).....	70
Figure 4.17 – Young’s modulus distribution of the simulation domain .....	71
Figure 4.18 – Boundary conditions for the reservoir geomechanical model. The bottom of the model is fixed in the vertical direction, but movement is allowed in the horizontal direction.....	71
Figure 4.19 – a) Simulated maximum effective horizontal stress distribution and b) simulated minimum effective horizontal stress distribution, assuming isotropic elastic formation without effect of natural fractures .....	72
Figure 4.20 – a) Simulated maximum effective horizontal stress distribution and b) simulated minimum effective horizontal stress distribution, assuming anisotropic nonlinear elastic formation with effect of natural fractures .....	72

Figure 4.21 – Comparison of the simulated minimum and maximum horizontal stresses at the well location with and without effect of natural fractures.....	73
Figure 4.22 – Comparison of simulated horizontal stress ratio between the two cases. a) Isotropic elastic formation, b) anisotropic nonlinear elastic formation .....	74
Figure 4.23 – Simulated fracture aperture distribution.....	74
Figure 4.24 – a) Simulated p-wave velocity and b) simulated s-wave velocity throughout the reservoir assuming isotropic elastic formation .....	75
Figure 4.25 – Simulated seismic wave velocities throughout the reservoir assuming anisotropic elastic formation a) fast p-wave velocity, wave propagates parallel to natural fractures b) slow p-wave velocity, wave propagates through natural fractures c) fast s-wave velocity and d) slow s-wave velocity, both s-wave velocities are for wave propagates parallel to natural fractures .....	76
Figure B1 – Illustration of coordinate system transformation from the principal stress coordinate system to the global coordinate system (left), and from the global coordinate system to borehole coordinate system(right).....	94



## LIST OF TABLES

	Page
Table 1 – Input parameters to simulate normal displacement of single fracture under uniaxial loading condition .....	39
Table 2 – Simulation parameters for isotropic formation case .....	45
Table 3 – First set of natural fracture properties .....	47
Table 4 – Second set of natural fracture properties .....	48
Table 5 – Summary of static experimental data of core samples from the field .....	55
Table 6 – Summary of dynamic experimental data of core samples from the field .....	56
Table 7 – Simulation parameters of boundary conditions and intact rock .....	69
Table 8 – Simulation parameters of natural fractures .....	69

# CHAPTER I

## INTRODUCTION AND BACKGROUND

### **1.1 Overview and Motivation**

For naturally fractured formations, optimization of the field development, including well planning and stimulation, and other activities such as water injection and CO<sub>2</sub> sequestration rely on the knowledge of characteristics of the natural fractures since they significantly affect properties of subsurface rock namely, permeability and porosity, elastic moduli, and seismic attributes. Ignoring the impacts of natural fractures can ultimately lead to failure in field operations from exploration stage to production stage.

For drilling practice, mud loss during drilling is often a sign of wellbore hitting natural fractures. In some server cases, when drilling through a fractured formation, borehole shift due to natural fracture is observed (Maury and Zurdo 1996). Near wellbore natural fractures can be visualized through borehole image logs and core samples.

Hydraulic fracturing in naturally fractured reservoirs often resulted in complex fracture network according to microseismic monitoring (Maxwell et al. 2002, Daniels et al. 2007). Using a hydraulic fracturing model that is capable to simulate the interaction between the main fracture and pre-existing natural fractures, Kresse et al. (2011) showed that as horizontal stress anisotropy decreases, the complexity of the fracture network increases as shown in Figure 1.1. Therefore, when designing a fracturing job in naturally fractured reservoirs, knowing the stress field and distribution of natural fractures are essential for the treatment to be carried out at the optimal condition.

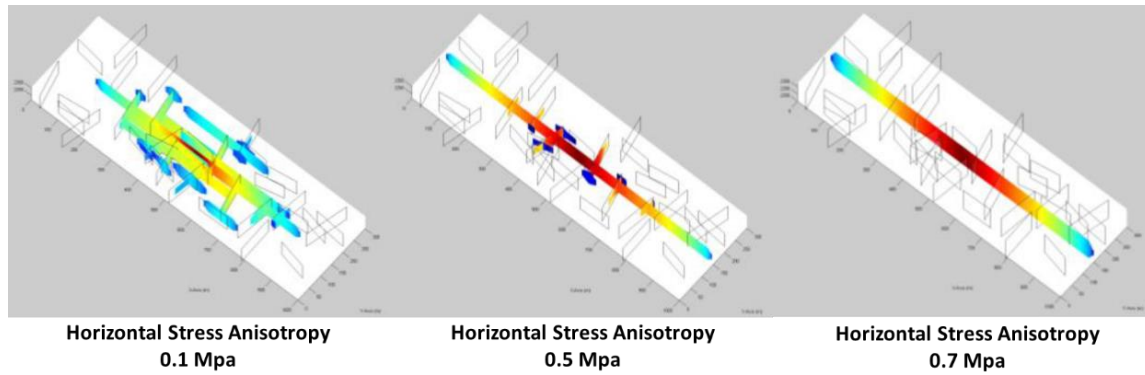


**Figure 1.1 – Simulated hydraulic fracture network and fluid pressure in the domain with different horizontal stress anisotropy. Reprinted from Kresse et al. (2011)**

Advanced flow-geomechanics coupled reservoir models, which capture the stress-induced permeability and porosity change of the in-situ rock, provide the capability of rigorous modeling of fluid flow in naturally fractured reservoirs (Chen and Teufel 1997, Zhao and Chen 2006, Bagheri and Settari 2008). For the coupled reservoir simulation, besides matrix permeability and porosity, fracture permeability and porosity, as well as the in-situ stress conditions, are also required. If we simplify a fracture as two parallel surfaces, then both fracture permeability and fracture void to matrix pore volume ratio are closely related to fracture aperture (Zimmerman 2012).

Due to different depositional environments and tectonic actives, the scale of natural fractures varies from a few centimeters to hundreds of meters. Different sizes of natural fractures can have different impacts and can be characterized by various means. Characterization of natural fractures and their properties is often done by using seismic interpretations, well logs, and experiments on fractured rock samples.

The detection of natural fractures distributed in the formation needs the help of seismic interpretations. Due to the scale of seismic wavelength, small natural fractures may not be detected

from the seismic interpretations (Hudson 1991). In this case, the anisotropic behavior of fractured rock mass which is reflected in the seismic attributes can be used as an alternative interpretation method for natural fracture characterization. Mechanical tests on the fractured rock provide fundamental knowledge of mechanical behaviors of natural fractures. The most prominent finding is the nonlinear stress-displacement relationship. As natural fractures may provide a significant amount of pore space and serve as permeable channel for fluid flow, understanding how fracture deform under stress is critical for reservoir simulation.

When building mathematical models or conducting numerical analyses for naturally fractured reservoirs, the fractures are often categorized as a type of discontinuities in the rock mass. From the numerical simulation perspective, two approaches, discrete or discontinuous method and equivalent continuum method, are generally used. Both approaches account for the nonlinear mechanical behavior of fractured rock mass. The difference is that in the discrete or discontinuous models, fractures are individually or explicitly defined, whereas, in the equivalent continuum models, fracture properties are embedded into the elastic moduli of the bulk rock mass, thus the fractures are implicitly defined.

## **1.2 Objectives and Focuses of the Study**

Many studies regarding the geomechanical characterization of naturally fractured reservoirs are done by only considering the effect of natural fractures in part of the process. The ignorance of any concern while characterizing naturally fractured reservoir can lead to inaccurate interpretations. The focus of this study is to develop a workflow which incorporates analyses of various types of data through different models to improve the reservoir characterization from geomechanical perspective.

In this study, an integrated approach is proposed and presented through a field study on a tight carbonate reservoir. The approach includes three major components: a finite-element-based geomechanical model for estimating the stress distribution of the field and updating the geomechanical properties of the rock in the simulation domain; a wellbore stability model for evaluating maximum horizontal stress through breakout analysis to serve as a constraint of the geomechanical model; and a stress-sensitive rock physics model for predicting the anisotropic seismic velocities of the field.

This thesis is structured into 5 chapters and 2 appendices. Following the introduction, Chapter 2 briefly reviews the experimental studies conducted on the stress-displacement relationships of fractured rock, different approaches for deformation analysis of fractured rocks, wellbore stability model, how to characterize natural fractures using well logs and, finally, the influences of natural fractures on seismic velocities.

Chapter 3 provides details of formulation and development of the three main models used in the integrated approach for geomechanical characterization of naturally fractured reservoir. The limitations of each model is discussed. Both the reservoir-scale geomechanical model and wellbore stability model are established on finite-element method. The method for solving the nonlinear stress-displacement behavior of a fractured rock is also presented in this chapter. The simulated fractured rock compliance from the geomechanical model is used for modeling the anisotropic seismic velocities.

Chapter 4 presents a field application using the integrated model to characterize the natural fractures. Well logs of the selected well and mechanical test results from core samples in the region are interpreted and analyzed as input parameters of the numerical models. Through the analysis of

this field case study, the stress and fracture aperture distributions at the reservoir scale are evaluated.

Appendix A provides the detailed derivation of analytical solution for stress distribution around a hollow cylinder in an anisotropic material. This solution is used to verify simulation results from the wellbore stability model.

Appendix B provides the stress transformation techniques among different coordinate systems. The methods can be used when calculating stresses around a wellbore.

## CHAPTER II

### LITERATURE REVIEW

Subsurface rock mass generally contains discontinuities such as fractures and weak planes which are usually more compliant than the intact rocks. The influence of fractures or joints in the rock mass is significant on the mechanical, transport and seismic properties. The deformation of fractured rock is generally anisotropic and stress-dependent. Different fractures or fracture sets may preserve their own stress-displacement relationships even they are in the same rock mass. The constitutive relationship for a general anisotropic rock mass can be described using Hooke's Law. However, to include the deformation of the fractures in the rock mass, it requires more complex models.

This chapter reviews the experimental investigations on mechanical and seismic behavior of fractured rock, theoretical models for fractured rock deformation analysis and natural fracture characterization methods at the wellbore.

#### **2.1 Experimental Observations and Empirical Models for Fractured Rock**

Experimental studies on jointed rocks provide fundamental knowledge of mechanical behavior of fractured rock. For rock mass with predominate fracture or fracture sets, the most prominent finding is the nonlinear stress-displacement relationship which is usually described by fracture stiffnesses. As in many cases, microfractures are randomly distributed in the rock mass, and the orientations of these microfractures are usually arbitrary. Rocks containing these features usually do not exhibit anisotropic mechanical behavior as observed from the rock with major fracture or fracture set.

The normal deformation of fractured rock was studied by Goodman (1976). From his observations, a power law function was proposed to approximate the relationship of fracture normal stress and displacement as shown in Equation 2.1.

$$V_j = V_m - (V_m \sigma_i) \frac{1}{\sigma_n} \quad (2.1)$$

where  $V_j$  is the fracture normal displacement,  $V_m$  is the maximum fracture normal displacement,  $\sigma_n$  is the normal stress applied on fracture surfaces, and  $\sigma_i$  is the initial stress level.

Bandis et al. (1983) concluded that a hyperbolic function for normal stress-closure relationship which fits better to his laboratory investigations of normal deformability on a number of different rock types and joint conditions as shown in Figure 2.1. The development of the hyperbolic function by Bandis et al. is briefly summarized below,

$$\sigma_n = \frac{V_j}{a - bV_j} \quad (2.2)$$

where  $V_j$  is the fracture normal displacement, and  $a$  and  $b$  are constants. Rearrange Equation 2.2 we have,

$$\sigma_n = \frac{1}{\frac{a}{V_j} - b} \quad (2.3)$$

When normal stress is very large, the fracture closure  $V_j$  should reach its maximum value  $V_m$ , this implies,

$$\frac{a}{b} = V_m \quad (2.4)$$

On the other hand, when normal stress is extremely small, the fracture closure  $V_j$  should tend to be zero, giving,



$$K_n = \frac{1}{a} = K_{ni} \quad (2.5)$$

where  $K_{ni}$  is the initial fracture normal stiffness. If we define fracture normal stiffness as the ratio of change of normal stress to normal closure,

$$K_n = \frac{\partial \sigma_n}{\partial V_j} \quad (2.6)$$

inserting Equation 2.3 into the above equation,

$$K_n = \frac{\partial \sigma_n}{\partial V_j} = \frac{1}{a \left(1 - \frac{b}{a} V_j\right)^2} = \frac{K_{ni}}{\left(1 - \frac{V_j}{V_m}\right)^2} \quad (2.7)$$

By substitution of  $V_j$  as:

$$V_j = \frac{a \sigma_n}{1 + a \sigma_n} = \frac{V_m \sigma_n}{K_{ni} V_m + \sigma_n} \quad (2.8)$$

Equation 2.7 becomes:

$$K_n = K_{ni} \left[ 1 - \frac{\sigma_n}{K_{ni} V_m + \sigma_n} \right]^{-2} \quad (2.9)$$

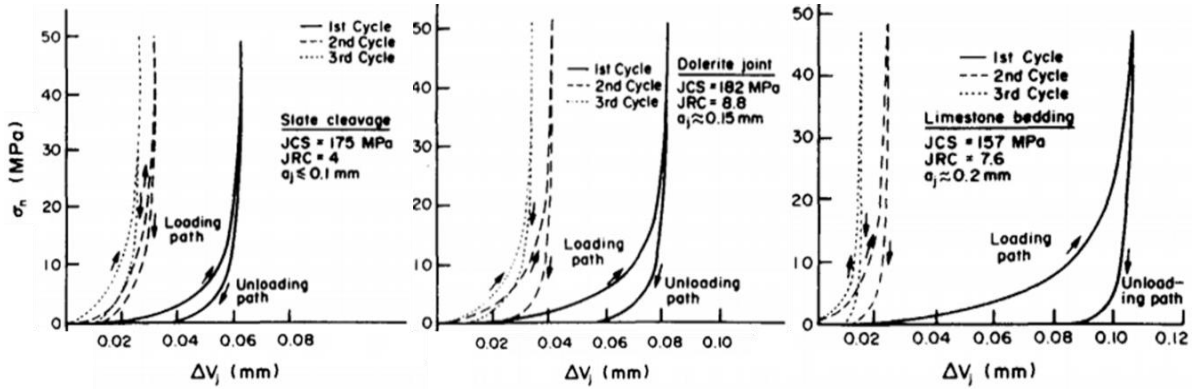


**Figure 2.1 – Experimental results on joint normal displacements under normal stresses for different types of rocks. Reprinted from Bandies et al. (1983)**

Both normal stress-displacement models by Goodman and Bandis et al. were empirical correlations developed by best fitting experimental data under certain conditions. On the other hand, models based on principles of contact theory where stiffness of fracture is derived from Hertz or Mindlin contact theories were also developed (Greenwood and Williamson 1966, Brown and Scholz 1985, Yoshioka and Scholz 1989, Mirsa 1999). Based on Hertz or Mindlin theories, the fracture surface profile is characterized by a distribution function, the force is then summed among the contacting asperities during the fracture closure by assuming either elastic or plastic deformation. The displacement of the fracture is solved when the force reaches the equilibrium.

The investigation of peak shear strength criteria was conducted by Patton (1966) on simplified fracture surface geometries. Patton concluded that the shear strength for a smooth joint is governed by the basic friction angle and for a saw-tooth joint, it is determined by the effective friction angle under low normal stress.

Based on Patton's work, Ladanyi and Archambault (1969) proposed an improved model by considering simultaneous sliding and shearing mechanics of a joint. The model was derived from energy conservation where the total shear force is a summation of three components: external work done in dilating against the normal force; additional internal work in friction due to dilatancy; and work done in internal friction. The general form of shear strength in this model is expressed as a function of the rate of dilation, the average friction angle, and shear area ratio.

Barton (1973) developed a peak shear strength criterion based on shear deformation behavior of the fracture with experimental results of direct shear test on fractures with various smoothness. The peak shear strength is defined by using an empirical correlation as,

$$\tau = \sigma_n \tan[JRC \log\left(\frac{JCS}{\sigma_n}\right) + \phi_b] \quad (2.10)$$

where  $JRC$  is the joint surface roughness coefficient,  $JCS$  is the joint wall compressive strength, and  $\phi_b$  is the friction angle. However, the model has limited applications because the determination on surface roughness coefficient  $JRC$  is subjective and a single  $JRC$  value may not be representative for the entire joint profile by neglecting the localized roughness (Karami and Stread 2008).

The shear deformation mechanics of a joint are generally divided into three groups (Karami and Stread 2008), the Coulomb friction model, the Barton-Bandis model (Barton et al. 1985) and the continuously yielding model (Cundall and Lemos 1988).

The Coulomb friction model assumes the joint is elastic-perfectly-plastic, where deformation of the joint is linear in both elastic and plastic deformation regimes. The Coulomb friction model is most suitable for joint has smooth joint surface and minimized dilation behavior.

Barton et al. (1985) introduced a relationship between the mobilized surface roughness  $JRC$  and the mobilized friction angle,

$$\phi'(mob) = JRC(mob) \log\left(\frac{JCS}{\sigma_n}\right) + \phi_r \quad (2.11)$$

where  $\phi_r$  is the residual friction angle. Based on the ratio of mobilized and peak  $JRC$  values the model predicts a nonlinear response of shear stress and shear displacement of a joint.

$$\frac{JRC(mob)}{JRC(peak)} = \frac{\phi'(mob) - \phi_r}{\phi'(peak) - \phi_r} \quad (2.12)$$

Cundall and Lemos (1988) proposed a continuous yielding model in which the normal and shear mechanical behaviors of a joint are both nonlinear. The model considers the progressive damage of the joint asperities under plastic shear deformation.

## 2.2 Numerical analysis in Geomechanics

### 2.2.1 Constitutive equation and material symmetry

In this section, the constitutive equations for linear elastic rock with different material symmetries are presented in the form of Hooke's law.

$$\sigma = C\varepsilon \quad (2.13)$$

or

$$\varepsilon = S\sigma \quad (2.14)$$

where  $\sigma$  is the stress,  $\varepsilon$  is the strain,  $C$  is the stiffness or elasticity tensor, and  $S$  is the compliance tensor. In three-dimensional space, stress and strain are defined by second-order tensors containing 9 elements. The stiffness and compliance of the rock are forth-order tensors containing 81 elements. Due to the symmetry of the stress and strain tensors, the generalized Hooke's law expression,

$$\sigma_{ij} = C_{ijkl}\varepsilon_{kl} \quad (2.15)$$

can be simplified by using Voigt notation, where the stress and strain are reduced from 9-element second-order tensors to 6-element vectors, and stiffness and compliance tensors are now reduced from 81-element fourth-order tensors to 6 by 6 matrices,

$$\sigma_i = C_{ij}\varepsilon_j \quad (2.16)$$

or in matrix form,

$$\begin{bmatrix} \sigma_1 \\ \sigma_2 \\ \sigma_3 \\ \sigma_4 \\ \sigma_5 \\ \sigma_6 \end{bmatrix} = \begin{bmatrix} C_{11} & C_{12} & C_{13} & C_{14} & C_{15} & C_{16} \\ C_{21} & C_{22} & C_{23} & C_{24} & C_{25} & C_{26} \\ C_{31} & C_{32} & C_{33} & C_{34} & C_{35} & C_{36} \\ C_{41} & C_{42} & C_{43} & C_{44} & C_{45} & C_{46} \\ C_{51} & C_{52} & C_{53} & C_{54} & C_{55} & C_{56} \\ C_{61} & C_{62} & C_{63} & C_{64} & C_{65} & C_{66} \end{bmatrix} \begin{bmatrix} \varepsilon_1 \\ \varepsilon_2 \\ \varepsilon_3 \\ \varepsilon_4 \\ \varepsilon_5 \\ \varepsilon_6 \end{bmatrix} \quad (2.17)$$

where the subscript in the Voigt notation as in Equation 2.17 can be converted to the fourth rank tensor subscripts in the following order:  $()_1$  represents  $()_{11}$ ,  $()_2$  represents  $()_{22}$ ,  $()_3$  represents  $()_{33}$ ,  $()_4$  represents  $()_{23}$ ,  $()_5$  represents  $()_{13}$ , and  $()_6$  represents  $()_{12}$ .

For an isotropic material, the elastic moduli do not show azimuthal difference. The components in stiffness and compliance tensors can be expressed using Young's modulus  $E$  and Poisson's ratio  $\nu$ ,

$$\begin{bmatrix} \varepsilon_1 \\ \varepsilon_2 \\ \varepsilon_3 \\ \varepsilon_4 \\ \varepsilon_5 \\ \varepsilon_6 \end{bmatrix} = \frac{1}{E} \begin{bmatrix} 1 & -\nu & -\nu & 0 & 0 & 0 \\ -\nu & 1 & -\nu & 0 & 0 & 0 \\ -\nu & -\nu & 1 & 0 & 0 & 0 \\ 0 & 0 & 0 & 2(1+\nu) & 0 & 0 \\ 0 & 0 & 0 & 0 & 2(1+\nu) & 0 \\ 0 & 0 & 0 & 0 & 0 & 2(1+\nu) \end{bmatrix} \begin{bmatrix} \sigma_1 \\ \sigma_2 \\ \sigma_3 \\ \sigma_4 \\ \sigma_5 \\ \sigma_6 \end{bmatrix} \quad (2.18)$$

In real field applications, it is unusual to find rock mass that is isotropic. However, common material symmetries, such as, transversely isotropic and orthotropic provide simple and relatively accurate assumption for geomechanical analysis. As the number of planes of symmetry increases as shown in Figure 2.2, the independent components in the stiffness or compliance tensor increase.

The transversely isotropic materials usually contain one plane of symmetry in a representative rock volume. The Young's modulus and the Poisson's ratio values are different in the directions normal (in the  $e_3$  direction) and parallel (in the  $e_1$  and  $e_2$  direction) to the plane of symmetry. In this case, the constitutive equation can be expressed as,

$$\begin{bmatrix} \varepsilon_1 \\ \varepsilon_2 \\ \varepsilon_3 \\ \varepsilon_4 \\ \varepsilon_5 \\ \varepsilon_6 \end{bmatrix} = \begin{bmatrix} \frac{1}{E_1} & -\frac{\nu_{12}}{E_1} & -\frac{\nu_{13}}{E_3} & 0 & 0 & 0 \\ -\frac{\nu_{12}}{E_1} & \frac{1}{E_1} & -\frac{\nu_{13}}{E_3} & 0 & 0 & 0 \\ -\frac{\nu_{13}}{E_1} & -\frac{\nu_{13}}{E_3} & \frac{1}{E_3} & 0 & 0 & 0 \\ 0 & 0 & 0 & \frac{1}{G_{13}} & 0 & 0 \\ 0 & 0 & 0 & 0 & \frac{1}{G_{13}} & 0 \\ 0 & 0 & 0 & 0 & 0 & \frac{1}{G_{12}} \end{bmatrix} \begin{bmatrix} \sigma_1 \\ \sigma_2 \\ \sigma_3 \\ \sigma_4 \\ \sigma_5 \\ \sigma_6 \end{bmatrix} \quad (2.19)$$

The orthotropic material contains two to three planes of symmetry which makes nine independent elastic constants in the compliance tensor. With three planes of symmetry, the stress-strain relation is expressed as,

$$\begin{bmatrix} \varepsilon_1 \\ \varepsilon_2 \\ \varepsilon_3 \\ \varepsilon_4 \\ \varepsilon_5 \\ \varepsilon_6 \end{bmatrix} = \begin{bmatrix} \frac{1}{E_1} & -\frac{\nu_{12}}{E_2} & -\frac{\nu_{13}}{E_3} & 0 & 0 & 0 \\ -\frac{\nu_{12}}{E_1} & \frac{1}{E_2} & -\frac{\nu_{23}}{E_3} & 0 & 0 & 0 \\ -\frac{\nu_{13}}{E_1} & -\frac{\nu_{23}}{E_2} & \frac{1}{E_3} & 0 & 0 & 0 \\ 0 & 0 & 0 & \frac{1}{G_{23}} & 0 & 0 \\ 0 & 0 & 0 & 0 & \frac{1}{G_{13}} & 0 \\ 0 & 0 & 0 & 0 & 0 & \frac{1}{G_{12}} \end{bmatrix} \begin{bmatrix} \sigma_1 \\ \sigma_2 \\ \sigma_3 \\ \sigma_4 \\ \sigma_5 \\ \sigma_6 \end{bmatrix} \quad (2.20)$$

Different types of material symmetries form the common anisotropy usually observed in geomechanical analyses. They also provide insights into mathematical models developed for deformation analysis of fractured rock as described in the next section.

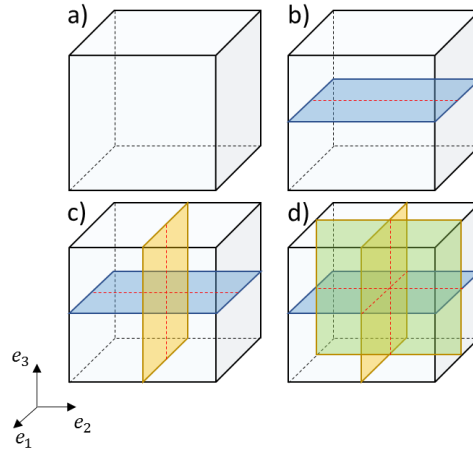


**Figure 2.2 – Material with different planes of symmetry a) Isotropic material. b) Transversely isotropic material. c) and d) Orthotropic material with two or three planes of symmetry.**

### 2.2.2 Deformation Analysis of Fractured Rock

Solutions for fractured rock deformation are usually divided into two categories: the discontinuous methods or the continuum-based methods. The former approach explicitly defines each individual fracture in the model domain and simulates the displacements of each fracture. On the other hand, the latter solution embeds the fracture properties into an equivalent continuum where the entire fractured rock mass is treated as a continuous body with modified properties.

Both discontinuous models and continuum-based models have their own advantages. Due to the discrete nature of fractured rock, the discontinuous models provide more accurate simulation results if the distributions of the fracture size, density, and orientations are arbitrary. However, the implementation of individual fractures into the simulation domain and the computational cost of the solution can be very expensive. The continuum-based analyses are more suitable for rock mass with persistent fracture sets that share similar properties. In addition, since the mechanical behavior

of the fractures are not simulated separately, the computation is greatly reduced compared to the discontinuous methods.

#### Discrete or discontinuous methods

In the numerical analysis using discrete approach, the discontinuities in the simulation domain are explicitly discretized with special elements. The discontinuous methods include the discrete element method (DEM) and discontinuous deformation analysis (DDA). These numerical schemes are used to simulate the deformation of rock mass containing arbitrarily distributed discontinuities.

Discrete element method is usually used when targeting small-scale problems from nanoscopic ( $\sim 10^{-9}$  m) to mesoscopic scale ( $\sim 10^{-4}$  m) since the length scale of interest is at the same order of magnitude as the discontinuity spacing (Jebahi et al. 2015). The concept was originally proposed by Cundall (1971) to solve rock mechanical problems. Cundall and Strack (1979) expanded the model to perform the deformation analysis of granular assemblies. Williams and Mustoe (1993) extended the use of the discrete element method from mainly granular particles to blocky particles. More recently, attempts for large-scale simulation using discrete element method with improved computational algorithms can be found in Cook and Jensen (2002).

Discontinuous deformation analysis is a special type of discrete element method where the mathematical formulation is based on the work-energy method and the principle of minimum potential energy. The concept is originally proposed by Shi and Goodman (1984, 1985) with first acquire known displacements and strains of the material at individual locations and perform the deformation analysis through best least square fit overall displacements, strains of each rock block and discontinuities. Shi (1988) expanded the concept and accommodate the model with



constitutive equations to provide a forward discontinuous deformation modeling approach. The difference between the discrete element method and discontinuous deformation analysis is that the former approach is a force method that attempts to adjust the contact forces to be constants and the latter is a displacement approach that the solutions in the equilibrium equations are for the unknown displacements (Yossef et al. 2018).

#### Continuum-based methods

Analytical solutions were derived for some simplified fractured rock geometries featuring certain elasticity symmetries. Most of the solutions provide closed-form expressions for the elastic constants that form the constitutive equation.

Amadei and Goodman (1981a), Gerrard (1982), and Yoshinaka and Yamabe (1986) developed analytical solutions to obtain the equivalent elastic constants for up to 3 sets of perpendicular fractures. In their models, the fractures are assumed to be planar and aligned to the axes in the global coordinate system. The fractures can have any width and can have general properties. Using this model, Amadei and Goodman (1981b) investigated the stress distribution of around a circular hole intersecting parallel fractures by using a general plane strain assumption for anisotropic rock mass where fracture normal and shear stiffnesses are incorporated into the constitutive relations.

The closed-formed expressions for elastic moduli of a rock mass intersecting with three sets of non-orthogonal fractures as shown in Figure 2.3 are developed by Huang et al. (1995) based on slip concept of discontinuities in fractured rock mass. The constitutive constants contain the elastic moduli of the intact rock, stiffnesses for each set of fracture, and angle between fracture

sets. Equation 2.21 shows the elastic modulus in z-direction under uniaxial test assuming the fractures have the same stiffnesses  $K_n$  and  $K_s$ ,

$$\frac{1}{\bar{E}_z} = 2 \cos^2\left(\frac{\theta}{2}\right) \left( \frac{\sin^2\left(\frac{\theta}{2}\right) K_n + \cos^2\left(\frac{\theta}{2}\right) K_s}{K_n K_s s_f} \right) - \frac{\sin(\theta) \lambda_{di}}{2 K_s s_f} + \frac{1}{E_0} \quad (2.21)$$

where  $\bar{E}_z$  is the equivalent Young's modulus of the fractured rock in the z-direction,  $E_0$  is the Young's modulus of the intact rock,  $\theta$  is the angle between two non-orthogonal fracture sets,  $s_f$  is the fracture spacing and  $\lambda_{di}$  is the dilatancy coefficient.

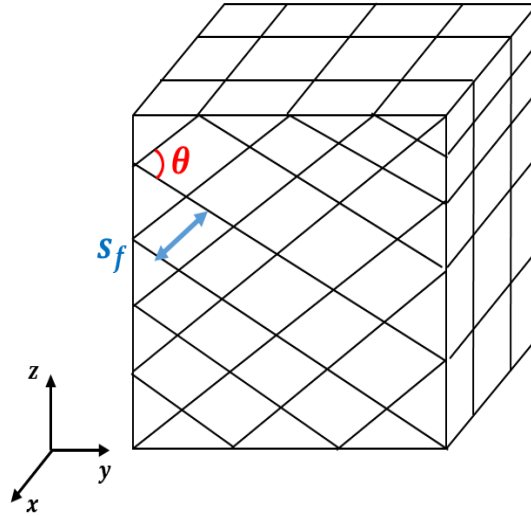


**Figure 2.3 – Rock mass intersecting with three non-orthogonal fracture sets**

To conduct the numerical analysis using equivalent continuum method, an equivalent continuum constitutive model needs to be established for fractured rock mass. The stress-strain relationship of the continuum can be developed based on either the concept of average strain energy density for an inhomogeneous elastic body (Singh 1973, Cai and Horii 1992), or the principle of conservation of energy for the work done by an external force on an elastic body

(Huang et al. 1985). The implementation of finite element scheme that incorporating the concept of equivalent continuum approach was introduced by Zienkiewicz and Pande (1977) for multilaminated rocks. The advantage of employing equivalent continuum concept into finite element analysis is that the model mesh construction is now independent of the locations of the discontinuities. The conventional approach to ensure the simulation accuracy by refining the mesh around the fractures is not required anymore. It significantly improved the computational efficiency without compromising the reliability of the simulation results.

### **2.3 Wellbore Stability Models**

Borehole instability occurs when the stress condition is altered by removing the rock mass and filling with drilling mud during the drilling operation. The stress concentration results in compressive shear failure around the wellbore region when the elevated stress exceeds the rock strength. The stress concentration around the wellbore depends on several factors including the magnitude and direction in-situ stresses, the mud pressure, well inclination and azimuth.

Depending on the severe level, borehole instability can result in stuck pipe or collapse of the wellbore as reported in numerous studies (Bell and Gough 1979, Plumb and Hickman 1985, Zoback et al. 1985, Peska and Zoback 1995). In naturally fractured formations, borehole shift along the discontinuous planes is observed (Maury and Zurdo 1996). Wellbore image and caliper logs are the most common tools to detect borehole breakouts.

To prevent the borehole instability issues, models were developed to understand the cause of the failure around wellbore and predict the scale of breakouts. Bradley (1979) proposed a borehole failure model with assumptions that the rock is linear elastic and the flow of fluid into or out of the formation is neglected. In this work, analytical solutions for the stresses at the wellbore

and into the formation were provided based on Kirsch's solution (1898) together with Fairhurst solution (1968). Zoback et al. (1985) adopted the similar approach but suggested using Coulomb-Navier failure criterion for breakout initiation.

Detournay and Cheng (1988) developed analytical solutions of the stress, displacement, and pore pressure field around a vertical borehole by accounting for the presence of pore fluid and poroelastic response of the formation. They concluded that the shear failure could be initiated inside the formation rock instead of at the borehole wall. Cui et al. (1997) presented an analytical solution of stress for an inclined borehole in poroelastic formation under the assumption of generalized plane-strain condition.

For formations contain discontinuities such as natural fractures and weak bedding planes, the conventional wellbore stability models for isotropic formations may yield inaccurate stress evaluation and breakout predictions due to anisotropic rock strength and the stress perturbation from the discontinuities.

Lekhnitskii (1963) and Amadei (1983) provided analytical solutions of the stress around a borehole with arbitrary orientation in an anisotropic formation by adopting generalized plane-strain assumption. Based on the analytical solution, Aadnoy (1988) investigated the wellbore instability issues in anisotropic formation and concluded that directional elastic properties are important factors on the failure at wellbore and the conventional isotropic wellbore stability model fails to take account into account anisotropic rock behavior. Ong and Roegiers (1993) extended Aadnoy's model by adopting a generalized three-dimensional anisotropic failure criterion together with the stress solution for a borehole in anisotropic formation. Zhang et al. (2003) presented a numerical solution for borehole stability analysis in naturally fractured formation by considering the formation rock as a dual-porosity poroelastic media.

Lee et al. (2012) improved previous models by considering the influence of weak plane on the failure regions around the well. In their model, the failure along the weak plane is evaluated separately using the projected normal and shear stresses on the weak plane. Liu et al. (2016) further improved Lee et al.'s model by taking poroelastic anisotropy into consideration.

Even though wellbore stability models are originally developed for predicting the occurrence of borehole breakouts and drilling-induced fracture, the models can also serve as an indicator of in-situ stress. Through borehole stability analysis, stresses can be calculated and calibrated by comparing the simulated wellbore failure and breakouts or drilling induced fractures observed and measured from the well logs. When modeling in-situ stresses of a field through a reservoir-scale geomechanical model, well measured or interpreted stress data are often served as constraints for the geomechanical model.

## **2.4 Fracture Characterization near Wellbore Using Well Logs**

Natural fractures can be characterized at borehole location directly from core samples or indirectly through log interpretations, including utilizing borehole imagers, such as microresistivity formation imager or ultrasonic borehole imager and conventional well logs such as resistivity logs. Log interpretations can be used to determine fracture spacing, fracture orientation and fracture aperture. The borehole image log not only can identify natural fractures at wellbore, information such as borehole breakouts and drilling-induced fractures as shown in Figure 2.4 are also valuable in interpreting orientations and estimating magnitudes of in-situ principal stresses. Practices using image logs to characterize near-wellbore natural fractures and build local stress models have been widely conducted throughout the world (Zoback et al., 1985; Trice, 1999; Makel, 2007; Ameen et al., 2012).

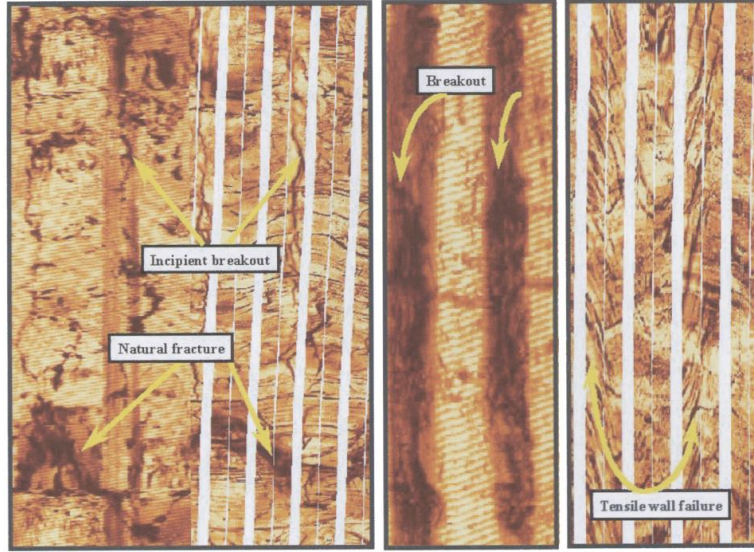


**Figure 2.4 – Natural fracture, borehole breakout, and tensile failure identified from FMI.  
Reprinted from Trice (1999)**

The spacing of natural fractures can be calculated from image logs if the fracture frequency and dip angle are known. Terzaghi (1965) introduced the concept of the “shadow zone” to correct the diminishing fracture frequency as the scan line approaching the strikes of the natural fractures,

$$s_f = \frac{L_s \sin(\beta)}{N} \quad (2.22)$$

where  $L_s$  is the length of scanned image log,  $\beta$  is the angle between the wellbore and fracture dip direction, and  $N$  is the number of fractures intersected with the wellbore as shown in Figure 2.5. As we notice, the above correction has limitation when  $\beta$  is approaching zero. The fracture spacing estimation becomes severely affected. Priest (1993) modified Terzaghi’s method by limiting the correction size to a minimum  $\beta$  of  $5.7^\circ$ .

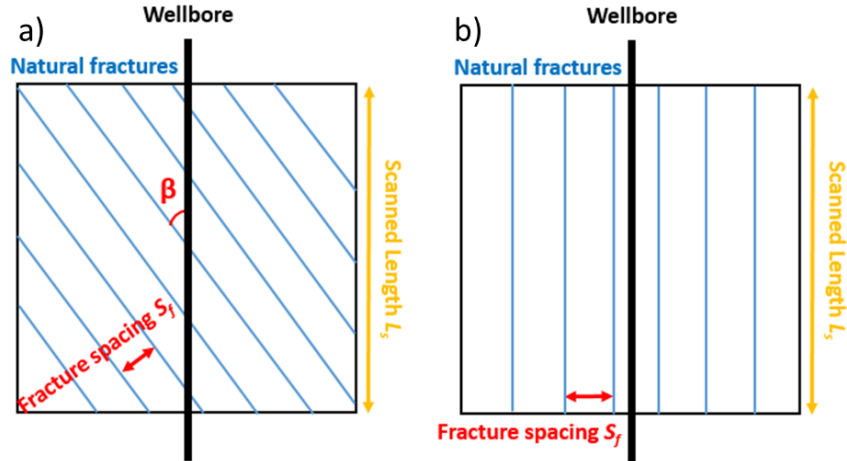


**Figure 2.5 – Schematics for fracture spacing. a) Fractures intersecting the wellbore, b) Fractures are parallel to wellbore**

Fracture aperture is also of great importance in evaluating fracture porosity and permeability. Luthi and Souhaite (1990) combined 3D finite element modeling and using image log and resistivity log measurements to determine the fracture aperture, where fracture aperture can be calculated using the formation resistivity, mud resistivity, current received by the formation microscanner as the scanner moves across a fracture.

## **2.5 Experimental and theoretical studies on influence of fractures on seismic velocities**

Seismic wave propagation through porous media is a stress-dependent process. Nur and Simmons (1969) investigated the response of a granite rock sample under uniaxial loading to seismic wave velocity anisotropy. The experimental results showed that the compressional waves travel fastest in the direction of the applied stress, whereas, the two shear waves have different velocities in any orientation, indicating shear wave splitting as shown in Figure 2.6.

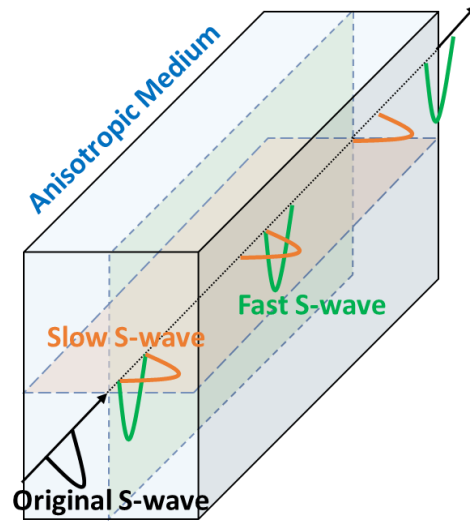


**Figure 2.6 – Illustration of shear wave splitting through an anisotropic medium**

Nur (1971) developed a theoretical model in aggregates with joints assuming penny-shaped pre-existing fractures to determine the velocities of the waves traveling through a jointed rock sample under arbitrary loadings. The effects of fracture distribution in the rock and nonhydrostatic loadings on the sample on seismic velocities were studied. The velocities that were calculated uniquely from the fracture distribution compares well with experimental results of compressional and shear velocities in granite samples as shown in Figure 2.7.



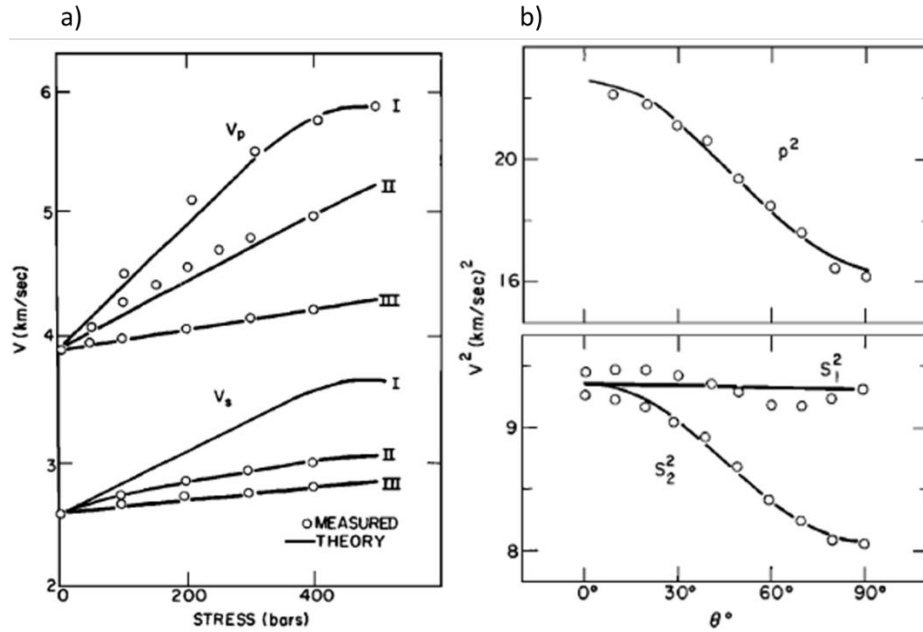


**Figure 2.7 – a) Comparison of measured and computed velocities as a function of stress in Barre granite. (I) Hydrostatic stress. (II) Velocity in the direction of uniaxial stress. (III) Velocity perpendicular to stress. b) Comparison of measured and computed elastic anisotropy in Barre granite. Reprinted from Nur (1971)**

The development of seismic wave velocity models based on stress-induced elastic anisotropy of jointed solids were done by O'Connell and Budiansky (1974), Henyey and Pomphrey (1982), and Hudson (1980, 1981). In their models, the fracture is assumed to be penny-shaped and parameters of each fracture need to be provided individually into the model formula. These models are generally not practical when fracture density is high, and it is not common to take measurements of each individual fracture in a rock sample.

For rock mass contains more than one set of parallel fractures, Sayers and Kachanov (1991) presented a relatively simpler scheme for obtaining the effective elastic properties of jointed rock with arbitrary fracture orientations and finite fracture densities through tensor transformation of elastic constants. In this model, the fractures are assumed to be penny-shaped, and the knowledge of the symmetry of anisotropy rock mass is not a prerequisite.

Mavko et al. (1995) developed a model for the stress-induced velocity change in rock mass containing arbitrary fracture geometries and orientations based on measured values of compressional and shear wave velocities through the isotropic intact rock. This model provides a more general solution for anisotropic wave velocity analysis since the fractures are not limited to penny-shaped and the fracture density can be arbitrarily defined. It also provides an invert method for the distribution of fractures given the fracture shape and aspect ratio.

$$S_{ijkl}(\tilde{\sigma}) = S_{ijkl}^0 + \Delta S_{ijkl} \quad (2.23)$$

where  $S_{ijkl}(\tilde{\sigma})$  is the compliance of the fractured rock at a given stress state  $\tilde{\sigma}$ ,  $S_{ijkl}^0$  is the reference compliance at a large confining pressure, and  $\Delta S_{ijkl}$  is the incremental compliance due to the stress change, which can be expressed using the fracture void space to rock volume ratio  $\bar{\phi}_c$  and compliance  $\bar{S}_{ijkl}^J$  of the fracture set at the current stress state,

Similarly, Schoenberg and Sayers (1995) and Sayers (2002) developed a rock physics model using effective compliance of the fractured rock as the sum of the compliance of the unfractured intact rock and each set of parallel fractures. Different from the method proposed by Mavko et al., instead of using fracture void space change, the compliance of the fractured rock is derived from the normal and shear compliances  $K_n$  and  $K_s$  of the fracture sets.

Prioul et al. (2004) developed a nonlinear rock physics model for predicting seismic velocities in a transverse isotropic rock mass under three-dimensional stress condition without the prerequisite of wave velocities in isotropic rocks. This model utilizes the third-order elasticity constants. However, the model is limited to a small range of stress change due to the linear relation between the elastic stiffness tensor and stress variations. If large stress change is implemented, stress-sensitivity coefficients that are a function of stress need to be used (Prioul and Lebrat 2004).

# CHAPTER III

## DEVELOPMENT OF INTEGRATED APPROACH FOR GEOMECHANICAL CHARACTERIZATION\*

The integrated approach for geomechanical characterization starts with the geomechanical model, then a wellbore stability model is used to provide constraints for the geomechanical model results. Finally, the seismic attributes, which in this study is the wave velocities, are evaluated based on the simulated rock elastic properties and stress distribution of the field through a stress-sensitive rock physics model. The workflow of the approach is presented in Figure 3.1.

Modeling the deformation and stress distribution of the fractured medium adopts the equivalent continuum method. The nonlinear behavior of the fracture stress-displacement relation is based on the correlation proposed by Bandis et al. (1983). The Full Newton-Raphson iteration is used for finding the solution. For borehole stability analysis in an anisotropic formation, a numerical model is built which is verified with the analytical solutions proposed by Lekhnitskii (1963).

---

\* Part of this dissertation is reprinted with permission from “From Wellbore to Seismic: An Integrated Approach for Geomechanical Characterization of Naturally Fractured Reservoirs” by Zhang, W., Zhu, D. and Kim, J., 2018: Paper SPE-191867-MS Presented at the SPE Argentina Exploration and Production of Unconventional Resources Symposium in Neuquen, Argentina, 14-16 August 2018. Copyright 2018 by the Society of Petroleum Engineers.

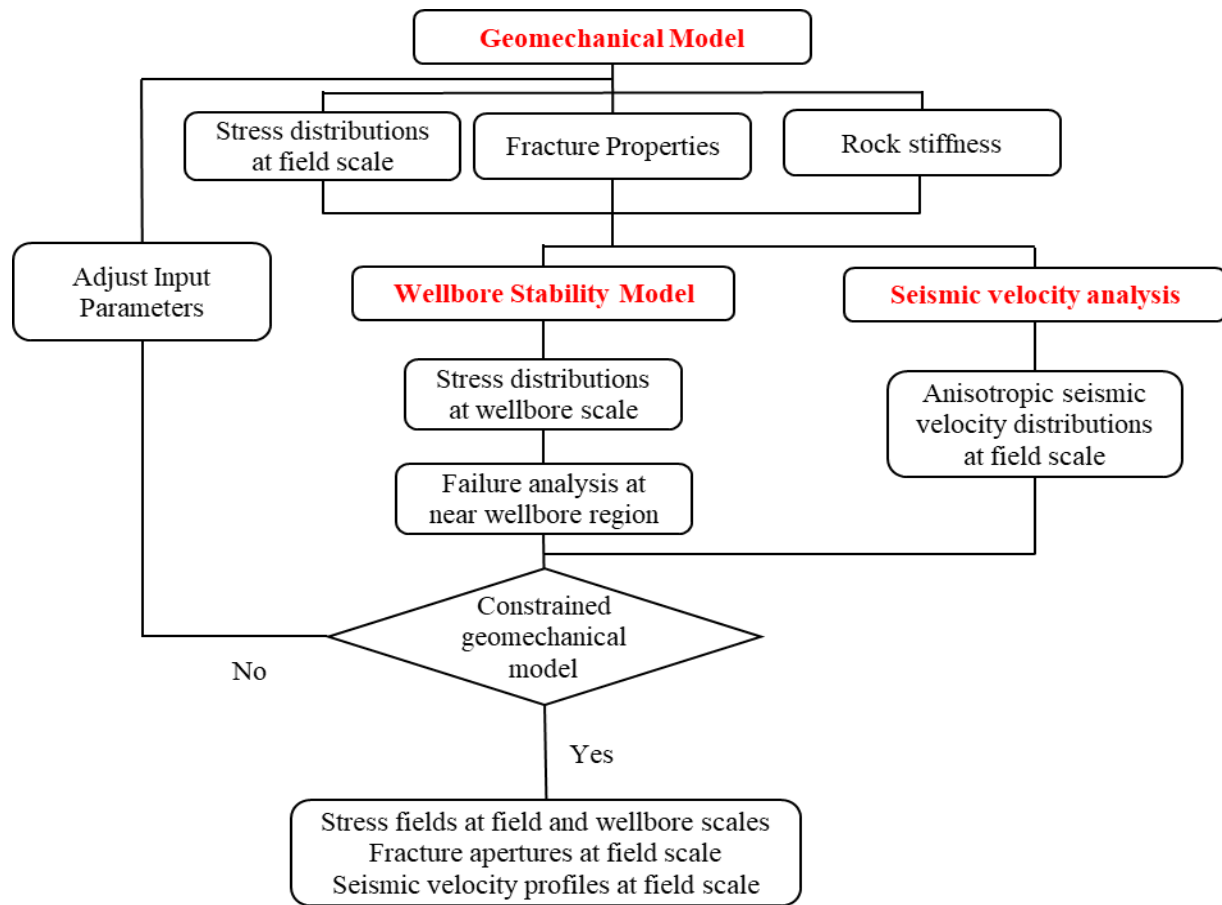


**Figure 3.1 – Workflow for the integrated approach**

### 3.1 Equivalent Continuum Method

The equivalent continuum method is designed to solve the constitutive relation of a material containing discontinuities that cause elastic anisotropy. The stress-strain relation for an elastic material is defined by Hooke's Law as described in Chapter II. In this section, two coordinate systems are introduced. As presented in Figure 3.2, the global coordinate system refers to the  $xyz$  coordinates that representing the bulk rock mass; whereas, the local coordinate system refers to the  $e_1e_2e_3$  coordinates where  $e_1$  and  $e_2$  are parallel to the fracture plane, and  $e_3$  is normal to the fracture plane.

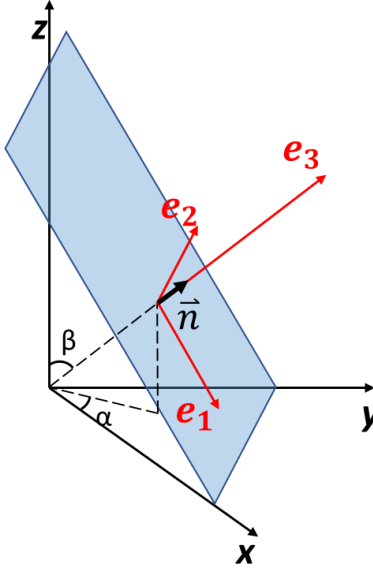


**Figure 3.2 – Schematics of natural fracture in the global and local coordinate systems**

The deformation of the fractured rock consists of two parts, one from the intact rock and the other one from the fracture set. In the equivalent continuum method, it can be assumed that the total strain increment of the continuum is the summation of the elastic strains in both intact rock and fractures. The new stress-strain relation of the continuum in the global coordinate system can be expressed as,

$$\Delta \varepsilon_{ij} = \Delta \varepsilon_{ij}^I + \Delta \varepsilon_{ij}^J \quad (3.1)$$

where  $\Delta \varepsilon$  is the total strain increment of the fractured rock,  $\Delta \varepsilon^I$  is the strain increment from intact rock, and  $\Delta \varepsilon^J$  is the strain increment from fracture set. Equation 3.1 can be further expressed using the effective stress as (Bagheri and Settari 2008),

$$\Delta \varepsilon_{ij} = S_{ijkl} \Delta \sigma'_{kl} = S_{ijkl}^I \Delta \sigma'_{kl} + S_{ijkl}^J \Delta \sigma'_{kl} \quad (3.2)$$

Where  $S_{ijkl}$  is the equivalent compliance of the fractured rock,  $S_{ijkl}^I$  is the compliance of the intact rock,  $S_{ijkl}^J$  is the compliance of the fracture set, and  $\Delta \sigma'_{kl}$  is the increment effective stress in the

global coordinate system. The compliance of the isotropic intact rock is described in Equation 2.18. For natural fractures, the compliance in the global coordinate system can be obtained using the fracture stiffness matrix  $D_{ij}$  with appropriate matrix transformation. The fracture stiffness matrix links the fracture displacements with the applied normal and shear stress increments in the local coordinate system,

$$\Delta\delta_j = D_{ij}\Delta\tau_j \quad (3.3)$$

or in matrix form,

$$\begin{bmatrix} \Delta\delta_1 \\ \Delta\delta_2 \\ \Delta\delta_3 \end{bmatrix} = \begin{bmatrix} D_{11} & D_{12} & D_{13} \\ D_{21} & D_{22} & D_{23} \\ D_{31} & D_{32} & D_{33} \end{bmatrix} \begin{bmatrix} \Delta\tau_1 \\ \Delta\tau_2 \\ \Delta\tau_3 \end{bmatrix} \quad (3.4)$$

where  $\Delta\delta$  is the fracture displacement increment,  $\Delta\tau$  is the traction increment on fracture surface, and subscript  $( )_1$ ,  $( )_2$ , and  $( )_3$  indicate the fracture dip, and fracture strike, and fracture normal direction respectively as shown in Figure 3.2.

The traction on fracture surface  $\tau_j$  can be calculated from the stresses in global coordinate system and normal unit vector of the fracture  $n_i$ ,

$$\tau_j = \sigma_{ij}n_i \quad (3.5)$$

With assumptions that small deformation on fracture surfaces and neglect coupled effect of shear and normal components, Equation 3.4 can be simplified as Huang et al. (1995),

$$\begin{bmatrix} \Delta\delta_1 \\ \Delta\delta_2 \\ \Delta\delta_3 \end{bmatrix} = \begin{bmatrix} D_{11} & 0 & 0 \\ 0 & D_{22} & 0 \\ 0 & 0 & D_{33} \end{bmatrix} \begin{bmatrix} \Delta\tau_1 \\ \Delta\tau_2 \\ \Delta\tau_3 \end{bmatrix} \quad (3.6)$$

where  $D_{11}$  and  $D_{22}$  are the inverse of fracture shear stiffness  $k_s$ , and  $D_{33}$  is the inverse of fracture normal stiffness  $k_n$ .

Based on the principle of energy conservation, Huang et al. (1995) proposed a relationship between the strain of the fracture sets and fracture displacements,

$$\Delta \varepsilon_{ij}^J = \sum_{n=1}^M n_i^n \Delta \delta_j^n \frac{1}{s_f^n} \quad (3.7)$$

where  $M$  is the total number of fracture sets,  $s_f$  is the fracture spacing. By substituting Equation 3.3 and 3.5 into Equation 3.7, for each fracture set,

$$S_{ijkl}^J = n_i D_{jk} n_l \frac{1}{s_f} \quad (3.8)$$

Since the compliance tensor for the isotropic intact rock is invariant, thus is independent of coordinate systems. In the local coordinate system, the equivalent compliance tensor of rock mass containing one set of fracture can be expressed as,

$$\hat{S}_{ijkl} = \hat{S}_{ijkl}^I + \hat{S}_{ijkl}^J \quad (3.9)$$

or in matrix form,

$$\hat{S}_{ijkl} = \begin{bmatrix} \frac{1}{E} & -\frac{\nu}{E} & -\frac{\nu}{E} & 0 & 0 & 0 \\ -\frac{\nu}{E} & \frac{1}{E} & -\frac{\nu}{E} & 0 & 0 & 0 \\ -\frac{\nu}{E} & -\frac{\nu}{E} & \frac{1}{E} + \frac{1}{k_n s_f} & 0 & 0 & 0 \\ 0 & 0 & 0 & \frac{1}{G} + \frac{1}{k_s s_f} & 0 & 0 \\ 0 & 0 & 0 & 0 & \frac{1}{G} + \frac{1}{k_s s_f} & 0 \\ 0 & 0 & 0 & 0 & 0 & \frac{1}{G} \end{bmatrix} \quad (3.10)$$

where the hat accent denotes the local coordinate system.

Transformation of the equivalent compliance tensor from the local coordinate system to the global coordinate system can be achieved with transformation matrix  $R_1$  containing directional cosine of fracture dip angle and dip direction,

$$S_{ijkl} = R_1 \hat{S}_{ijkl} R_1^T \quad (3.11)$$

and

$$R_1 = \begin{bmatrix} l_{11}^2 & l_{12}^2 & l_{13}^2 & l_{12}l_{13} & l_{11}l_{13} & l_{12}l_{11} \\ l_{22}^2 & l_{21}^2 & l_{23}^2 & l_{23}l_{22} & l_{23}l_{21} & l_{22}l_{21} \\ l_{33}^2 & l_{32}^2 & l_{31}^2 & l_{33}l_{32} & l_{33}l_{31} & l_{32}l_{31} \\ 2l_{21}l_{31} & 2l_{32}l_{22} & 2l_{33}l_{23} & l_{33}l_{22} + l_{32}l_{23} & l_{33}l_{21} + l_{31}l_{23} & l_{31}l_{22} + l_{32}l_{21} \\ 2l_{11}l_{31} & 2l_{32}l_{12} & 2l_{33}l_{13} & l_{33}l_{12} + l_{32}l_{13} & l_{33}l_{11} + l_{31}l_{13} & l_{31}l_{12} + l_{32}l_{11} \\ 2l_{21}l_{11} & 2l_{12}l_{22} & 2l_{13}l_{23} & l_{13}l_{22} + l_{12}l_{23} & l_{13}l_{21} + l_{11}l_{23} & l_{11}l_{22} + l_{12}l_{21} \end{bmatrix} \quad (3.12)$$

Where  $l_{ij}$  contains the directional cosine between the global and the local coordinate systems,

$$l_{11} = \cos(e_1, x) \quad l_{12} = \cos(e_2, x) \quad l_{13} = \cos(e_3, x) \quad (3.13)$$

$$l_{21} = \cos(e_1, y) \quad l_{12} = \cos(e_2, y) \quad l_{23} = \cos(e_3, y) \quad (3.14)$$

$$l_{31} = \cos(e_1, z) \quad l_{32} = \cos(e_2, z) \quad l_{33} = \cos(e_3, z) \quad (3.15)$$

Once equivalent compliance tensor is calculated, the equivalent stiffness tensor  $C_{ijkl}$  can be obtained by inverting the compliance tensor.

### 3.2 Finite-Element-Based Geomechanical Model

In this study, a finite-element-based model is built to evaluate the reservoir stress distributions and geomechanical properties. This section presents the mathematical description, the finite element formulation and discretization for the three-dimensional geomechanical model, and discussions on the model limitations.



### 3.2.1 Finite-element formulation

The geomechanical model developed in this study follows the assumptions listed below:

- The model assumes elastic behavior for both intact rock and natural fractures.
- The body force is neglected.
- Failure of the intact rock is not considered.
- Fracture shear stiffness is assumed as a constant value in each grid cell.

The finite-element model is developed based on the constitutive equations described in the previous section, and the governing equations, the equilibrium of force and momentum, assuming quasi-static condition,

$$\sigma_{ij,j} + F_i^b = 0 \quad (3.16)$$

$$\int_{\Omega} (\sigma_{ij,j} + F_i^b) d\Omega = 0 \quad (3.17)$$

where  $F^b$  is the body force per unit volume, which in this study is not considered.

With the absence of the body force term and apply the principle of virtual displacements, which states that the summation of external virtual work,  $\delta R$ , done by the surface stress and the internal virtual work stored as strain energy,  $\delta W$ , should be equal to zero (Reddy 2004 ),

$$\delta W + \delta R = 0 \quad (3.18)$$

$\delta W$  and  $\delta R$  are defined as,

$$\delta W = \int_{\Omega} \sigma_{ij} \delta \varepsilon_{ij} d\Omega \quad (3.19)$$

and

$$\delta R = \int_{\Gamma} T_j \delta u_j d\Gamma \quad (3.20)$$

Substitute Equation 3.19 and 3.20 into Equation 3.18, Equation 3.18 can be rewritten as,

$$\int_{\Omega} \sigma_{ij} \delta \varepsilon_{ij} d\Omega = - \int_{\Gamma} T_j \delta u_j d\Gamma \quad (3.21)$$

or,

$$\int_{\Omega} \delta \varepsilon^T \sigma d\Omega = - \int_{\Gamma} \delta u^T T d\Gamma \quad (3.22)$$

Where  $\delta u_j$  is the virtual displacement,  $\delta \varepsilon_{ij}$  is the virtual strain associated with virtual displacement, and  $T$  is the boundary stress.

In this study, an 8-node brick element and linear shape functions are used. In three-dimensional space, the displacement vector  $u = (u_1 \ u_2 \ u_3)^T$  at any location within the element can be expressed using the nodal displacements and corresponding shape functions,

$$u = \sum_{k=1}^8 N_k u^k \quad (3.23)$$

where  $u^k$  is the nodal displacement vector,  $N_k$  is the corresponding shape function. For brick element with 8 nodes, the shape function for each node is,

$$N_k = \frac{1}{8} (1 + \xi_k \xi) (1 + \eta_k \eta) (1 + \varsigma_k \varsigma) \quad (3.24)$$

where  $\xi$ ,  $\eta$ , and  $\varsigma$  are the transformed coordinates, where in this coordinate the vertices of the original brick or tetrahedron,  $\xi_k$ ,  $\eta_k$  and  $\varsigma_k$  are now at  $(\pm 1, \pm 1, \pm 1)$  as shown in Figure 3.3.

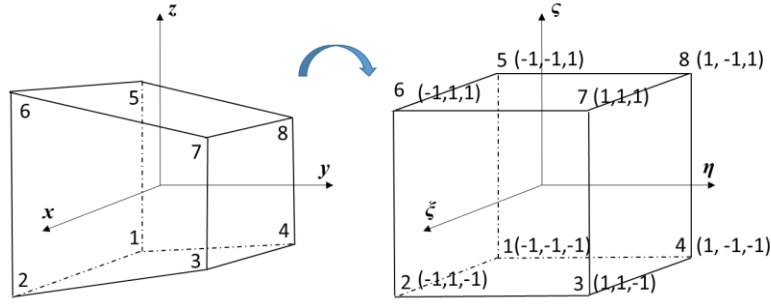


**Figure 3.3 – Illustration of space transformation of an 8-node element from the global coordinate to the transformed coordinate**

If the shape function matrix  $N$  and element displacement vector  $\hat{u}^e$  are defined as,

$$N = \begin{bmatrix} N_1 & 0 & 0 & \cdots & N_8 & 0 & 0 \\ 0 & N_1 & 0 & \cdots & 0 & N_8 & 0 \\ 0 & 0 & N_1 & \cdots & 0 & 0 & N_8 \end{bmatrix} \quad (3.25)$$

and

$$\hat{u}^e = (u^1 \quad \cdots \quad u^8)^T \quad (3.26)$$

Then Equation 3.23, can be rewritten as,

$$u = N\hat{u}^e \quad (3.27)$$

Now we define operator matrices  $L$  and  $B$  as,

$$L = \begin{bmatrix} \frac{\partial}{\partial x} & 0 & 0 \\ 0 & \frac{\partial}{\partial y} & 0 \\ 0 & 0 & \frac{\partial}{\partial z} \\ 0 & \frac{\partial}{\partial z} & \frac{\partial}{\partial y} \\ \frac{\partial}{\partial z} & 0 & \frac{\partial}{\partial x} \\ \frac{\partial}{\partial y} & \frac{\partial}{\partial x} & 0 \end{bmatrix} \quad (3.28)$$

and

$$B = LN \quad (3.29)$$

Then the strain components at any point in an element can be defined as,

$$\varepsilon = B\hat{u}^e \quad (3.30)$$

or in matrix form,

$$\begin{bmatrix} \varepsilon_x \\ \varepsilon_y \\ \varepsilon_z \\ \gamma_{yz} \\ \gamma_{xz} \\ \gamma_{xy} \end{bmatrix} = \begin{bmatrix} \frac{\partial N_1}{\partial x} & 0 & 0 & \dots & \frac{\partial N_8}{\partial x} & 0 & 0 \\ 0 & \frac{\partial N_1}{\partial y} & 0 & \dots & 0 & \frac{\partial N_8}{\partial y} & 0 \\ 0 & 0 & \frac{\partial N_1}{\partial z} & \dots & 0 & 0 & \frac{\partial N_8}{\partial z} \\ 0 & \frac{\partial N_1}{\partial z} & \frac{\partial N_1}{\partial y} & \dots & 0 & \frac{\partial N_8}{\partial z} & \frac{\partial N_8}{\partial y} \\ \frac{\partial N_1}{\partial z} & 0 & \frac{\partial N_1}{\partial x} & \dots & \frac{\partial N_8}{\partial z} & 0 & \frac{\partial N_8}{\partial x} \\ \frac{\partial N_1}{\partial y} & \frac{\partial N_1}{\partial x} & 0 & \dots & \frac{\partial N_8}{\partial y} & \frac{\partial N_8}{\partial x} & 0 \end{bmatrix} \begin{bmatrix} u_1^1 \\ u_2^1 \\ u_3^1 \\ \vdots \\ u_1^8 \\ u_2^8 \\ u_3^8 \end{bmatrix} \quad (3.31)$$

With the constitutive relationship, the stress can be expressed as,

$$\sigma = CB\hat{u}^e \quad (3.32)$$

Substitute Equation 3.32 into 3.22,

$$\int_{\Omega} \delta u^T B^T C B \hat{u}^e d\Omega = - \int_{\Gamma} \delta u^T N^T T d\Omega \quad (3.33)$$

Equation 3.33 can be further rewritten as,

$$\left( \int_{\Omega} B^T C B d\Omega \right) \hat{u}^e = - \int_{\Gamma} N^T T d\Omega \quad (3.34)$$

or,

$$K^e \hat{u}^e = f^e \quad (3.35)$$

where  $K^e$  is the element stiffness matrix,  $f^e$  is the element load vector. With appropriate assembly, the total stiffness matrix  $K$  and total load vector  $f$  can be compiled to solve the total displacements within the simulation domain.

The integration of in the stiffness matrix is often performed by employing Simpson's integration rule by transforming the original brick or tetrahedron element in the global coordinate system into a cubic element in the local coordinate system, as shown in Figure 3.3. The stiffness matrix then can be expressed as,

$$K = \int_{\Omega} B^T C B d\Omega = \int_{-1}^1 \int_{-1}^1 \int_{-1}^1 B^T C B \det(J) d\xi d\eta d\zeta \quad (3.36)$$

where  $J$  is the Jacobian matrix,

$$\begin{bmatrix} \frac{\partial}{\partial \xi} \\ \frac{\partial}{\partial \eta} \\ \frac{\partial}{\partial \zeta} \end{bmatrix} = \begin{bmatrix} \frac{\partial x}{\partial \xi} & \frac{\partial y}{\partial \xi} & \frac{\partial z}{\partial \xi} \\ \frac{\partial x}{\partial \eta} & \frac{\partial y}{\partial \eta} & \frac{\partial z}{\partial \eta} \\ \frac{\partial x}{\partial \zeta} & \frac{\partial y}{\partial \zeta} & \frac{\partial z}{\partial \zeta} \end{bmatrix} \begin{bmatrix} \frac{\partial}{\partial x} \\ \frac{\partial}{\partial y} \\ \frac{\partial}{\partial z} \end{bmatrix} = J \begin{bmatrix} \frac{\partial}{\partial x} \\ \frac{\partial}{\partial y} \\ \frac{\partial}{\partial z} \end{bmatrix} \quad (3.37)$$

or

$$\begin{bmatrix} \frac{\partial}{\partial x} \\ \frac{\partial}{\partial y} \\ \frac{\partial}{\partial z} \end{bmatrix} = \begin{bmatrix} \frac{\partial x}{\partial \xi} & \frac{\partial y}{\partial \xi} & \frac{\partial z}{\partial \xi} \\ \frac{\partial x}{\partial \eta} & \frac{\partial y}{\partial \eta} & \frac{\partial z}{\partial \eta} \\ \frac{\partial x}{\partial \zeta} & \frac{\partial y}{\partial \zeta} & \frac{\partial z}{\partial \zeta} \end{bmatrix} \begin{bmatrix} \frac{\partial}{\partial \xi} \\ \frac{\partial}{\partial \eta} \\ \frac{\partial}{\partial \zeta} \end{bmatrix} = J^{-1} \begin{bmatrix} \frac{\partial}{\partial \xi} \\ \frac{\partial}{\partial \eta} \\ \frac{\partial}{\partial \zeta} \end{bmatrix} \quad (3.38)$$

When multiple load increments are implemented, which is commonly used in nonlinear finite element analysis, the internal force  $F_{int}$  needs to be calculated from the nodal displacement solution to check the force balance at each iteration within one load step,

$$F_{int} = \int_{\Omega} B^T C B u d\Omega = \int_{\Omega} B^T \sigma d\Omega \quad (3.39)$$

The residual force or the out of balance force  $R$  is defined as the difference between the external force and the internal force at the current load step,

$$R = F_{ext} - F_{int} \quad (3.40)$$

If the residual force is larger than the assigned tolerance, an incremental displacement vector is calculated from the residual force and added to be previous displacement solution. The iteration procedure continues until either the tolerance is met, or the maximum rounds of iterations are reached. Generally, if the material is linear elastic, the calculated internal force is the same as the external force and no iteration is required. However, if the constitutive equation nonlinear, then the iterations are required to obtain the force equilibrium. The solution for such kind of problem usually requires numerical techniques such as Full Newton-Raphson method, Modified Newton-Raphson method, or Picard Iteration method (Reddy 2004). Once the force balance is reached, the external force for next load step can be expressed as,

$$F_{ext} = F_{int} + \Delta F_{ext} \quad (3.41)$$

The solution schemes for each method is demonstrated in Figure 3.4. As shown in Figure 3.4 a), the implementation of the Full Newton-Raphson method requires change of rock stiffness at each iteration within one load step. For the Modified Newton-Raphson method as shown in Figure 3.4 b), the rock stiffness is set to be constant until change is demanded. Usually, in the Modified Newton-Raphson method, the change of rock stiffness is at the beginning of each load step. The Picard Iteration method or the Direct Iteration method as shown in Figure 3.4 c), also updates the rock stiffness, however, instead of using tangent stiffness as in the Full Newton-Raphson method, the secant stiffness is used. Detailed derivations and applications of the above

iteration techniques and other methods for solving nonlinear equations can be found in reference as Reddy's work (Reddy 2004).

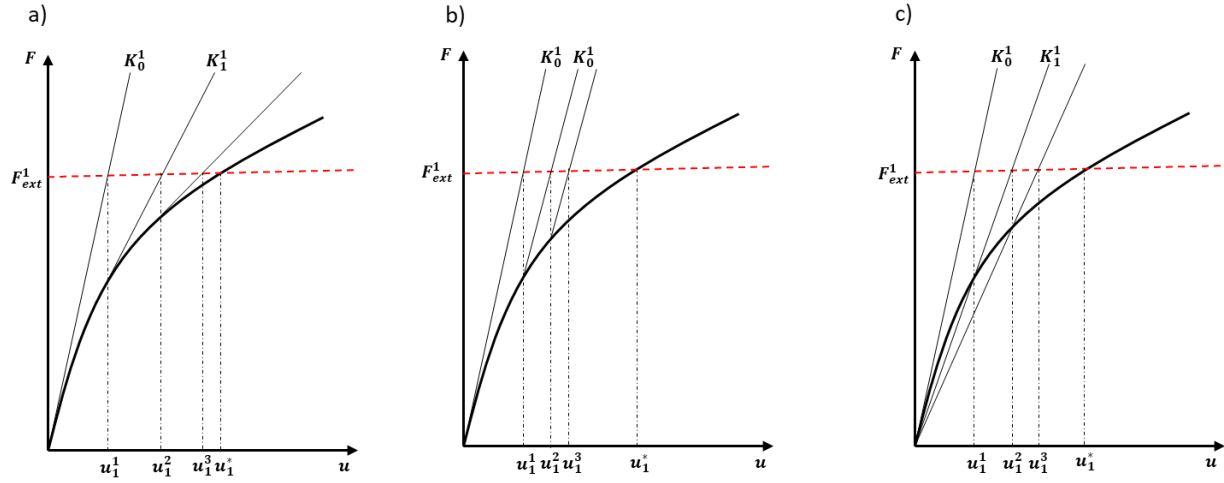


**Figure 3.4 – Illustration of iteration techniques for nonlinear finite element analysis. a) Full Newton-Raphson method. b) Modified Newton-Raphson method. c) Picard Iteration method. Reprinted from Reddy (2004)**

Due to the nature of fracture stress-displacement relation, the Modified Newton Raphson method causes divergence of solution, and the Picard Iteration method provides a slow convergence rate. Thus, in this study, the Full Newton-Raphson method is adopted as the solution technique for the nonlinear finite element analysis since it provides a relatively fast and stable convergence to the solution.

### 3.2.2 Model validation with a single fracture

The validation of the numerical model with the Full Newton-Raphson method is presented in this section. The simulated results of stress and strain curve for a uniaxial test on rock sample with one single fracture is compared with the analytical solution. The sample is assumed to have a dimension of 1m×1m×1m with fracture placed in the center of the sample. The fracture surface

is assumed to be perpendicular to the z-axis which is also the direction of the loading. Other parameters used for model verification are shown in Table 1.

**Table 1 – Input parameters to simulate normal displacement of single fracture under uniaxial loading condition**

Initial Fracture Normal Stiffness $K_{ni}$ , [GPa/m]	5
Fracture Shear Stiffness $K_s$ , [GPa/m]	5
Maximum Fracture Closure $v_m$ , [m]	2e-4
Young's Modulus of Intact Rock $E$ , [GPa]	20
Poisson's Ratio of Intact Rock $\nu$	0.33
Applied Normal Stress in z-direction $\sigma_n$ , [MPa]	0-10

The analytical solution for the normal displacement of a single fracture under uniaxial loading is expressed as a hyperbolic function (Bandis et al. 1983),

$$\sigma_n = \frac{K_{ni}V_j}{1 - \frac{V_j}{V_m}} \quad (3.42)$$

Figure 3.5 shows the simulated total displacement of the sample under 1 MPa uniaxial loading condition from the numerical model and compared to the stress-displacement curve derived from analytical solution. The total displacement of the sample is the summation of the displacements caused by the fracture and the intact rock. For this case, to achieve the force balance under 1 MPa applied stress, 4 iterations are need using full Newton-Raphson scheme.



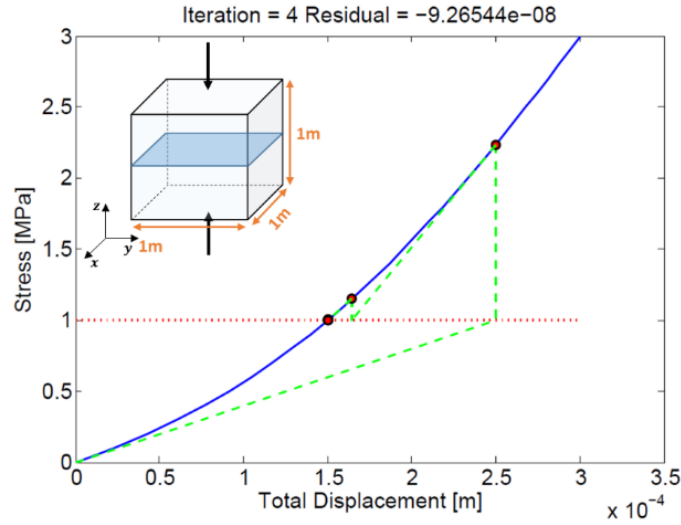


**Figure 3.5 – Simulated and analytical total displacement of the sample with a single fracture under uniaxial loading condition. The Full Newton-Raphson method is used for iteration.**

Figure 3.6 shows the simulated fracture displacement and the analytical solution up to 10 MPa loading in the z-direction.

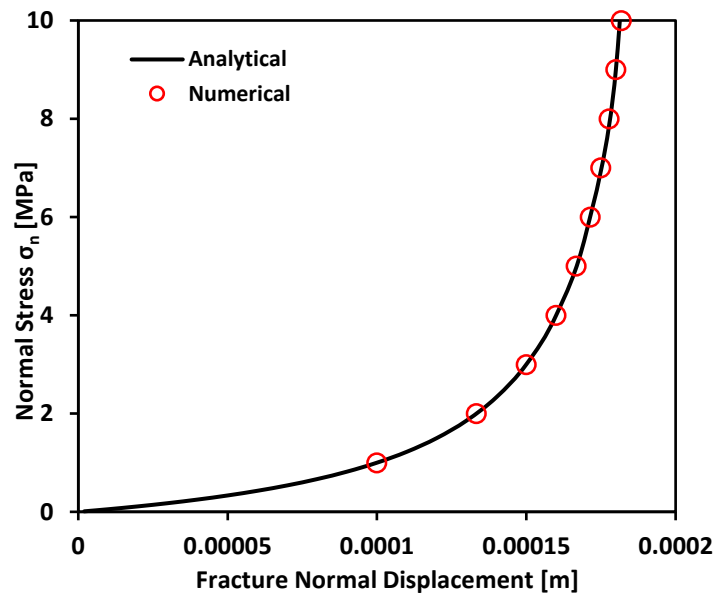


**Figure 3.6 – Simulated and analytical fracture normal displacement under increasing normal stress**

### *3.2.3 Model limitations*

The current finite-element-based geomechanical model only accounts for elastic material. Plastic deformations of the rock and fracture are not included. The shear failure of the intact rock and post failure behavior are also ignored. In this study, it is assumed that except for the pre-existing natural fractures, no other discontinuous surfaces are generated during the simulation. However, the mathematical model presented in section 3.2.1 can be used for multiple fracture sets. For simplicity and demonstrative purpose, in this study, only one fracture set is implemented in the numerical model.

## **3.3 Wellbore Stability Model in Anisotropic Formations**

### *3.3.1 Model development*

The wellbore stability model developed in this study follows the assumptions listed below:

- The model assumes elastic behavior for both intact rock and natural fractures.
- Mud penetration into the formation and natural farceurs are not considered.
- Fracture normal and shear stiffnesses are assumed as constants.

The development of wellbore stability model shares similar procedure as the development of the geomechanical model presented in section 3.2.1. The difference from the geomechanical model is that the simulation domain is now bounded with a hollow cylinder at the center as shown in Figure 3.7. The grid block also changed from brick elements to tetrahedron elements to adapt the shape of the borehole.

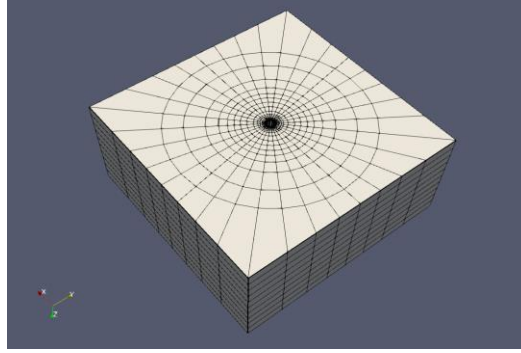


**Figure 3.7 –Geometry and model structure for wellbore stability analysis**

There are 25 elements in the radial direction, 32 elements in the tangential direction and 10 elements in the depth direction. To improve the accuracy of the stress simulation in the near-wellbore region, the size of the grid block towards the borehole is gradually refined. The model considers the elastic anisotropy due to the presence of natural fractures. However, in this study, we use constant fracture normal and shear stiffnesses during the simulation, thus the nonlinear mechanical behavior is not included in the model.

Experimental observations show that the strength of the rock containing weak planes is dependent on the orientations of the weak planes, such as beddings or natural fractures (Pomeroy and Mohmoud 1997, McLamore and Gray 1967) as shown in Figure 3.8.

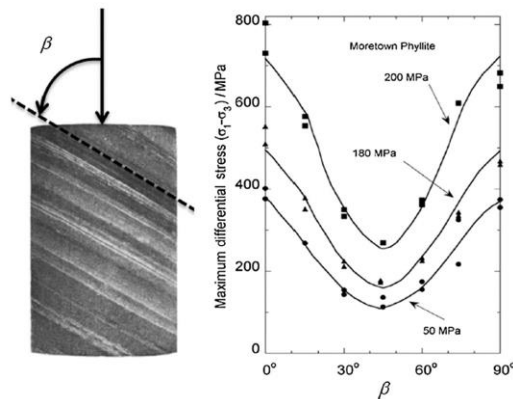


**Figure 3.8 – Laminated rock sample and differential stress at failure with respect to the inclination angles of the lamination. Reprinted from Saeidi et al. (2014).**

Borehole stability analysis in naturally fractured reservoirs needs to consider both the failure of the intact rock around the borehole and the slippage of the natural fractures. In this study, two types of failure criteria are employed. For the intact rock, the Mohr-Coulomb failure criterion is used,

$$\sigma_1 = \sigma_3 + 2(C_0 + \mu\sigma_3) \left( \sqrt{1 + \mu^2} + \mu \right) \quad (3.43)$$

for natural fractures,

$$\tau = C_0^{nf} + \mu^{nf} \sigma_n \quad (3.44)$$

where  $\sigma_1$  and  $\sigma_3$  are the maximum and minimum principal stresses,  $C_0$  and  $\mu$  are the cohesive strength and coefficient of friction of the intact rock,  $C_0^{nf}$  and  $\mu^{nf}$  are cohesive strength and coefficient of friction of natural fractures,  $\tau$  and  $\sigma_n$  are shear and normal stress on fracture surfaces.

### 3.3.2 Model validation

The analytical solution for stress distribution around a hollow cylinder in an anisotropic elastic material was proposed by Lekhnitskii (1963). The solution was derived based on general plane strain assumption where the stress-strain constitutive relation is expressed as,

$$\begin{bmatrix} \varepsilon_{xx} \\ \varepsilon_{yy} \\ 0 \\ \gamma_{yz} \\ \gamma_{xz} \\ \gamma_{xy} \end{bmatrix} = \begin{bmatrix} C_{11} & C_{12} & C_{13} & C_{14} & C_{15} & C_{16} \\ C_{21} & C_{22} & C_{23} & C_{24} & C_{25} & C_{26} \\ C_{31} & C_{32} & C_{33} & C_{34} & C_{35} & C_{36} \\ C_{41} & C_{42} & C_{43} & C_{44} & C_{45} & C_{46} \\ C_{51} & C_{52} & C_{53} & C_{54} & C_{55} & C_{56} \\ C_{61} & C_{62} & C_{63} & C_{64} & C_{65} & C_{66} \end{bmatrix} \begin{bmatrix} \sigma_{xx} \\ \sigma_{yy} \\ \sigma_{zz} \\ \tau_{yz} \\ \tau_{xz} \\ \tau_{xy} \end{bmatrix} \quad (3.45)$$

along with equilibrium equations,

$$\frac{\partial \sigma_{xx}}{\partial x} + \frac{\partial \tau_{xy}}{\partial y} = 0 \quad (3.46)$$

$$\frac{\partial \sigma_{yy}}{\partial y} + \frac{\partial \tau_{xy}}{\partial x} = 0 \quad (3.47)$$

$$\frac{\partial \tau_{xz}}{\partial x} + \frac{\partial \tau_{yz}}{\partial y} = 0 \quad (3.48)$$

and compatibility equations,

$$\frac{\partial^2 \varepsilon_{xx}}{\partial y^2} + \frac{\partial^2 \varepsilon_{yy}}{\partial x^2} = \frac{\partial^2 \gamma_{xy}}{\partial x \partial y} \quad (3.49)$$

$$\frac{\partial \gamma_{zx}}{\partial y} - \frac{\partial \gamma_{yz}}{\partial x} = 0 \quad (3.50)$$

The final form of the stress components is composed of the far field stresses in the borehole coordinate system and borehole-induced stresses,

$$\sigma_{xx}^{b,ani} = \sigma_{xx}^b + \sigma_{xx}^{b,i} = \sigma_{xx}^b + 2\text{Re}[\mu_1^2 \phi_1'(z_1) + \mu_2^2 \phi_2'(z_2) + \lambda_3 \mu_3^2 \phi_3'(z_3)] \quad (3.51)$$

$$\sigma_{yy}^{b,ani} = \sigma_{yy}^b + \sigma_{yy}^{b,i} = \sigma_{yy}^b + 2\text{Re}[\phi_1'(z_1) + \phi_2'(z_2) + \lambda_3 \phi_3'(z_3)] \quad (3.52)$$

$$\tau_{xy}^{b,ani} = \tau_{xy}^b + \tau_{xy}^{b,i} = \tau_{xy}^b - 2\text{Re}[\mu_1 \phi_1'(z_1) + \mu_2 \phi_2'(z_2) + \lambda_3 \mu_3 \phi_3'(z_3)] \quad (3.53)$$

$$\tau_{xz}^{b,ani} = \tau_{xz}^b + \tau_{xz}^{b,i} = \tau_{xz}^b + 2\text{Re}[\lambda_1 \mu_1 \phi_1'(z_1) + \lambda_2 \mu_2 \phi_2'(z_2) + \mu_3 \phi_3'(z_3)] \quad (3.54)$$

$$\tau_{yz}^{b,ani} = \tau_{yz}^b + \tau_{yz}^{b,i} = \tau_{yz}^b - 2\text{Re}[\lambda_1 \phi_1'(z_1) + \lambda_2 \phi_2'(z_2) + \phi_3'(z_3)] \quad (3.55)$$

$$\sigma_{zz}^{b,ani} = \sigma_{zz}^b - \frac{1}{C_{33}} (C_{31} \sigma_{xx}^{b,i} + C_{32} \sigma_{yy}^{b,i} + C_{34} \tau_{yz}^{b,i} + C_{35} \tau_{yz}^{b,i} + C_{36} \tau_{xy}^{b,i}) \quad (3.56)$$

where the superscript ( )<sup>b,ani</sup> represents the stresses around the wellbore in the anisotropic elastic formation, ( )<sup>b</sup> represents the far-field stress in the borehole coordinate system, ( )<sup>b,i</sup> represents the induced stress caused by removing the rock from the wellbore, Re( ) is the real part of a complex number,  $\mu_i$  are six complex or imaginary roots of a sextic polynomial equation,

$\lambda_i$  are three coefficients obtained from  $\mu_i$ , and  $\phi'_i$  are three analytical functions. The detailed derivation and explanations of the terms can be found in Appendix A and Appendix B.

To validate the borehole stability model, the simulation results are first compared with the analytical solutions of borehole stress distributions in an isotropic formation (Bradly 1979) with boundary stress conditions and rock elastic properties shown in Table 2.

**Table 2 – Simulation parameters for isotropic formation case**

Stress in x-direction $\sigma_x$ , [MPa]	20
Stress in y-direction $\sigma_y$ , [MPa]	15
Stress in z-direction $\sigma_z$ , [MPa]	25
Wellbore Pressure $p_w$ [MPa]	5
Young's Modulus E, [GPa]	10
Poisson's ratio $\nu$	0.3

Figure 3.9 shows the numerical solutions indicated as hollow marks and analytical solutions as solid lines. The results from the simulation compare well with the analytical results.

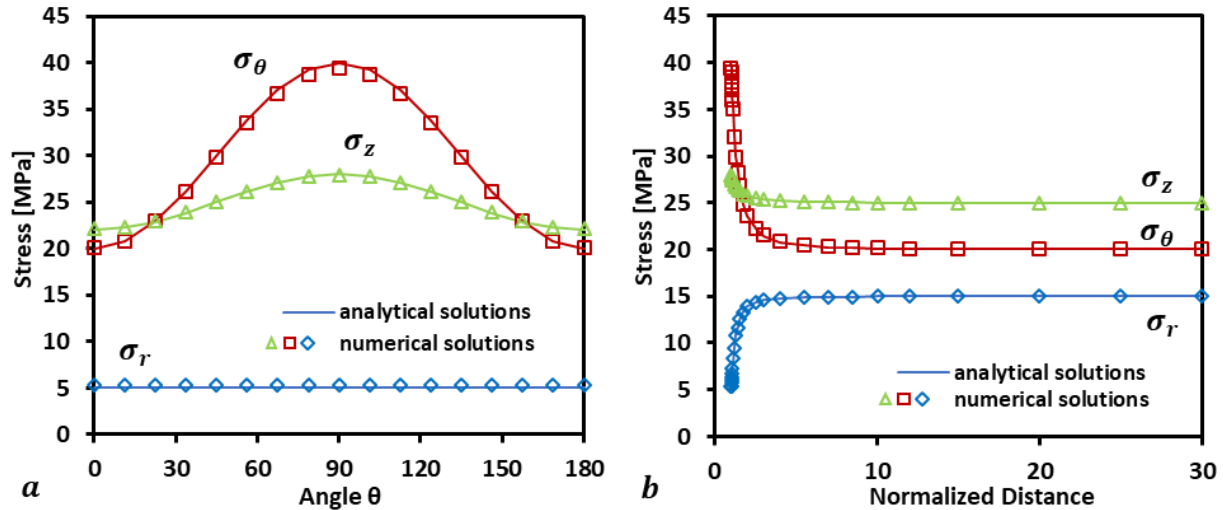


**Figure 3.9 – Stress distributions around wellbore in an isotropic formation (a) Comparison of numerical and analytical solutions for stress distribution at the borehole (b) Comparison of numerical and analytical solutions for stress distributions along the y-axis**

The verification of the model for an anisotropic formation used the same stress conditions and formation Young's modulus and Poisson's ratio as the isotropic case. Two sets of natural fractures are implemented in the simulation domain separately. The first set of simulations compares impacts of fracture normal stiffness on stress distributions around the wellbore. The second set of simulations compares the effect of natural fracture orientations on the stress distributions. The properties for each case are summarized in Table 3 and Table 4. Fracture shear stiffness usually takes a fraction of intact rock shear modulus or a proportion of fracture normal stiffness. In this study, a constant fracture shear stiffness same as the intact rock shear modulus is used in the model validation. Figure 3.10 and 3.11 show the simulated stresses and compared with analytical solutions, where the solid lines denote the analytical solutions and the symbols denote the numerical results.

As shown in Figure 3.10, for a vertical fracture set with strike angle is  $45^\circ$  from the x-axis, when the magnitude of fracture normal stiffness is equal to one-tenth of the intact rock Young's modulus, the numerical simulation results start to show significant differences comparing to the analytical solutions. The error suggests that for the field applications, if the fracture is too compliant, such as the magnitude of fracture normal stiffness is lower than one-tenth of the rock Young's modulus, the numerical model may yield inaccurate stress estimations.

The effect of fracture inclination on the stress distributions at the wellbore is not as dramatic when comparing to the impact of fracture stiffness. Figure 3.11 shows the simulated and analytical solutions of the stress around the borehole with fracture inclination angle ranging from  $0^\circ$  to  $90^\circ$ . In this sensitivity study, the magnitude of the fracture normal stiffness is kept as a constant as half of the rock Young's modulus.

**Table 3 – First set of natural fracture properties**

Fracture Normal Stiffness $K_n$ , [GPa/m]	10, 5, 2, 1
Fracture Shear Stiffness $K_s$ , [GPa/m]	3.85
Fracture dip direction $\alpha$	45°
Fracture inclination angle $\beta$	90°
Fracture Spacing $s_f$ , [m]	1
Maximum Fracture Closure $v_m$ , [m]	2e-4

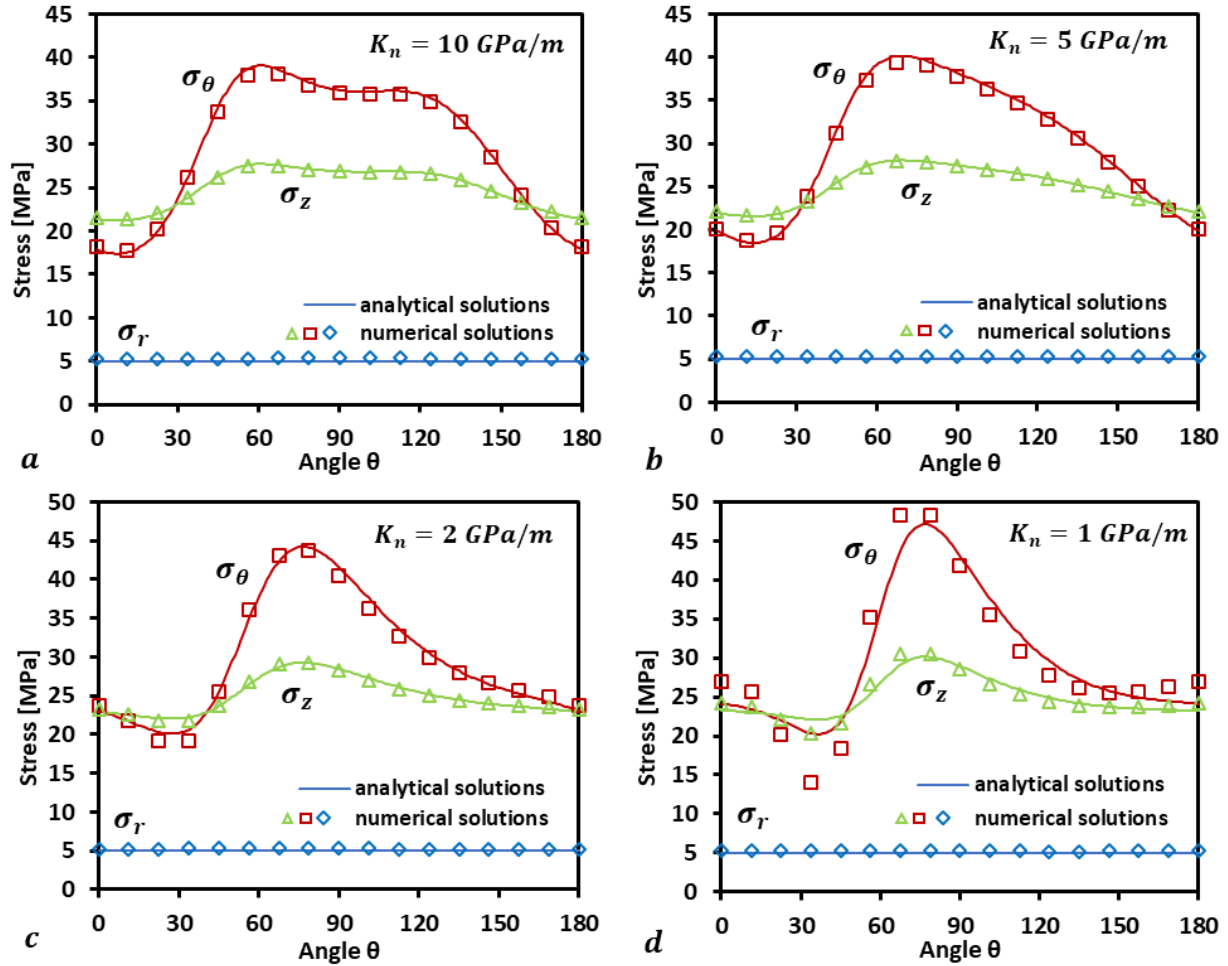


**Figure 3.10 – Stress distributions at the wellbore in an anisotropic formation (a) Fracture normal stiffness  $K_n = 10 \text{ GPa/m}$  (b) Fracture normal stiffness  $K_n = 5 \text{ GPa/m}$  (c) Fracture normal stiffness  $K_n = 2 \text{ GPa/m}$  and (d) Fracture normal stiffness  $K_n = 1 \text{ GPa/m}$**



**Table 4 – Second set of natural fracture properties**

Fracture Normal Stiffness $K_n$ , [GPa/m]	5
Fracture Shear Stiffness $K_s$ , [GPa/m]	3.85
Fracture dip direction $\alpha$	45°
Fracture inclination angle $\beta$	0°, 30°, 60°, 90°
Fracture Spacing $s_f$ [m]	1
Maximum Fracture Closure $v_m$ , [m]	2e-4

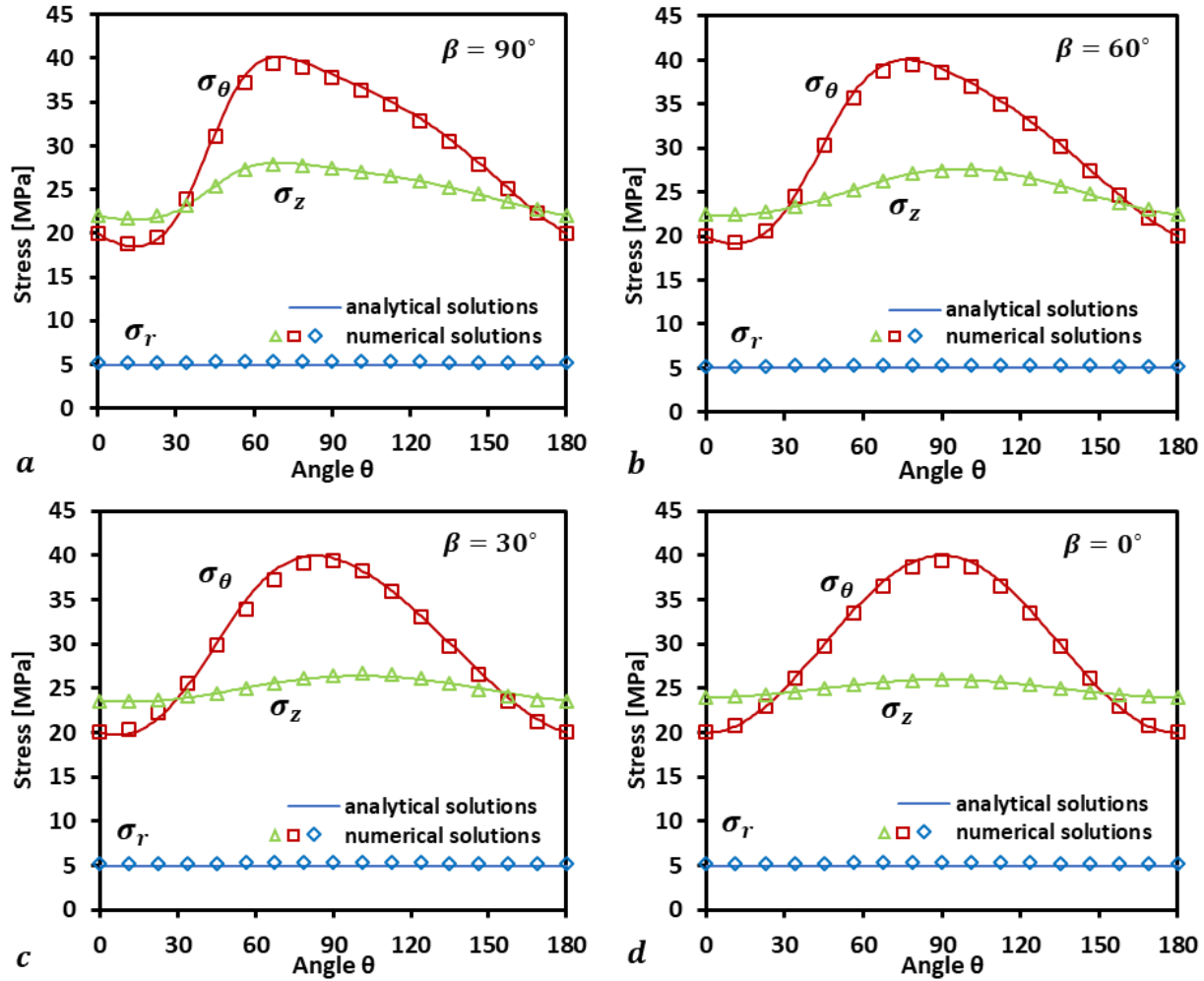


**Figure 3.11 – Stress distributions at the wellbore in an anisotropic formation (a) Fracture inclination angle  $\beta = 90^\circ$  (b) Fracture inclination angle  $\beta = 60^\circ$  (c) Fracture inclination angle  $\beta = 30^\circ$  and (d) Fracture inclination angle  $\beta = 0^\circ$**

### 3.3.3 Model limitations

The wellbore stability model is limited to elastic deformation of the fractured rock. Plastic deformations of the natural fractures and the intact rock are not included. Mud penetration into the formation and natural fractures while drilling may cause change of pore pressure around the wellbore region, resulting in changes of effective in-situ stresses as well as the effective normal stress acting on the fracture planes. The effect of mud penetration may alter the stress conditions for wellbore failure as predicted by the model. Further study and improvements in the wellbore stability model should focus on taking account of the effects described above.

## 3.4 Seismic Velocity Anisotropy

Seismic data interpretation is a tool to understand the geological structure and identify changes of rock properties at the reservoir scale, as supported by the experimental studies that the velocity of wave propagates through jointed media is anisotropic and varies depends on wave propagation direction and stress conditions (Nur and Simmons, 1969; Mavko and Nur, 1978).

The in-situ stresses are often triaxial with three principal stresses with different values, which in turn will affect the aperture of the natural fractures in different orientations resulting in change in elastic moduli. The stress-induced P- and S-wave velocity anisotropy, therefore, can be used as a method to calibrate the orientation of natural fractures and stress state of the field.

In this study, anisotropic P- and S-wave phase velocities in arbitrary propagation direction  $n = (n_1, n_2, n_3)^T$  are computed based on stiffness tensor under a given stress state (Helbig, 1994). The components of Kelvin-Christoffel matrix  $\Gamma_{ij}$  is first computed based on the stiffness tensor  $C_{ij}$  in Voigt notation and wave propagation direction vector  $n$ ,

$$\Gamma_{11} = n_1^2 C_{11} + n_2^2 C_{66} + n_3^2 C_{55} + 2n_1 n_2 C_{16} + 2n_1 n_3 C_{15} + 2n_2 n_3 C_{56} \quad (3.57)$$

$$\begin{aligned}\Gamma_{12} = & n_1 n_2 (C_{12} + C_{66}) + n_1^2 C_{16} + n_2^2 C_{26} + n_3^2 C_{45} + n_1 n_3 (C_{14} + C_{56}) \\ & + n_2 n_3 (C_{46} + C_{25})\end{aligned}\quad (3.58)$$

$$\begin{aligned}\Gamma_{13} = & n_1 n_2 (C_{13} + C_{55}) + n_1^2 C_{15} + n_2^2 C_{46} + n_3^2 C_{35} + n_1 n_2 (C_{14} + C_{56}) \\ & + n_2 n_3 (C_{36} + C_{45})\end{aligned}\quad (3.59)$$

$$\Gamma_{21} = \Gamma_{12} \quad (3.60)$$

$$\Gamma_{22} = n_1^2 C_{66} + n_2^2 C_{22} + n_3^2 C_{44} + 2n_1 n_2 C_{26} + 2n_1 n_3 C_{46} + 2n_2 n_3 C_{13} \quad (3.61)$$

$$\Gamma_{31} = \Gamma_{13} \quad (3.62)$$

$$\Gamma_{32} = \Gamma_{23} \quad (3.63)$$

$$\Gamma_{33} = n_1^2 C_{55} + n_2^2 C_{44} + n_3^2 C_{33} + 2n_1 n_2 C_{45} + 2n_1 n_3 C_{35} + 2n_2 n_3 C_{34} \quad (3.64)$$

The three eigenvalues  $\lambda_i$  of the the Kelvin-Christoffel matrix and density of the material  $\rho$  are related the three seismic velocities, P-wave, fast S-wave, and slow S-wave as,

$$V_i = \sqrt{\frac{\lambda_i}{\rho}} \quad (3.65)$$

The P-wave velocity usually corresponds to the largest eigenvalue and then the fast S-wave, and the slow S-wave velocities. The eigenvector associated with each eigenvalue gives the polarization direction of the corresponding wave as shown in Figure 3.12.

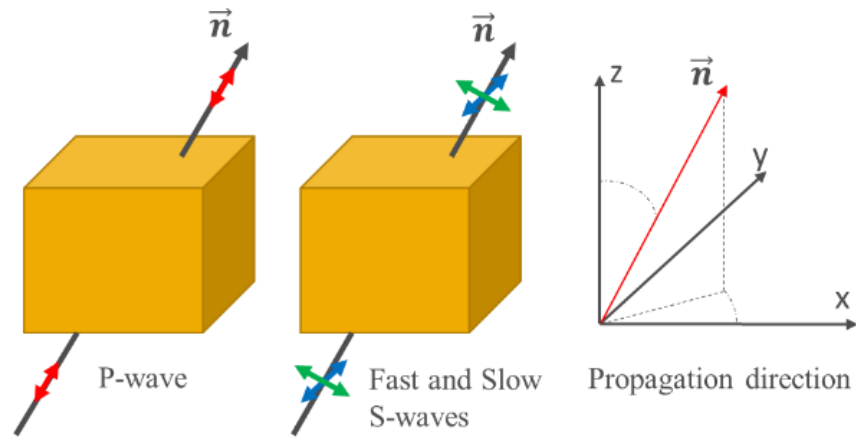


**Figure 3.12 – Polarization directions of P- and S- waves with respect to wave propagation direction  $n$**

## CHAPTER IV

### FIELD CASE STUDY

In this study, the geomechanical properties, in-situ stress distributions and seismic velocity anisotropy of a tight gas carbonate reservoir in the Tazhong area, Tarim Basin were investigated. The lower Ordovician fracture-cavity formations are the primary hydrocarbon traps and the main target formations in this study. The matrix rock in the area has overall low permeability and porosity. However, the field is located in major fault belt zones. Natural fractures are well developed in some regions along the faults and can be observed in image logs from most of the wells drilled in the area.

Establishing a comprehensive model to characterize the fractured reservoir from the geomechanical perspective can be very challenging. In this field case, an integrated approach is developed for geomechanical characterization conducted at a reservoir-scale where well ZG161, in the TZ45 block, is drilled. Detailed data analyses and interpretations and numerical simulation results on reservoir in-situ stresses, natural fracture properties, and anisotropic seismic velocities are presented in this section.

#### **4.1 Field Introduction**

##### *4.1.1 Geological description and tectonic actives of the Tazhong area*

The Tazhong area in Tarim basin as shown in Figure 4.1 covers an area of  $5 \times 10^4 \text{ km}^2$  (Jin et al. 2018). The area is divided into several structural units by the strike-slip faults in the NE direction and the thrust fault, Tazhong No. 1 Fault, in the NW direction. The forming of the Tazhong uplift provides favorable migration conduits for hydrocarbon migration and accumulation (Lan et al.

2015, Neng et al. 2008). The Cambrian – lower Ordovician source rocks in the north, and upper Ordovician carbonate source rock are two main contributors for the hydrocarbon accumulated in the Tazhong area (Wang et al. 2013).

The Lianglitage–Yingshan group in the Tazhong area is composed of Ordovician carbonates and the formations contain the major hydrocarbon-bear reservoirs in the region. The main target, Yingshan formation, is buried at 5000~6500 m, with varying thickness and an average thickness of 120 m (Zhang et al. 2007). The formation lithology mainly consists of light gray sparite calcarenite, micrite limestone, micrite calcarenite and dolomitic limestone (Liu et al. 2011).

The present-day in-situ stress around the Tarim Basin is dominated by a regional compressional tectonic stress field by the Himalayan collisional orogeny (Sun et al. 2017). The Tazhong area experienced a transition from extension to compression regime in the Caledonian orogeny during middle Ordovician. The tectonic activities developed the fractures in the formations with varying scales from microfractures to large fractures in three stages: in the Upper Ordovician, and in the uppermost 100 m of the Middle and Lower Ordovician (Ding et al. 2012).

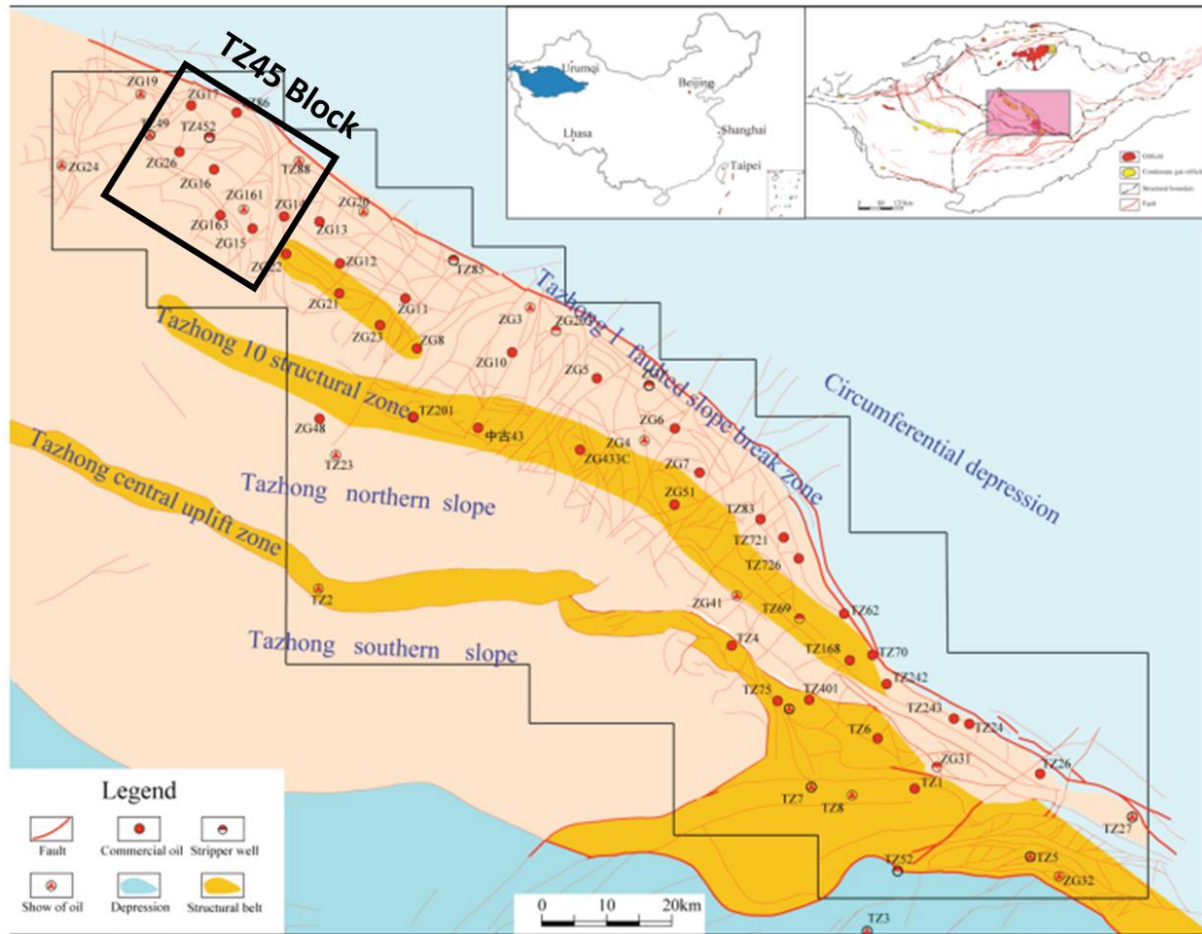


**Table 5 – Summary of static experimental data of core samples from the field**

Test No.	bulk density (g/cc)	porosity	permeability (mD)	Poisson's ratio	Young's Modulus (GPa)	Confining Pressure (MPa)
1	2.797	0.013	3.842	0.212	27.18	33
2	2.737	0.037	0.003	0.269	35.74	65
3	2.823	0.015	0.003	0.233	32.16	65
4	2.845	0.019	0.135	0.329	34.90	65
5	2.802	0.027	0.111	0.277	31.28	33
6	2.877	0.021	0.003	0.180	37.43	33
7	2.947	0.021	0.004	0.149	35.21	65
8	2.908	0.026	0.002	0.205	34.34	65
9	2.864	0.018	0.008	0.135	22.86	65
10	2.841	0.030	0.091	0.301	41.13	65
11	2.782	0.013	0.008	0.203	32.96	70
12	2.747	0.013	0.050	0.140	24.29	70
13	2.767	0.018	0.017	0.280	27.82	70
14	2.782	0.016	0.001	0.160	20.44	70
15	2.78	0.017	0.004	0.237	31.83	70
16	2.864	0.014	0.039	0.313	44.00	70
17	2.901	0.017	0.009	0.304	34.85	70

The dynamic elastic properties can be calculated once the compressional and shear wave velocities are known by using the following equations:

Shear Modulus:

$$G = \rho V_s^2 \quad (4.1)$$

Poisson's ratio:

$$v = \frac{\left(0.5 \left(\frac{V_p}{V_s}\right)^2 - 1\right)}{\left(\frac{V_p}{V_s}\right)^2 - 1} \quad (4.2)$$

Young's Modulus:

$$E = \frac{\rho V_s^2 (3V_p^2 - 4V_s^2)}{V_p^2 - V_s^2} \quad (4.3)$$



**Table 6 – Summary of dynamic experimental data of core samples from the field**

Test No.	Vp (m/s)	Vs (m/s)	Dynamic Poisson's Ratio	Dynamic Shear Modulus (GPa)	Dynamic Young's Modulus (GPa)
1	6826	3591	0.309	36	94
2	5621	3245	0.250	29	72
3	5862	2998	0.323	25	67
4	5168	2345	0.370	16	43
5	6667	3608	0.293	36	94
6	5974	3500	0.239	35	87
7	5855	3454	0.233	35	87
8	5495	3296	0.219	32	77
9	5685	3426	0.215	34	82
10	6177	3399	0.283	33	84
11	6406	3758	0.238	39	97
12	6246	3349	0.298	31	80
13	5797	3236	0.274	29	74
14	6435	3573	0.277	36	91
15	5695	3288	0.250	30	75
16	5828	3171	0.290	29	74
17	5790	3053	0.307	27	71

A correlation between dynamic and static Young's Modulus is generated and is shown in Figure 4.2. Similarly, the dynamic and static Poisson's ratio is shown in Figure 4.3.

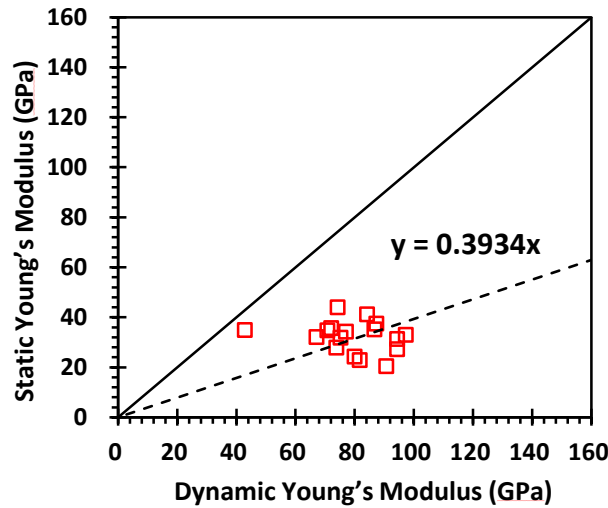


**Figure 4.2 – Correlation between dynamic and static Young's Modulus**

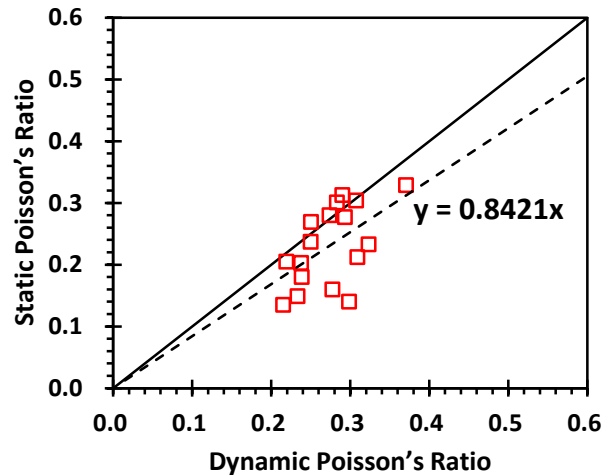


**Figure 4.3 – Correlation between dynamic and static Poisson's ratio**

Another important parameter to determine from the test analysis is the rock compressive strength. Usually, true unconfined compressive strength is obtained from uniaxial compression test. The compressive strength obtained from triaxial tests under small confining pressure can also be used to estimate unconfined compressive strength. Other methods to obtain unconfined compressive strength including extrapolate triaxial test results with different confining pressures

or derived from compression and shear wave velocities. The latter two methods may yield large uncertainty.

In this study, 6 additional triaxial tests under small confining pressure of 2 MPa were conducted. All core samples were taken from Yingshan formation in the TZ45 block. The test specimens are 50 mm in height and 25 mm in diameter in dry condition. Stresses at failure of the samples were recorded. Figure 4.4 shows a sample specimen used in the triaxial test before and after failure. The sample presents a relatively uniform lithology for the intact rock and microfractures can be observed in the sample. Figure 4.5 shows the measured stress-strain curves. The axial stress-strain curve has three distinguish regime before rapture: the nonlinear deformation at the beginning of the test due to compression on natural fractures and pores; linear elastic deformation between stress levels of 30 MPa and 100 MPa; and strain hardening when stress level exceeds the initial yield point.

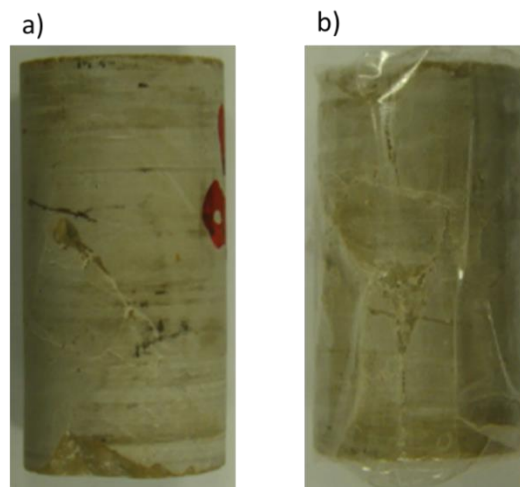


**Figure 4.4 – Core sample for triaxial test a) before the test and b) after the test. Specimen dimension: 50 mm in height, 25 mm in diameter Microfracture can be observed in the sample**

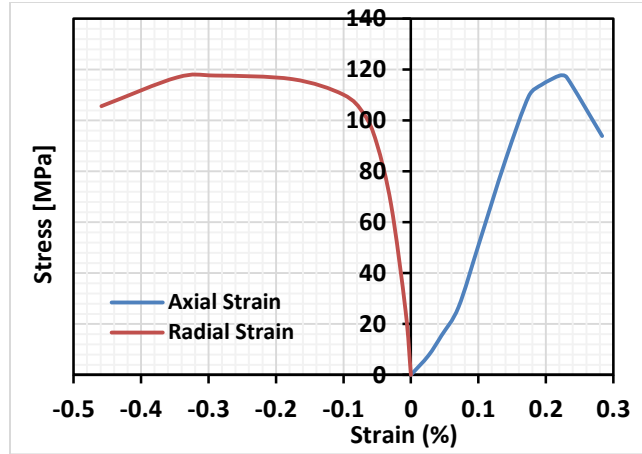


**Figure 4.5 – Stress-strain curves from triaxial test**

Figure 4.6 summarizes the ultimate rock strengths recorded from the triaxial tests and are plotted against sample shear modulus. A linear trend can be found between the shear modulus and rock strength, as shown in Equation 4.4. Additionally, three uniaxial tests were performed, the uniaxial compressive strengths measured from the tests are 23.03MPa, 30.2 MPa, and 33.4 MPa with corresponding static shear modulus of 53 GPa, 18 GPa, and 39 GPa. It is noticed that the uniaxial test results are inconsistent when compared with the correlation based on triaxial tests.

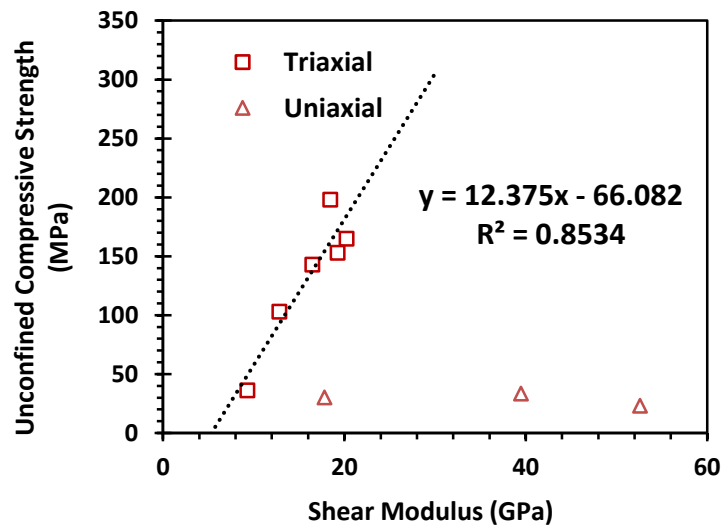


**Figure 4.6 – Experimental results on compressive strength of the rock**

Rock strength from triaxial tests:

$$\text{Rock Strength} = 12.375G - 66.082 \quad (4.4)$$

where the unit of rock strength is in MPa, and  $G$  is the shear modulus in GPa.

## 4.2 Well Data Acquisition and Interpretations

The example reservoir presented in this field study is produced by Well ZG161. Well ZG161 is a vertical well completed at 6300 m true vertical depth. The well is located in the southeast region of the TZ45 block as shown in Figure 4.7. In Figure 4.7, the red color represents the Lianglitage Formation, the yellow color represents the Yijianfang Formation and the green color represents the Yingshan Formation.

Logging data are available at the formation depth from 6050 m to 6300 m, which include image, sonic, density, and caliper logs as presented in Figure 4.8. Elastic properties such as Young's modulus and Poisson's ratio can be interpreted from the sonic and density logs and calibrated using correlations as shown in Equation 4.1 through 4.3. Rock strength can be estimated using Equation 4.4. The interpreted elastic moduli are presented in Figure 4.9.

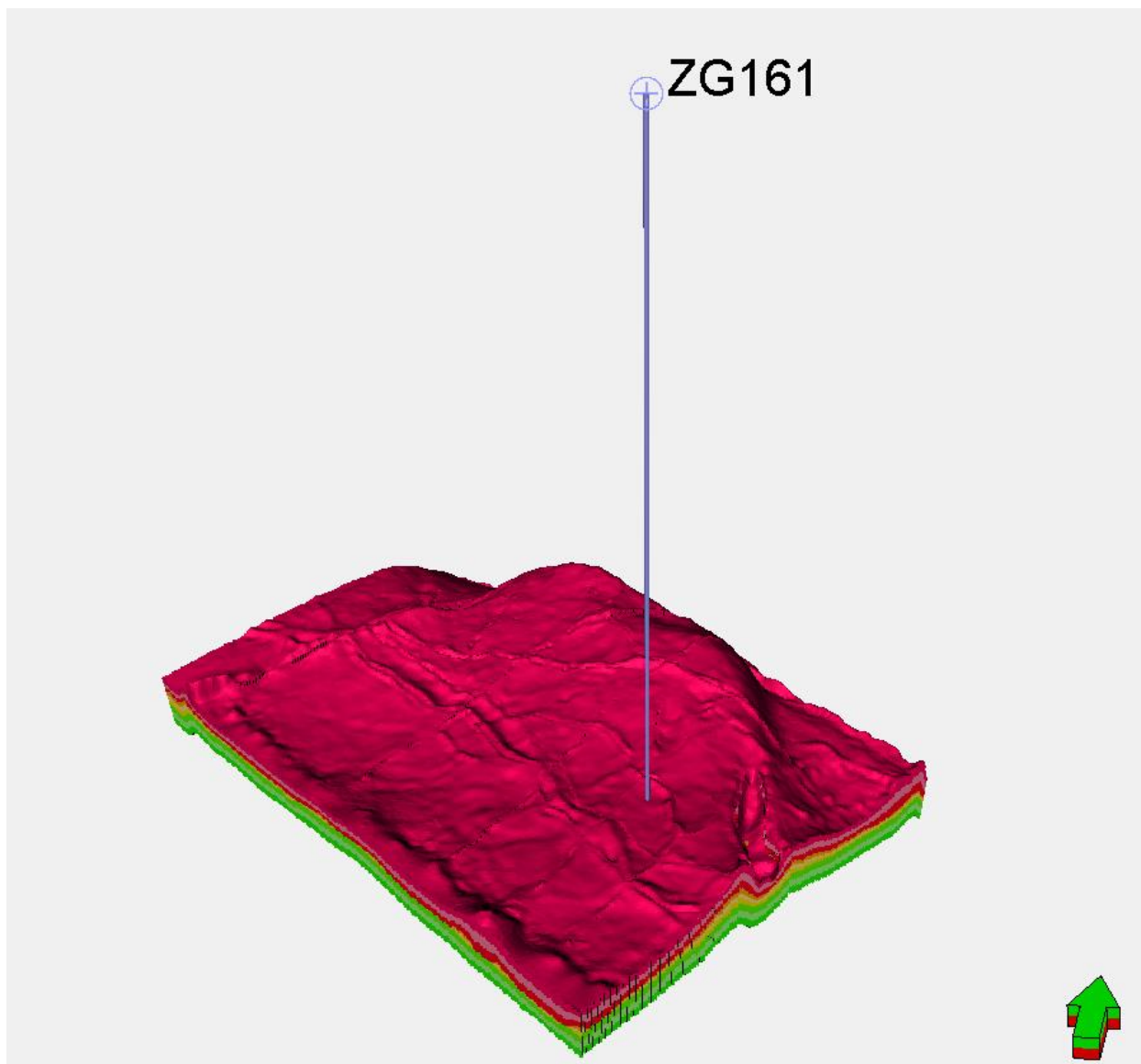


**Figure 4.7 – Location of Well ZG161 in the TZ45 block of the tight gas carbonate field**

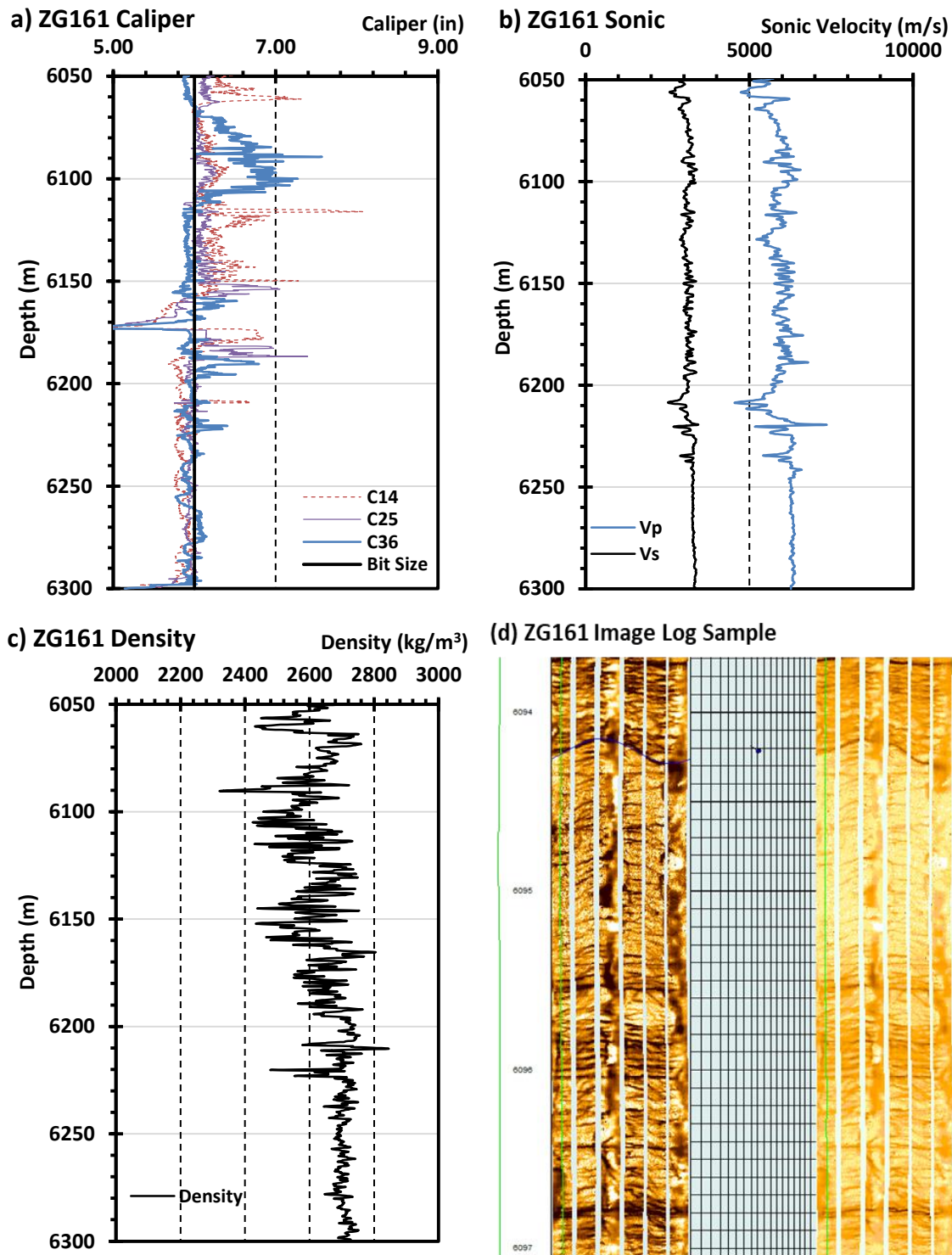
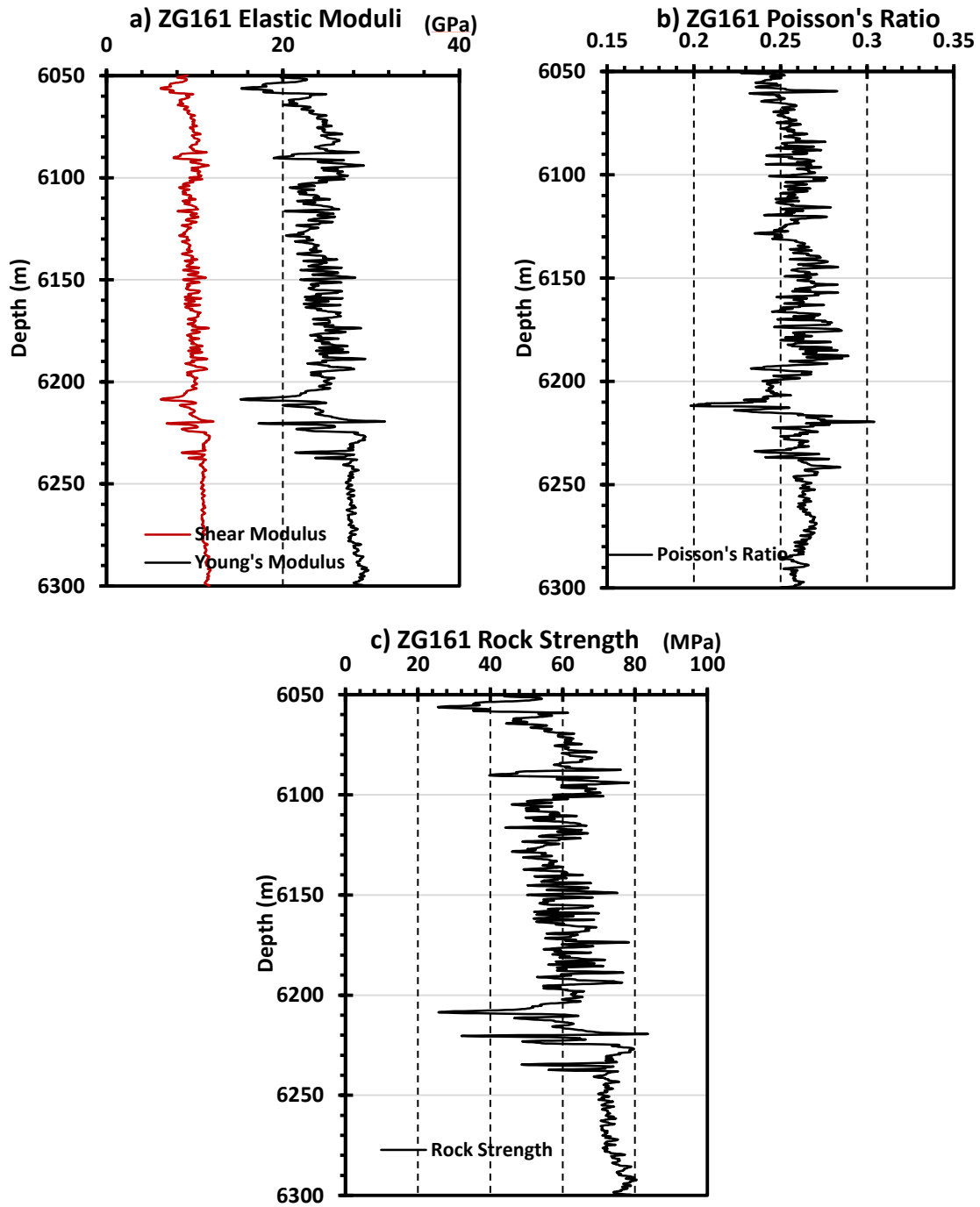


Figure 4.8– a) 6-arm caliper readings, b) sonic velocity logs, c) density log and d) sample image log from interval 6094m-6097m



**Figure 4.9 – Elastic properties interpreted from well logs. a) Young's modulus and shear modulus at the well, b) Poisson's ratio and c) rock strength**



## 4.3 Reservoir-scale Geomechanical Modeling

### 4.3.1 Geostatistical modeling of reservoir properties

The generation of a three-dimensional reservoir property model is accomplished by employing the geostatistical method. Elastic moduli distributions are populated using well data interpretations as presented in the previous section. In the TZ45 block, 11 wells scatter throughout the region. Elastic properties are generated for all 11 wells based on available well logs. The Sequential Gaussian Simulation was performed for the realizations of field-scale property distributions. The Elastic moduli distribution are presented in Figure 4.10 to 4.12. The formation throughout the field is slightly overpressured with an average formation pressure of 70 MPa.

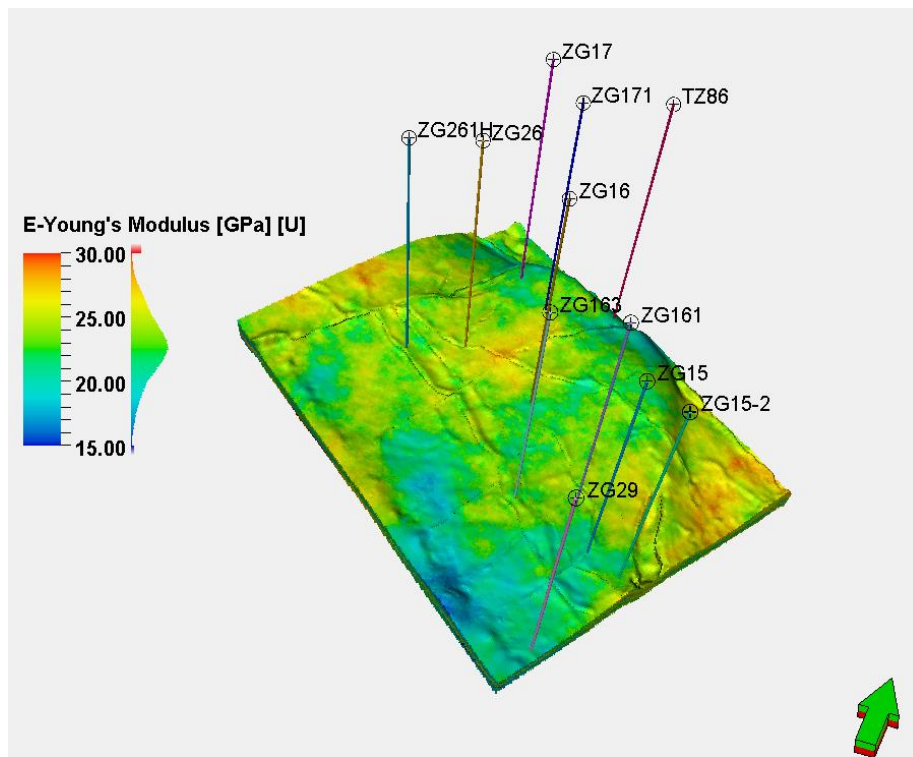


**Figure 4.10 –Young's modulus distribution of the TZ45 block**

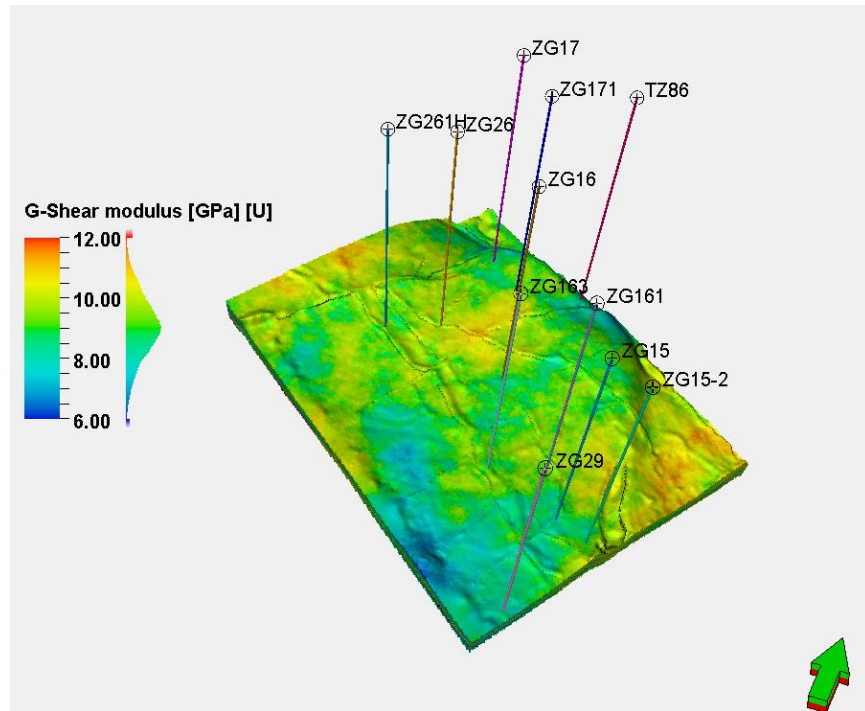


**Figure 4.11 – Shear modulus distribution of the TZ45 block**

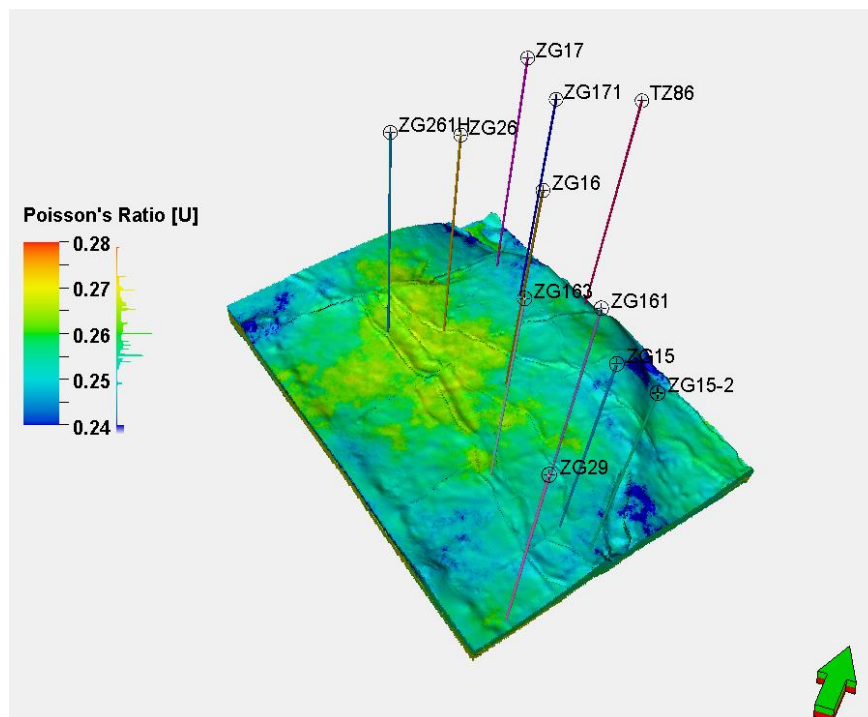


**Figure 4.12 –Poisson's ratio distribution of the TZ45 block**

In this study, the reservoir properties around Well ZG161 are extracted and assigned to a  $31 \times 31 \times 9$  simulation domain, as indicated by the red boxes in Figure 4.13, for geomechanical modeling. Well ZG161 is placed at the center of the model frame. With grid size of 100 m in x-, y-, and z-directions, the simulation domain is 3100 m in length, and 450 m in thickness.

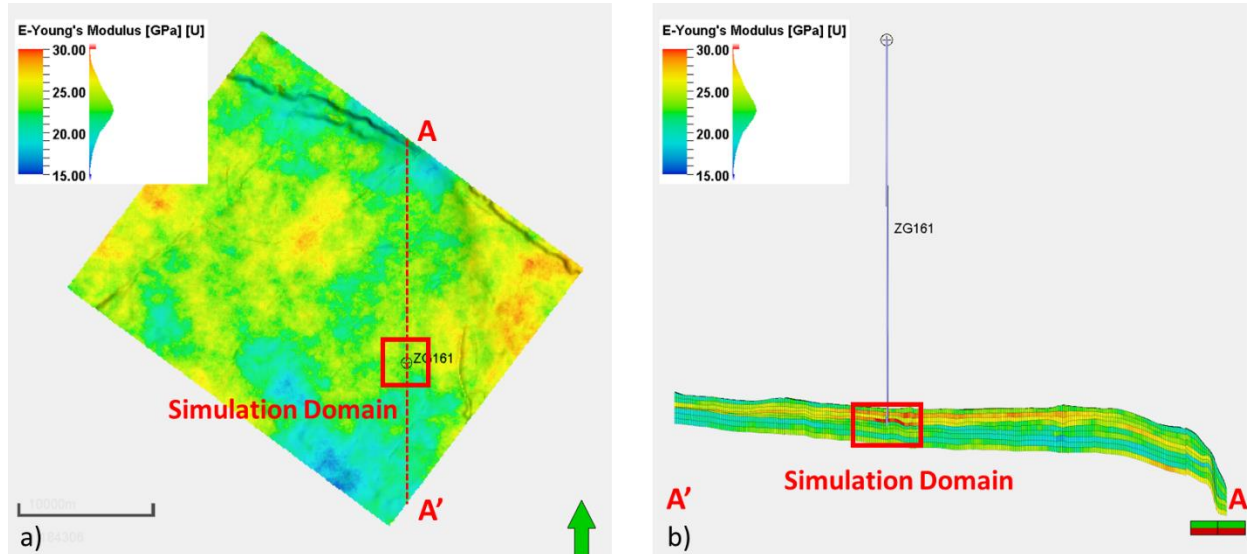


**Figure 4.13 – Simulation domain for geomechanical modeling of Well ZG161 with a) top view and b) cross-sectional view**

#### 4.3.2 Stress analysis around borehole

The stresses estimated or interpreted at near wellbore region are often served as constraints for the geomechanical model. In this study, the overburden stresses at the well location are approximated by the density logs. The overburden stress is approximately 140 MPa at the formation top at 6050 m vertical depth.

The minimum horizontal stress is interpreted from the acid fracturing treatment records. An average minimum horizontal stress of approximately 120 MPa is estimated over the stimulated depth interval from 6050 m to 6300 m.

The maximum horizontal stress at ZG161 can be interpreted by borehole breakouts identified from image logs as shown in Figure 4.14. From Figure 4.14, the spacing of the major natural fractures can also be identified, which is approximately 1 meter. The dip angle and dip direction are  $45^{\circ}$  and N45W respectively. A summary of the breakout intervals along the borehole at target formation is illustrated in Figure 4.15.

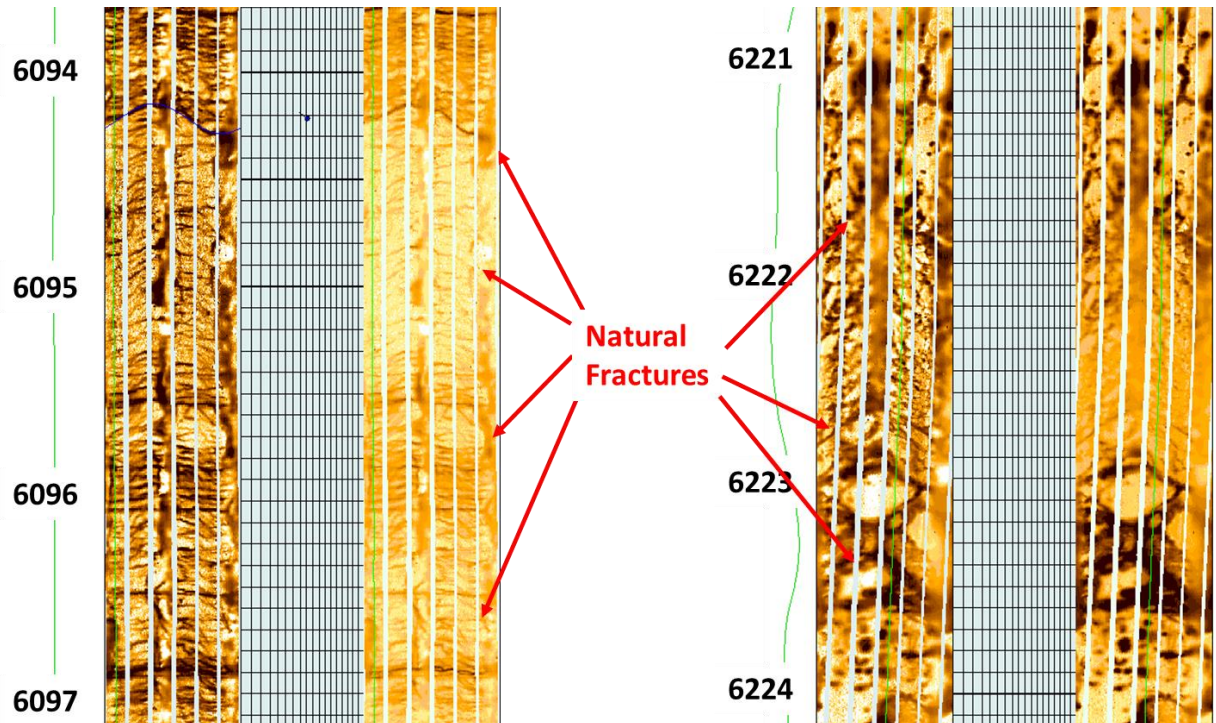


**Figure 4.14 – Examples of natural fractures observed from image logs at intervals 6094m-6097m and 6221m-6224m**

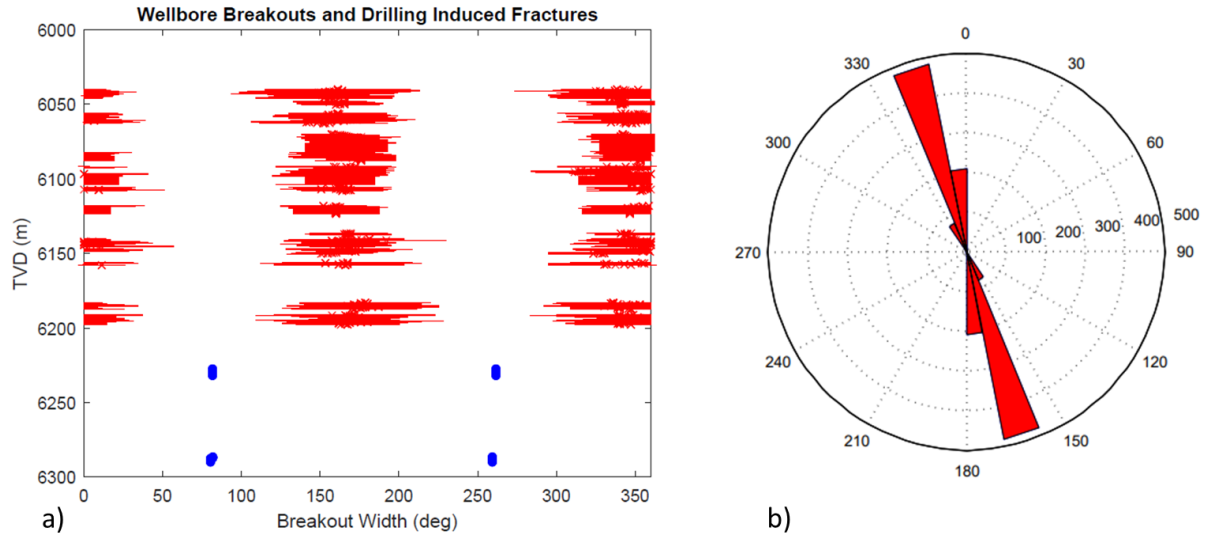


**Figure 4.15 – a) ZG161 Breakouts intervals identified from image log showing as red lines. b) Rose diagram showing the azimuth of centers of borehole breakouts, 0° indicates north.**

It is observed from Figure 4.15 that the average azimuth of the breakout centers is N15W and N165E, and the breakout angles range from 80 to 100 degrees. The drilling induced fractures occur symmetrically at azimuth N90E and N90W, indicating the minimum horizontal stress is orientated in the E-W direction.

To estimate the maximum horizontal stress at the wellbore, the borehole stability model is used to simulate the stress distributions and predict the borehole failure regions. The boundary conditions and input parameters used for the borehole stability analysis is listed in Table 7 and Table 8. In this simulation, the fracture normal and shear stiffnesses are assumed to be half of the average intact rock Young's modulus and shear modulus. The maximum allowable fracture normal displacement is assumed to be 200 micrometers.

**Table 7 – Simulation parameters of boundary conditions and intact rock**

Stress in E-W Direction $\sigma_x$ , [MPa]	120
Stress in N-S Direction $\sigma_y$ , [MPa]	130
Vertical Stress $\sigma_z$ , [MPa]	140
Formation Pressure, $p_p$	70
Wellbore Pressure $P_w$ [MPa]	73
Average Young's Modulus E, [GPa]	25
Poisson's ratio $\nu$	0.26
Rock Cohesive Strength $C_o$ , [MPa]	15
Friction Coefficient $\mu_o$	0.7

**Table 8 – Simulation parameters of natural fractures**

Fracture Normal Stiffness $K_n$ , [GPa/m]	12.5
Fracture Shear Stiffness $K_s$ , [GPa/m]	5
Fracture dip direction $\alpha$	135°
Fracture inclination angle $\beta$	45°
Fracture Spacing $s_f$ , [m]	1
Maximum Fracture Closure $v_m$ , [m]	2e-4
Fracture Cohesive Strength $C_f$ , [MPa]	5
Friction Coefficient $\mu_o$	0.45

With the maximum horizontal stress of 130 MPa orientating in N-S direction, the projected wellbore failure areas are simulated, and the result is presented in Figure 4.16. The failure areas have an angle of 90 degree with the center of the failure at approximately N10W. The maximum failure depth is approximately 0.35 inches. The shape of the failure area is compared with the breakout interpretations from image log as shown in red boxes in Figure 4.16. The image shown in the figure starts from the north direction and ends in the north direction. From the interpretation, the breakout widths azimuths are approximately from N55W to N45E and from S55E to S45W. As shown in the caliper log, based on a 6-inch drill bit, the total depth of the failure at interval 6095 m – 6100 m ranges from 0.7 inch to 1 inch. Compares with the log measurements, the simulation provided reasonable results.



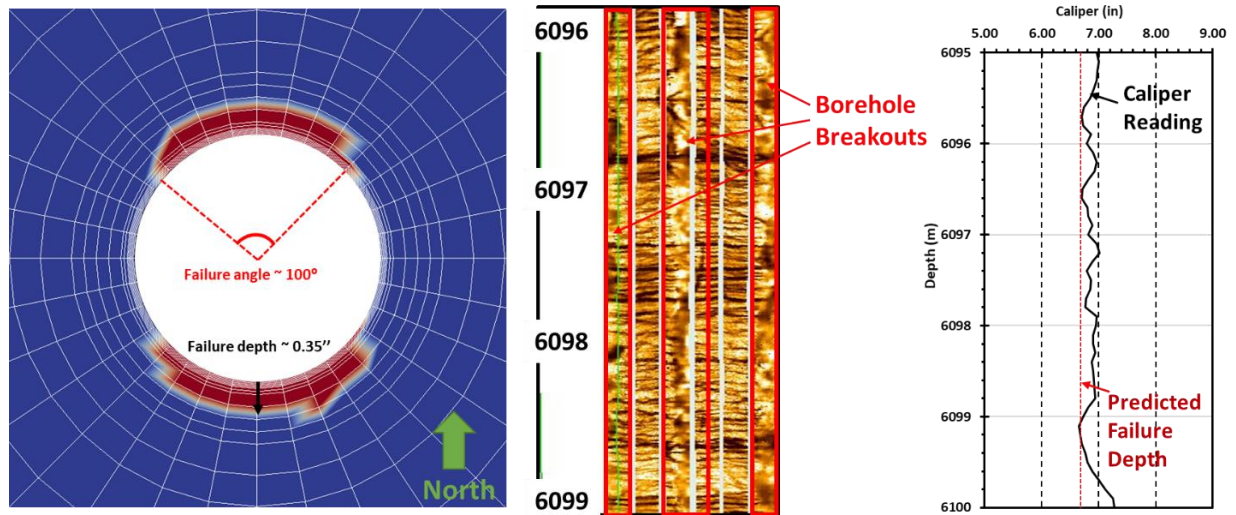


**Figure 4.16 – Projected borehole failure area from simulation result with minimum horizontal stress  $\sigma_h = 120\text{MPa}$ , maximum horizontal stress  $\sigma_h = 130\text{MPa}$ , and vertical stress  $\sigma_v = 140\text{MPa}$  (left) An example of borehole breakout interpretation from image log at interval 6096 m – 6099 m (middle) Caliper Measurement of the borehole at interval 6095 m – 6100 m (right).**

#### 4.3.3 Reservoir geomechanical modeling

The structure of the reservoir used in geomechanical modeling is assumed to be rectangular shape with 31 grid blocks in both the x-, and the y-directions over 3100 m, and 9 grid blocks in the z-direction for the formation thickness of 450 m. One set of natural fractures is implemented in the geomechanical model. The fracture initial normal and shear stiffness of 10 GPa/m and 5 GPa/m. The fracture spacing is 1 m. The fracture aperture is assumed to be 200 micrometers and the maximum allowable normal displacement is 90% of the fracture aperture. The fracture dip angle and dip direction are 45° and N45W, which is the same setting as for wellbore stability model. The mechanical properties of the intact rock are extracted from the geostatistical model described in section 4.3.1. Figure 4.17 shows the Young's modulus distribution of the simulation

domain. The boundary and initial conditions are shown in Figure 4.18. The model bottom is fixed in the vertical direction, but displacements in the horizontal directions are allowed.

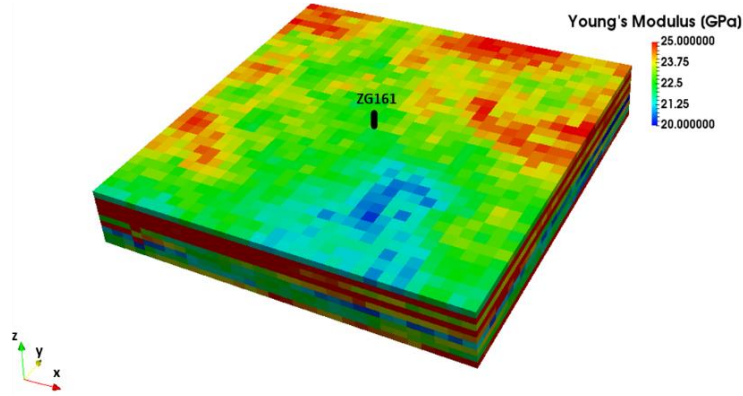


**Figure 4.17 – Young's modulus distribution of the simulation domain**

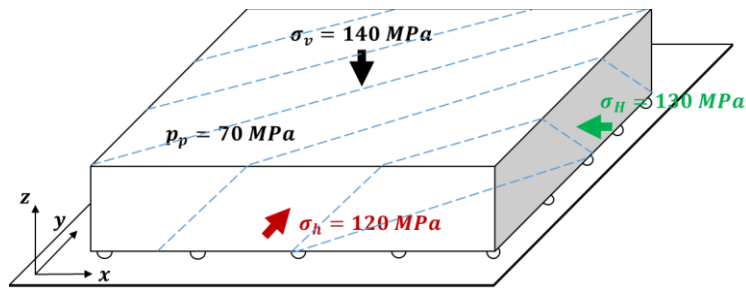


**Figure 4.18 – Boundary conditions for the reservoir geomechanical model. The bottom of the model is fixed in the vertical direction, but movement is allowed in the horizontal direction**

To better understand the stress perturbation due to the presence of natural fractures, the geomechanical modeling is first performed on the base case, isotropic linear elastic formation without considering natural fractures. In this case, the effective maximum and minimum horizontal stress distributions are simulated and presented in Figure 4.19. If natural fractures are considered, the formation rock mass becomes anisotropic nonlinear elastic. The in-situ stress distributions are simulated and presented in Figure 4.20.



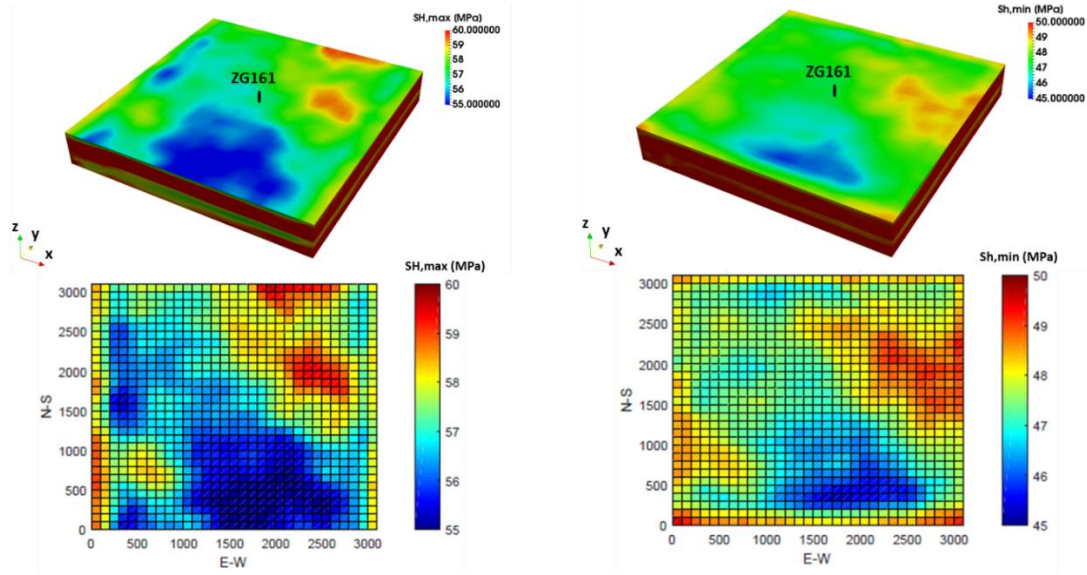


**Figure 4.19 – a) Simulated maximum effective horizontal stress distribution and b) simulated minimum effective horizontal stress distribution, assuming isotropic elastic formation without effect of natural fractures**

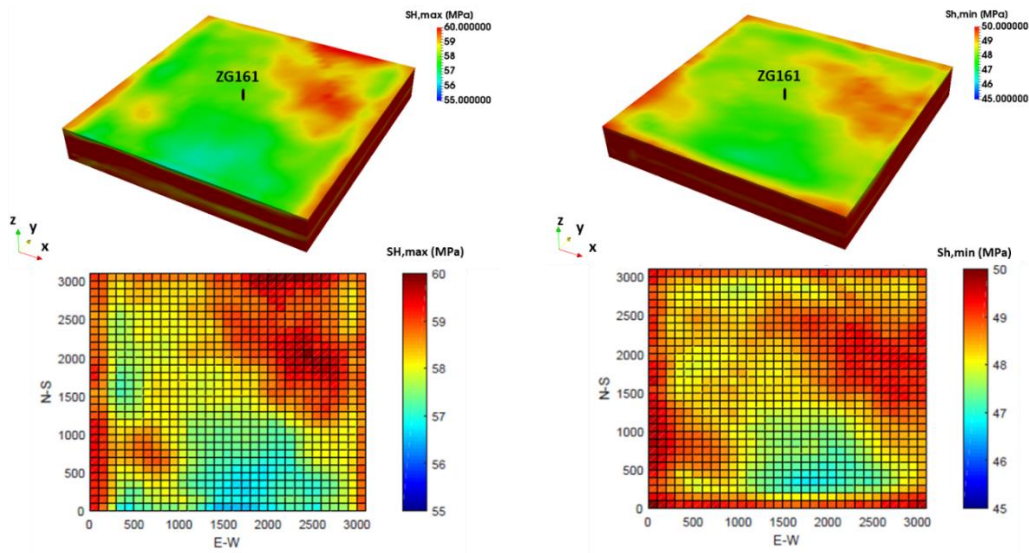


**Figure 4.20 – a) Simulated maximum effective horizontal stress distribution and b) simulated minimum effective horizontal stress distribution, assuming anisotropic nonlinear elastic formation with effect of natural fractures**

Figure 4.21 compares the simulated horizontal stresses at the well location from the two cases. The model results show that stress curves are smoother in the anisotropic nonlinear elastic case given the same modeling conditions.

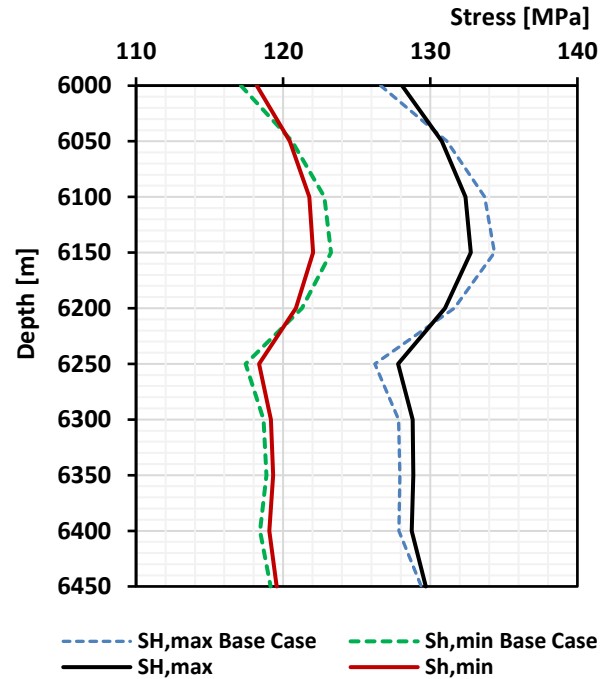


**Figure 4.21 – Comparison of the simulated minimum and maximum horizontal stresses at the well location with and without effect of natural fractures.**

Figure 4.22 shows the simulated effective horizontal stress ratios for both cases. By assuming formation is isotropic elastic, and the impact of natural fractures is neglected, the stress ratio of two horizontal principal stresses throughout the reservoir ranges from 1.14 to 1.26. For the anisotropic nonlinear elastic case, the simulation result yields a horizontal stress ratio ranging from 1.152 to 1.247. The horizontal stress anisotropy has great influence on the hydraulic fracturing treatment in fractured reservoirs. With more prominent horizontal stress anisotropy, the fracturing treatment creates a predominant bi-wing fracture, whereas, with less stress anisotropy, the

treatment creates a more complex fracture network. Knowing the horizontal stress ratio of the field can help on well planning and well stimulation design.

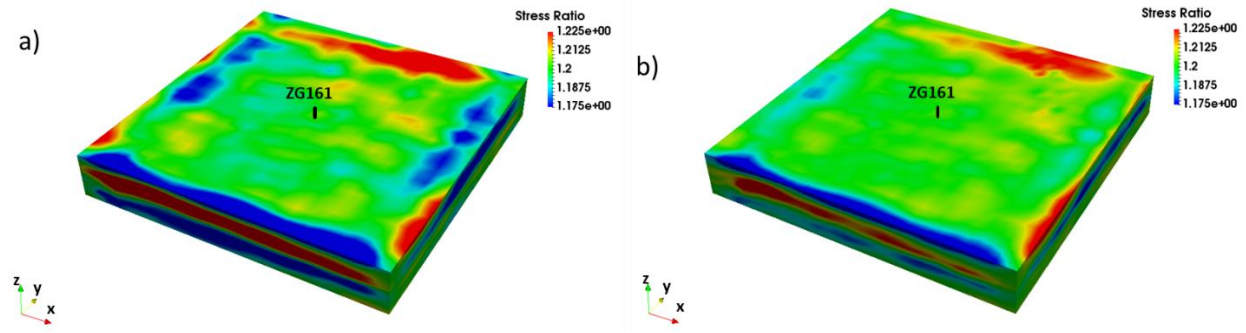


**Figure 4.22 – Comparison of simulated horizontal stress ratio between the two cases. a) Isotropic elastic formation, b) anisotropic nonlinear elastic formation**

The natural fracture apertures throughout the reservoir are updated during the simulation as shown in Figure 4.23. Under the given boundary condition and initial fracture properties, the final fracture aperture ranges from 25 micrometers to 28 micrometers, which is equivalent to 12% to 14% of the initial aperture. The knowledge of fracture aperture throughout the field can provide information for reservoir flow simulations in fractured reservoirs where rock permeability is controlled by the presence of open fractures.

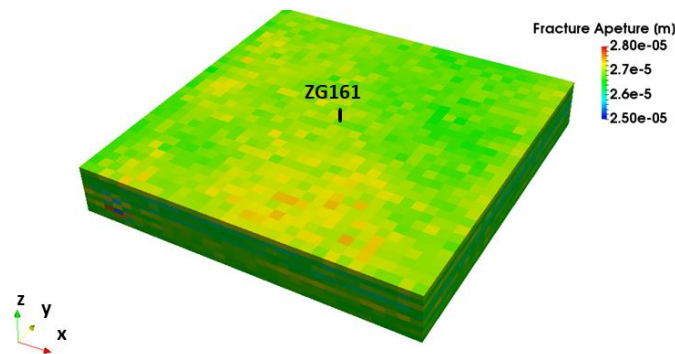


**Figure 4.23 – Simulated fracture aperture distribution**

#### 4.3.4 Seismic velocity modeling

The P- and S-wave velocities of the field can be generated using the anisotropic seismic velocity model described in section 3.4. If the reservoir rock has isotropic elastic properties, the wave propagates with the same velocity in all directions. Figure 4.24 shows the p- and s-wave velocity across of the reservoir assuming isotropic elastic rock properties.

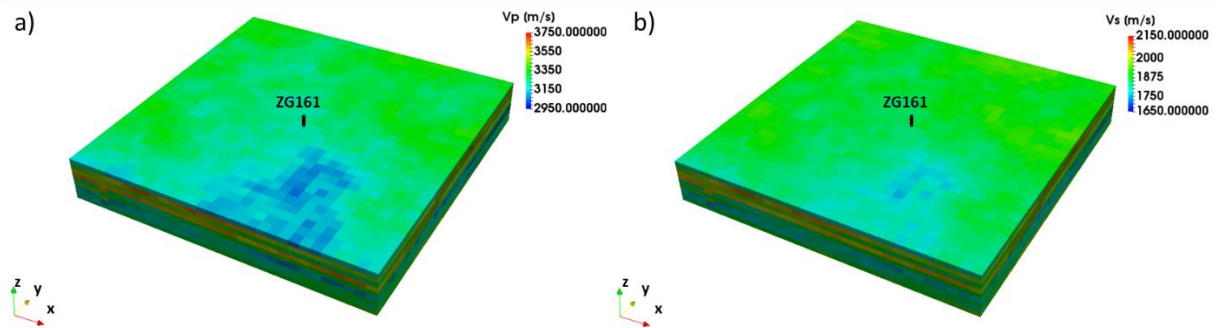


**Figure 4.24 – a) Simulated p-wave velocity and b) simulated s-wave velocity throughout the reservoir assuming isotropic elastic formation**

Figure 4.25 presents the seismic velocities simulated in the naturally fracture reservoir. From the simulation results, when the p-wave propagation direction is parallel to natural fractures, the velocity ranges from 2950 m/s to 3750 m/s, whereas for the p-wave propagating perpendicular through natural fractures, the velocity decreases to 2680 m/s to 3330 m/s. For comparison purpose, the scale of the velocity plots in Figure 4.25 a) and b) is unified from 2700 m/s to 3700 m/s. The anisotropy of the formation elastic properties also causes shear wave splitting as shown in Figure 4.25 c) and d). Plot c) and d) show the fast s-wave and slow s-wave velocity distributions when the wave propagation is in the direction parallel to the natural fractures. The slow s-wave velocity ranges from 1030 m/s to 1090 m/s, whereas the fast s-wave velocity ranges from 1450 m/s to 1750 m/s.

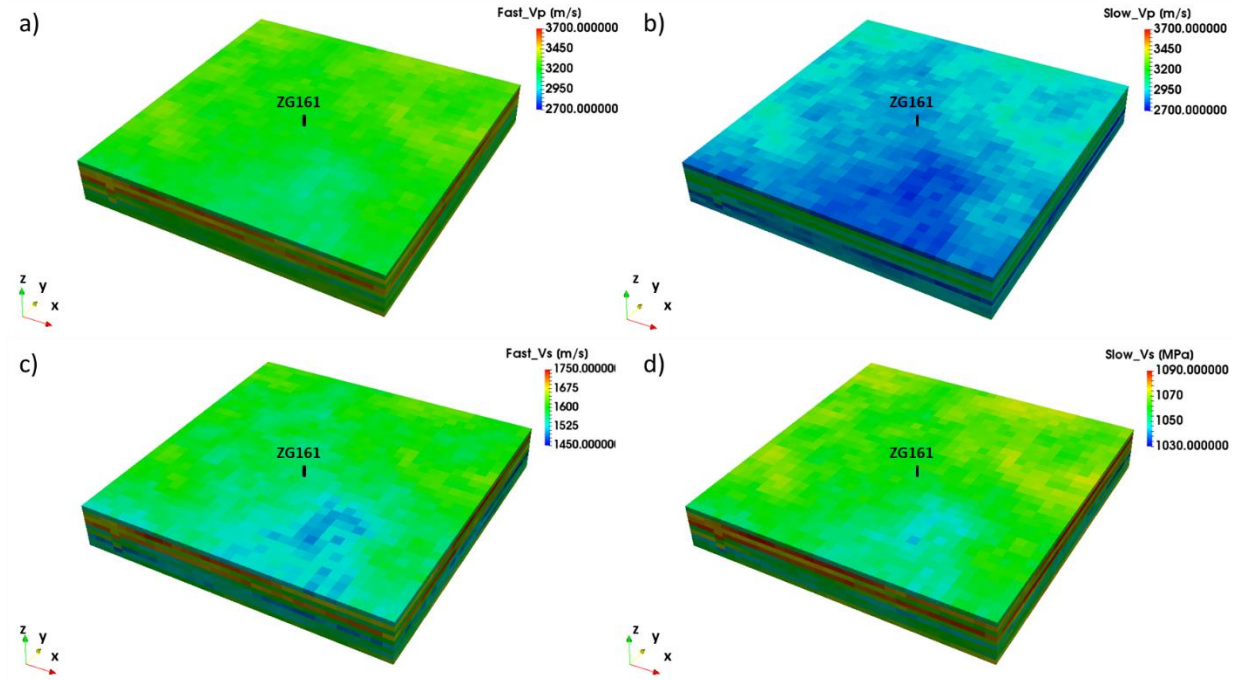


**Figure 4.25 – Simulated seismic wave velocities throughout the reservoir assuming anisotropic elastic formation a) fast p-wave velocity, wave propagates parallel to natural fractures b) slow p-wave velocity, wave propagates through natural fractures c) fast s-wave velocity and d) slow s-wave velocity, both s-wave velocities are for wave propagates parallel to natural fractures**

## CHAPTER V

### CONCLUSIONS

In this study, an integrated approach for geomechanical characterization of naturally fractured reservoirs is presented. The models presented provide a more reliable approach on estimations in in-situ stress field and geomechanical attributes of naturally fractured reservoirs by linking wellbore-scale, reservoir-scale, and seismic attributes simulations together.

The simulation results in the field study indicate that under certain stress conditions and natural fracture properties, using non-linear anisotropic elastic geomechanical model, the horizontal stress ratio is predicted to have a narrower range comparing with results from a conventional isotropic linear elastic model.

If anisotropic seismic velocity measurements are available, it could be useful resources for mapping geomechanical properties in naturally fractured reservoirs. In case those measurements are not accessible, using this geomechanical characterization model with careful implementation of natural fracture properties in the model, the anisotropic seismic velocities (one P-wave and two S-wave velocities) can be estimated.

Fracture aperture in fractured reservoirs is directly related to enhanced permeability zones. Our integrated approach for geomechanical characterization helps to locate open fractures. Knowledge such as fracture aperture and fracture stiffness under in-situ stress state is also beneficial in calculating fluid-flow behavior of naturally fractured reservoirs.

## REFERENCES

- Aadnoy, B.S., 1988. Modeling of the Stability of Highly Inclined Borehole in Anisotropic Rock Formations. *SPE Drilling Eng.* 3(3), 259-268.
- Amadei, B. and Goodman, R.E., 1981a. A 3-D Constitutive Relation for Fractured Rock Masses. *Proceedings of the International Symposium on the Mechanical Behavior of Structured Media*, Ottawa Part B, 249-268.
- Amadei, B. and Goodman, R.E., 1981b. Formulation on of Complete Plane Strain Problems for Regularly Jointed Rocks. *Proceedings of 22<sup>nd</sup> U.S. Symposium on Rock Mechanics*, Cambridge, Massachusetts.
- Amadei, B., 1983. Rock Anisotropy and the Theory of Stress Measurements. Springer, Berlin.
- Ameen, M.S., MacPherson, K., Al-Marhoon, M.I., and Rahim, Z., 2012. Diverse Fracture Properties and Their Impact on Performance in Conventional and Tight-Gas Reservoirs, Saudi Arabia: The Unayzah, South Haradh Case Study. *AAPG Bulletin* 96(3), 459-492.
- Bagheri, M. and Settari, A., 2008. Modeling of Geomechanics in Naturally Fractured Reservoirs. *SPE Reserv. Eval. Eng.* 11(1), 108-118.
- Barton, N. 1973. Review of a New Shear-Strength Criterion for Rock Joints. *Eng. Geol.* 7(4), 287-232.
- Barton, N., Bandis, S.C., and Bakhtar, K., 1985. Strength, Deformation and Conductivity Coupling of Rock Joints. *Int. J. Rock Mech. Min. Sci. Geomech. Abstr.* 22(3), 121-140.
- Bandis, S.C., Lumsden, A.D., Barton, N.R., 1983. Fundamentals of Rock Joint Deformation. *Int. J. Rock Mech. Min. Sci. Geomech. Abstr.* 20(6), 249-268.

- Bell, J.S. and Gough, D.I., 1979. Northeast-Southwest Compressive Stress in Alberta: Evidence from Oil Wells. *Earth Planet Sci. Lett.* 45, 475-482.
- Bradley, W.B., 1979. Failure of Inclined Boreholes. *J. Energy Resour. Technol. Trans. ASME* 101(4), 232-239.
- Brown, S.R. and Scholz, C.H., 1985. Broad Bandwidth Study of the Topography of Natural Rock Surfaces. *Journal of Geophysical Research* 90(B14), 12575-12582.
- Cai, M. and Horii, H., 1992. A Constitutive Model of Highly Jointed Rock Masses. *Mechanics of Materials* 13, 217-246.
- Chen, H.Y. and Teufel, L.W., 1997. Coupling Fluid-Flow and Geomechanics in Dual-Porosity Modeling of Naturally Fractured Reservoirs. SPE paper presented at the SPE Annual Technical Conference and Exhibition. San Antonio Texas, U.S.A. 5-8 October 1997.
- Cook, B.K. and Jensen, R.P., 2002. Discrete Element Method: Numerical Modeling of Discontinua. *Proceedings of the Third International Conference on Discrete Element Methods*. Santa Fe, New Mexico.
- Cui, L., Cheng, A.H.-D., and Abousleiman, Y., 1997. Poroelastic Solution of an Inclined Borehole. *ASME J. Appl. Mech.* 64, 32-38.
- Cundall, P.A., 1971. A Computer Model for Simulating Progressive, Large Scale Movements in Blocky Rock Systems. *Proceedings of Symposium of International Society of Rock Mechanics*. Nancy.
- Cundall, P.A. and Strack, O.D.L., 1979. A Discrete Numerical Model for Granular Assemblies. *Geotechnique* 29(1), 47-65.



- Cundall, P. and Lemos, J.V., 1988. Numerical Simulation of Fault Instabilities with a Continuously-Yielding Joint Model. *Proceedings of the 2<sup>nd</sup> International Symposium on Rockbursts and Seismicity in Mines*. Minneapolis.
- Daniels, J., Waters, G., LeCalvez, J., Lassek, J. and Bentley, D., 2007. Contacting More of the Barnett Shale Through and Integration of Real-Time Microseismic Monitoring, Petrophysics and Hydraulic Fracture Design. SPE paper presented at the 2007 SPE Annual Technical Conference and Exhibition. Anaheim California, U.S.A., 12-14 October 2007.
- Detournay, E. and Cheng, AH-D., 1988. Poroelastic Response of a Borehole in a Non-hydrostatic Stress Field. *Int. J. Rock Mech. Min. Sci Geomech. Abstr.* 25(3), 171-182.
- Ding, W., Fan, T., Yu, B., Huang, X., and Liu, C., 2012. Ordovician Carbonate Reservoir Fracture Characteristics and Fracture Distribution Forecasting in the Tazhong Area of Tarim Basin, Northwest China. *J. Pet. Sci. Eng.* 86(87), 62-70.
- Fairhurst, C., 1968. Methods of Determining in Situ Rock Stresses at Great Depths. *Technical Report TRI-68. US Army Corps of Engineers*.
- Gerrard, C.M., 1982. Elastic Models of Rock Masses Having One, Two and Three Sets of Joints. *Int. J. Rock Mech. Min. Sci Geomech. Abstr.* 19, 285-305.
- Goodman, R.E., 1976. Methods of Geological Engineering in Discontinuous Rocks. San Francisco. West Publishing Company.
- Goodman, R.E. and Shi, G., 1985. Block Theory and its Application to Rock Engineering. Prentice-Hall Englewood Cliffs, NJ.
- Greenwood, J.A. and Williamson, J.B.P., 1966. Contact of Nominally Flat Surfaces. *Proceedings of the Royal Society A: Mathematical, Physical and Engineering Sciences* 295(142), 300-319.

- Helbig, K., 1994, Foundations of anisotropy for exploration seismics, Handbook of geophysical exploration Section 1 — Seismic exploration, vol. 22: Pergamon.
- Henyey, F.S. and Pomphrey, N., 1982. Self-Consistent Moduli of a Fractured Solid. *Geophys. Res. Lett.* 9, 903-906.
- Huang, T.H., Chang, C.S., Yang, Z.Y., 1995. Elastic Moduli for Fractured Rock Mass. *Rock Mech. Rock Eng.* 28(3), 135-144.
- Hudson, J.A., 1980. Overall Properties of a Fractured Solid. *Proceedings of the Cambridge Philosophical Society* 88, 371–384.
- Hudson, J.A., 1981. Wave Speeds and Attenuation of Elastic Waves in Material Containing Fractures. *Geophysical Journal of the Royal Astronomical Society*, 64, 133–150.
- Hudson, J.A., 1991. Overall Properties of Heterogeneous Material. *Geophys. J. Int.* 107, 505-511.
- Jaeger, J., Cook, N., and Zimmerman, R., 2007. Fundamentals of Rock Mechanics (Fourth ed.). Blackwell Publishing Ltd.
- Jebahi, M., Andre, D., Lordanoff, I., and Terreros, I., 2015. Discrete Element Method to Model 3D Continuous Material. John Wiley & Sons Inc.
- Jin, W., Cui, Z., and Ye, Z., 2018. Tectonic Characteristic and Origin of Tazhong Uplift, Tarim Basin. *Proceedings of 2018 International Conference on Energy, Power and Materials Engineering*.
- Karami, A. and Stread, D., 2008. Asperity Degradation and Damage in the Direct Shear Test: A Hybrid FEM/DEM Approach. *Rock Mech. Rock Eng.* 41(2): 229-266.
- Kresse, O., Cohen, C., Weng, X., Wu, R., and Gu, H., 2011. Numerical Modeling of Hydraulic Fracturing in Naturally Fractured Formations. Presented at the 45th US Rock Mechanics/Geomechanics Symposium. Francisco California, U.S.A. 26-29 June 2011.

- Kirsch, E.G., 1898. Die Theorie der Elastizität und die Bedürfnisse der Festigkeitslehre. *Zeitschrift des Vereines deutscher Ingenieure*, 42(29), 797-807.
- Ladanyi, B. and Archambault, G., 1969. Simulation of Shear Behavior of a Jointed Rock Mass. *Proceedings of the Symposium on Rock Mechanics*, Berkeley, CA.
- Lan, X., Lu, X., Zhu, Y., and Yu, H., 2015. The Geometry and Origin of Strike-Slip Faults Cutting the Tazhong Low Rise Megaanticline (Central Uplift, Tarim Basin, China) and Their Control on Hydrocarbon Distribution in Carbonate Reservoirs. *J. Nat. Gas Sci. Eng.* 22, 633-645.
- Lee, H., Ong, S.H., Azeemuddin, M., and Goodman, H., 2012. A Wellbore Stability Model for Formations with Anisotropic Rock Strengths. *J. Pet. Sci. Eng.* 96 (97), 109-119.
- Lekhnitskii, S.G., 1963. Theory of Elasticity of an Anisotropic Body. Moscow: MIR Publisher.
- Liu, M., Jin, Y., Lu, Y. Chen, M., Hou, B., Chen, W. Wen, X., and Yu, X., 2016. A Wellbore Stability Model for a Deviated Well in a Transversely Isotropic Formation Considering Poroelastic Effects. *Rock Mech. Rock Eng.* 49, 3671-3686.
- Liu, X., Wang, X., Han, J., Jiao, W., Yu, H., and Yue, Z., 2011. Hydrocarbon Play of Ordovician Carbonate Dominated By Faulting and Karstification – A Case Study of Yingshan Formation on North Slope of Tazhong Area in Tarim Basin, NW China. *Energy Exploration and Exploitation*, 29, 743-758.
- Luthi, S.M. and Souhaite, P., 1990. Fracture Apertures from Electrical Borehole Scans. *Geophysics*. 55(7), 821-833.
- Makel, G.H., 2007. The Modelling of Fractured Reservoirs: Constraints and Potential for Fracture Network Geometry and Hydraulics Analysis. Structurally Complex Reservoirs. London: Geological Society. Special Publications, 292, 375-403.

- Maury, V. and Zurdo, C. 1996. Drilling-Induced Lateral Shifts Along Pre-Existing Fractures: A Common Cause of Drilling Problems. *SPE Drilling and Completion*. 11(1), 17-24.
- Mavko, G., Mukerji, T., and Godfrey, N., 1995. Predicting Stress Induced Velocity Anisotropy in Rocks. *Geophysics*, 60, 1081–1087.
- Mavko, G. and Nur, A. 1978. The Effect of Non-Elliptical Fractures on the Compressibility of Rocks. *J. Geophys. Res.* 83, 4459-4468
- Maxwell, S.C., Urbancic, T.I., Steinsberger, N. and Zinno, R., 2002. Microseismic Imaging of Hydraulic Fracture Complexity in the Barnett Shale. SPE paper presented at the SPE Annual Conference and Exhibition. San Antonio Texas, U.S.A. 29 September-2 October 2002.
- McLamore, R., Gray, K.E., 1967. The mechanical behavior of transversely isotropic sedimentary rocks. *Transactions in American Society of Mechanical Engineering Series B*, 62-76.
- Misra, A. 1999. Micromechanical Model for Anisotropic Rock Joints. *J. Geophys. Res. Solid Earth*, 104(B10): 23175-23187.
- Neng, Y., Yang, H., and Deng, X., 2008. Structural Patterns of Fault Damage Zones in Carbonate Rocks and Their Influences on Petroleum Accumulation in Tazhong Paleo-Uplift, Tarim Basin, NW China. *Petroleum Exploration and Development*, 45, 43-54.
- Nur, A. and Simmons, G., 1969. Stress Induced Velocity Anisotropy in Rock: An Experimental Study. *J. Geophys. Res.* 74, 6667-6674.
- Nur, A., 1971. Effects of Stress on Velocity Anisotropy in Rocks with Fractures. *J. Geophys. Res.* 76(8), 2022–2034.
- O'Connell, R.J. and Budiansky, B., 1974. Seismic Velocities in Dry and Saturated Fractured Solids. *J. Geophys. Res.* 79, 5412-5426.

- Saeidi, O., Rasouli, V., Vaneghi, R.G., Gholami, R. and Torabi, R.G., 2014. A modified failure criterion for transversely isotropic rocks. *Geoscience Frontiers*. 5(2), 215-225.
- Ong, S. and Roegiers, J.C., 1993. Influence of Anisotropies in Borehole Stability. *Int. J. Rock Mech. Min. Sci.* 30(7), 1069-1075.
- Patton, F.D., 1966. Multiple Modes of Shear Failure in Rock. *Proceedings of the First Congress of International Society of Rock Mechanics*, Lisbon. Vol 1, 509-513.
- Peska, P. and Zoback, M.D., 1995. Observations of Borehole Breakouts and Tensile Wall-Fractures in Deviated Boreholes: A Technique to Constrain in Situ Stress and Rock Strength. *Proceedings of the 35 U.S. Symposium on Rock Mechanics*.
- Plumb, R.A. and Hickman, S.H., 1985. Stress-Induced Borehole Elongation: A Comparison Between the Four-Arm Dipmeter and the Borehole Televiewer in the Auburn Geothermal Well. *J. Geophys. Res.*, 90, 5513-5521.
- Pomeroy, C.D., Hobbs, D.W., Mahmoud, A., 1971. The Effect of Weakness Plane Orientation on the Fracture of Barnsley Hard Coal by Triaxial Compression. *Int. J. Rock Mech. Min. Sci.* 8, 227-238.
- Priest, S.D., 1993. Discontinuity Analysis for Rock Engineering. Chapman & Hall.
- Prioul, R. Bakulin, A., and Bakulin, V., 2004. Nonlinear Rock Physics Model for Estimation of 3-D Subsurface Stress in Anisotropic Formations: Theory and Laboratory Verification. *Geophysics*. 69, 415-425.
- Prioul, R., and Lebrat, T., 2004. Calibration of Velocity-Stress Relationships Under Hydrostatic Stress for Their Use Under Nonhydrostatic Conditions. *74<sup>th</sup> Annual International Meeting, SEG, Expanded Abstracts*, 1689-1701.

- Reddy, J.N., 2004. An Introduction to Nonlinear Finite Element Analysis. Oxford University Press.
- Sayers, C.M. and Kachanov, M., 1991. A Simple Technique for Finding Effective Elastic Constants of Fractured Solids for Arbitrary Fracture Orientation Statistics. *International Journal of Solids and Structures*, 12, 81–97.
- Sayers, C.M., 2002. Stress-Dependent Elastic Anisotropy of Sandstones. *Geophysical Prospecting*, 50, 85–95.
- Schoenberg, M. and Sayers, C.M., 1995. Seismic Anisotropy of Fractured Rock. *Geophysics*, 60, 204–211.
- Shi, G. and Goodman, R.E., 1984. Discontinuous Deformation Analysis. *Proceedings of the 25 U.S. Symposium on Rock Mechanics*. New York, 269-277.
- Shi, G., 1988. Discontinuous Deformation Analysis: A New Numerical Model for the Statics and Dynamics of Locked Systems. Ph.D. thesis, University of California, Berkeley.
- Singh, B. (1973), "Continuum Characterization of Jointed Rock Masses. Part I - The Constitutive Equations", *Int. J. Rock Mech. Min. Sci. Geomech.*, 10, 311-335.
- Sun, D., Sone, H., Lin, W., Cui, J., He, B., Lv, H., and Cao, Z., 2017. Stress State measured at ~7km Depth in the Tarim Basin, NW China. *Scientific Reports* 7, 4503.
- Terzaghi, R.D., 1965. Sources of Error in Jointed Surveys. *Geotechnique* 15, 287-304.
- Trice, R., 1999. Application of Borehole Image Logs in Constructing 3D Static Models of Productive Fracture Networks in the Apulian Platform, Southern Apennines. Borehole Imaging: Application and Case Histories. London: Geological Society. Special Publications, 159, 155-176.

- Wang, Z., Su, J., Zhu, G., Han, J., and Wang, Y., 2013. Characteristics and Accumulation Mechanism of Quasi-Layered Ordovician Carbonate Reservoirs in the Tazhong Area, Tarim Basin. *Energy Exploration & Exploitation*, 31, 545-567.
- Williams, J.R. and Mustoe, G.W., 1993. *Proceedings of the Second International Conference on Discrete Element Methods*, Santa Fe, New Mexico.
- Yoshinaka, R. and Yamabe, T., 1986. Joint Stiffness and the Deformation Behavior of Discontinuous Rocks. *International Journal of Rock Mechanics and Mining Sciences & Geomechanics Abstracts*, 23(1), 19-28.
- Yoshioka, N. and Scholz, C.H. 1989. Elastic Properties of Contacting Surfaces Under Normal and Shear Loads 2. Comparison of Theory with Experiment. *J. Geophys. Res.* 94(B12), 17691-17700.
- Yossef, H.H., Ma, G., Shi, G., 2018. Discontinuous Deformation Analysis in Rock Mechanics Practice. *ISRM Book Series* Vol 5. London, Taylor & Francis Group.
- Zienkiewicz, O.C., Pande, G.N., 1977. Time-Dependent Multilaminate Model of Rocks-a Numerical Study of Deformation and Failure of Rock Masses. London, John Wiley.
- Zimmerman, R.W., 2012. The History and Role of the Cubic Law for Fluid Flow in Fractured Rocks. Presented at 2012 AGU Fall Meeting.
- Zhang, S.C., Liang, D.G., Zhu, G.Y., Zhang, X.Y., Zhang, B.M., Chen, J.P., and Zhang, B., 2007. Fundamental Geological Elements for the Occurrence of Chinese Marine Oil and Gas Accumulations. *Chinese Science Bulletin* 52, 28-43.
- Zhao, Y. and Chen, M., 2006. Fully Coupled Dual-Porosity Model for Anisotropic Formations. *Int. J. Rock Mech. Min. Sci.* 43, 1128-1133.

Zoback, M.D., Moos, D., Mastin, L., 1985. Well Bore Breakouts and in Situ Stress. *J. Geophys. Res.* 90(B7), 5523-5530



## APPENDIX A

### DERIVATION OF STRESS DISTRIBUTION AROUND A BOREHOLE

The analytical stress solutions around a cylindrical hole in an anisotropic elastic material was solved by Lekhnitskii (1963) and Amadei (1983). The final solutions of the stress are composed of two parts, one from the far field stresses, and one from stress induced from removing the cylindrical material.

Generalized plane strain condition is assumed. In this assumption the first derivatives of displacements in the axial direction are zeros,

$$\frac{\partial u}{\partial z} = \frac{\partial v}{\partial z} = \frac{\partial w}{\partial z} = 0 \quad (A - 1)$$

indicating  $\varepsilon_{zz} = 0$ .

Now we define  $A$  as the compliance tensor in borehole coordinate system, the constitutive relation relates the strain and stress components in borehole coordinate system as,

$$\begin{bmatrix} \varepsilon_{xx} \\ \varepsilon_{yy} \\ 0 \\ \gamma_{yz} \\ \gamma_{xz} \\ \gamma_{xy} \end{bmatrix} = \begin{bmatrix} a_{11} & a_{12} & a_{13} & a_{14} & a_{15} & a_{16} \\ a_{21} & a_{22} & a_{23} & a_{24} & a_{25} & a_{26} \\ a_{31} & a_{32} & a_{33} & a_{34} & a_{35} & a_{36} \\ a_{41} & a_{42} & a_{43} & a_{44} & a_{45} & a_{46} \\ a_{51} & a_{52} & a_{53} & a_{54} & a_{55} & a_{56} \\ a_{61} & a_{62} & a_{63} & a_{64} & a_{65} & a_{66} \end{bmatrix} \begin{bmatrix} \sigma_{xx} \\ \sigma_{yy} \\ \sigma_{zz} \\ \tau_{yz} \\ \tau_{xz} \\ \tau_{xy} \end{bmatrix} \quad (A - 2)$$

The equilibrium equations are given as:

$$\frac{\partial \sigma_{xx}}{\partial x} + \frac{\partial \tau_{xy}}{\partial y} = 0 \quad (A - 3)$$

$$\frac{\partial \sigma_{yy}}{\partial y} + \frac{\partial \tau_{xy}}{\partial x} = 0 \quad (A - 4)$$

$$\frac{\partial \tau_{xz}}{\partial x} + \frac{\partial \tau_{yz}}{\partial y} = 0 \quad (A - 5)$$

and compatibility equations:

$$\frac{\partial^2 \varepsilon_{xx}}{\partial y^2} + \frac{\partial^2 \varepsilon_{yy}}{\partial x^2} = \frac{\partial^2 \gamma_{xy}}{\partial x \partial y} \quad (A-6)$$

$$\frac{\partial \gamma_{zx}}{\partial y} - \frac{\partial \gamma_{yz}}{\partial x} = 0 \quad (A-7)$$

To derive the solution of the stresses, we define two stress functions,  $F(x, y)$  and  $G(x, y)$  which satisfy the equilibrium equations and are related to the stress components as,

$$\sigma_{xx} = \frac{\partial^2 F}{\partial y^2} \quad (A-8)$$

$$\sigma_{yy} = \frac{\partial^2 F}{\partial x^2} \quad (A-9)$$

$$\tau_{xy} = \frac{\partial^2 F}{\partial x \partial y} \quad (A-10)$$

$$\tau_{xz} = \frac{\partial G}{\partial y} \quad (A-11)$$

$$\tau_{yz} = \frac{\partial G}{\partial x} \quad (A-12)$$

Substituting Equations A-8 to A-12 into A-2, the strain terms can be then expressed as stress functions  $F(x, y)$  and  $G(x, y)$ . If the strain components are further substitute into the compatibility equations A-6 and A-7, two sets of coupled differential equations can be obtained,

$$(L_4 L_2 - L_3^2)F = 0 \quad (A-13)$$

$$(L_3^2 - L_4 L_2)G = 0 \quad (A-14)$$

where  $L_2$ ,  $L_3$ , and  $L_4$  are the differential operators,

$$L_2 = \beta_{44} \frac{\partial^2}{\partial x^2} - 2\beta_{45} \frac{\partial^2}{\partial x \partial y} + \beta_{55} \frac{\partial^2}{\partial y^2} \quad (A-15)$$

$$L_3 = -\beta_{24} \frac{\partial^3}{\partial x^3} + (\beta_{25} + \beta_{46}) \frac{\partial^3}{\partial x^2 \partial y} - (\beta_{14} + \beta_{56}) \frac{\partial^3}{\partial x \partial y^2} + \beta_{15} \frac{\partial^3}{\partial y^3} \quad (A-16)$$

$$L_4 = \beta_{22} \frac{\partial^4}{\partial x^4} - 2\beta_{26} \frac{\partial^4}{\partial x^3 \partial y} + (2\beta_{12} + \beta_{66}) \frac{\partial^4}{\partial x^2 \partial y^2} - 2\beta_{16} \frac{\partial^4}{\partial x \partial y^3} + \beta_{11} \frac{\partial^4}{\partial y^4} \quad (A-17)$$

where  $\beta_{ij}$  is defined as,

$$\beta_{ij} = a_{ij} - \frac{a_{i3}a_{j3}}{a_{33}} \quad (A-18)$$

Using the method of characteristics, a general solution of the coupled Equation A-13 and A-14 can be found. Substituting  $e^{x+\mu y}$  for the stress function  $F(x, y)$  into Equation A-13 and A-14, the resulting algebraic equation after differentiation is,

$$L_4(\mu)L_2(\mu) - L_3(\mu)^2 = 0 \quad (A-19)$$

where,

$$L_2(\mu) = \beta_{44} - 2\beta_{45}\mu + \beta_{55}\mu^2 \quad (A-20)$$

$$L_3(\mu) = -\beta_{24} + (\beta_{25} + \beta_{46})\mu - (\beta_{14} + \beta_{56})\mu^3 + \beta_{15}\mu^3 \quad (A-21)$$

$$L_4(\mu) = \beta_{22} - 2\beta_{26}\mu + (2\beta_{12} + \beta_{66})\mu^2 - 2\beta_{16}\mu^3 + \beta_{11}\mu^4 \quad (A-22)$$

Equation A-19 always has six complex or purely imaginary roots  $\mu_i$ , where three roots are always conjugate to the others. Lekhnitskii (1963) has shown that general expressions for the stress functions  $F$  and  $G$  can be found as,

$$F = 2Re(F_1(z_1) + F_2(z_2) + F_3(z_3)) \quad (A-23)$$

$$G = 2Re\left(\lambda_1 F'_1(z_1) + \lambda_2 F'_2(z_2) + \frac{1}{\lambda_3} F'_3(z_3)\right) \quad (A-24)$$

where  $F_i(z_i)$  is an analytical function of the complex coordinates  $z_i = x_i + \mu_i y_i$ , and  $F'_i(z_i)$  is the derivative of  $F_i(z_i)$  with respect to  $z_i$ . The coefficients  $\lambda_i$  are defined as,

$$\lambda_1 = -\frac{l_3(\mu_1)}{l_2(\mu_1)} \quad (A-25)$$

$$\lambda_2 = -\frac{l_3(\mu_2)}{l_2(\mu_2)} \quad (A-26)$$

$$\lambda_3 = -\frac{l_3(\mu_3)}{l_4(\mu_3)} \quad (A-27)$$

Substituting the general stress functions in Equations A-23 and A-24 into equations A-8 to A-12 yields the expressions for the borehole-induced stresses  $\sigma^{b,i}$ . With the far field stress components in the borehole coordinate system, the final form of the stress expressions around a borehole in an anisotropic formation are,

$$\sigma_{xx}^{b,ani} = \sigma_{xx}^b + \sigma_{xx}^{b,i} = \sigma_{xx}^b + 2\text{Re}[\mu_1^2 \phi_1'(z_1) + \mu_2^2 \phi_2'(z_2) + \lambda_3 \mu_3^2 \phi_3'(z_3)] \quad (A-28)$$

$$\sigma_{yy}^{b,ani} = \sigma_{yy}^b + \sigma_{yy}^{b,i} = \sigma_{yy}^b + 2\text{Re}[\phi_1'(z_1) + \phi_2'(z_2) + \lambda_3 \phi_3'(z_3)] \quad (A-29)$$

$$\tau_{xy}^{b,ani} = \tau_{xy}^b + \tau_{xy}^{b,i} = \tau_{xy}^b - 2\text{Re}[\mu_1 \phi_1'(z_1) + \mu_2 \phi_2'(z_2) + \lambda_3 \mu_3 \phi_3'(z_3)] \quad (A-30)$$

$$\tau_{xz}^{b,ani} = \tau_{xz}^b + \tau_{xz}^{b,i} = \tau_{xz}^b + 2\text{Re}[\lambda_1 \mu_1 \phi_1'(z_1) + \lambda_2 \mu_2 \phi_2'(z_2) + \mu_3 \phi_3'(z_3)] \quad (A-31)$$

$$\tau_{yz}^{b,ani} = \tau_{yz}^b + \tau_{yz}^{b,i} = \tau_{yz}^b - 2\text{Re}[\lambda_1 \phi_1'(z_1) + \lambda_2 \phi_2'(z_2) + \phi_3'(z_3)] \quad (A-32)$$

$$\sigma_{zz}^{b,ani} = \sigma_{zz}^b - \frac{1}{C_{33}}(C_{31}\sigma_{xx}^{b,i} + C_{32}\sigma_{yy}^{b,i} + C_{34}\tau_{yz}^{b,i} + C_{35}\tau_{yz}^{b,i} + C_{36}\tau_{xy}^{b,i}) \quad (A-33)$$

where  $\phi_i'$  are the derivatives of three analytical equations,

$$\begin{aligned} \phi_1'(z_1) = & \gamma_1[(\mu_3 \lambda_2 \lambda_3 - \mu_2)(\sigma_{yy}^b - i\tau_{xy}^b - P_w) + (\lambda_2 \lambda_3 - 1)(\tau_{xy}^b - i\sigma_{xx}^b + iP_w) \\ & + \lambda_3(\mu_3 - \mu_2)(\tau_{yz}^b - i\tau_{xz}^b)] \end{aligned} \quad (A-34)$$

$$\begin{aligned} \phi_2'(z_2) = & \gamma_2[-(\mu_3 \lambda_1 \lambda_3 - \mu_1)(\sigma_{yy}^b - i\tau_{xy}^b - P_w) + (1 - \lambda_1 \lambda_3)(\tau_{xy}^b - i\sigma_{xx}^b + iP_w) \\ & + \lambda_3(\mu_1 - \mu_3)(\tau_{yz}^b - i\tau_{xz}^b)] \end{aligned} \quad (A-35)$$

$$\begin{aligned} \phi_3'(z_3) = & \gamma_3[(\mu_2 \lambda_1 - \mu_1 \lambda_2)(\sigma_{yy}^b - i\tau_{xy}^b - P_w) + (\lambda_1 - \lambda_2)(\tau_{xy}^b - i\sigma_{xx}^b + iP_w) \\ & + (\mu_2 - \mu_1)(\tau_{yz}^b - i\tau_{xz}^b)] \end{aligned} \quad (A-36)$$

where

$$\gamma_j = \left[ -2\Delta p_j \sqrt{\left(\frac{z_j}{a}\right)^2 - 1 - \mu_j^2} \right]^{-1} \quad (A - 37)$$

$$\Delta p_j = \frac{\frac{z_j}{a} + \sqrt{\left(\frac{z_j}{a}\right)^2 - 1 - \mu_j^2}}{1 - i\mu_j} \quad (A - 38)$$

and

$$\Delta = \mu_1 - \mu_2 + \lambda_2 \lambda_3 (\mu_1 - \mu_3) + \lambda_1 \lambda_3 (\mu_3 - \mu_2) \quad (A - 39)$$

From the constitutive relation C-2, the axial stress can be written as,

$$\sigma_{zz}^{b,ani} = \sigma_{xx}^b - \frac{1}{a_{33}} (a_{31}\sigma_{xx}^{b,i} + a_{32}\sigma_{yy}^{b,i} + a_{34}\tau_{yz}^{b,i} + a_{35}\tau_{yz}^{b,i} + a_{36}\tau_{xy}^{b,i}) \quad (A - 40)$$

## APPENDIX B

### STRESS TRANSFORMATIONS

In this section, the mathematical formulations to transform the stress from the principal stress directions to the wellbore directions are presented. First, stresses in the principal stress coordinate system are transformed to the global coordinate system as shown in Figure B1. The maximum horizontal principal stress  $\sigma_H$  is aligned with  $x_p$  axis, the minimum horizontal principal stress  $\sigma_h$  is aligned with  $y_p$  axis, and the vertical principal stress  $\sigma_v$  is aligned with  $z_p$  axis. The global coordinate system is defined that the north is in the positive direction of  $x_e$ , east is in the positive direction of  $y_e$ , and the positive direction of  $z_e$  is pointing downward.

$$\sigma_{GCS} = T_1^T \sigma_{PCS} T_1 \quad (B - 1)$$

where  $\sigma_{PCS}$  is the principal stress matrix,

$$\sigma_{PCS} = \begin{bmatrix} \sigma_h & 0 & 0 \\ 0 & \sigma_H & 0 \\ 0 & 0 & \sigma_v \end{bmatrix} \quad (B - 2)$$

and  $T_1$  is the transformation matrix from principal stress coordinate system to global coordinate system,

$$T_1 = \begin{bmatrix} \cos(\alpha_s) \cos(\beta_s) & \sin(\alpha_s) \cos(\beta_s) & \sin(\beta_s) \\ -\sin(\alpha_s) & \cos(\alpha_s) & 0 \\ -\cos(\alpha_s) \sin(\beta_s) & -\sin(\alpha_s) \sin(\beta_s) & \cos(\beta_s) \end{bmatrix} \quad (B - 3)$$

where  $\alpha_s$  is the azimuth of the maximum horizontal stress and  $\beta_s$  is the inclination angle between  $\sigma_v$  and  $z_e$  axis. Then we can transform the stress components from the global coordinate system to the borehole coordinate system as shown in Figure B1,

$$\sigma_{BCS} = T_2 \sigma_{GCS} T_2^T \quad (B - 4)$$

where  $\sigma_{GCS}$  is the defined as,

$$\sigma_{GCS} = \begin{bmatrix} \sigma_{xx} & \tau_{xy} & \tau_{xz} \\ \tau_{yx} & \sigma_{yy} & \tau_{yz} \\ \tau_{zx} & \tau_{zy} & \sigma_{zz} \end{bmatrix} \quad (B - 5)$$

and  $T_2$  is the transformation matrix from global coordinate system to borehole coordinate system,

$$T_2 = \begin{bmatrix} \cos(\alpha_b) \cos(\beta_b) & \sin(\alpha_b) \cos(\beta_b) & \sin(\beta_b) \\ -\sin(\alpha_b) & \cos(\alpha_b) & 0 \\ -\cos(\alpha_b) \sin(\beta_b) & -\sin(\alpha_b) \sin(\beta_b) & \cos(\beta_b) \end{bmatrix} \quad (B - 6)$$

where  $\alpha_b$  and  $\beta_b$  are the azimuth and inclined angle of the wellbore, and  $\sigma_{BCS}$  is denoted as,

$$\sigma_{BCS} = \begin{bmatrix} \sigma_{xx}^b & \tau_{xy}^b & \tau_{xz}^b \\ \tau_{yx}^b & \sigma_{yy}^b & \tau_{yz}^b \\ \tau_{zx}^b & \tau_{zy}^b & \sigma_{zz}^b \end{bmatrix} \quad (B - 7)$$

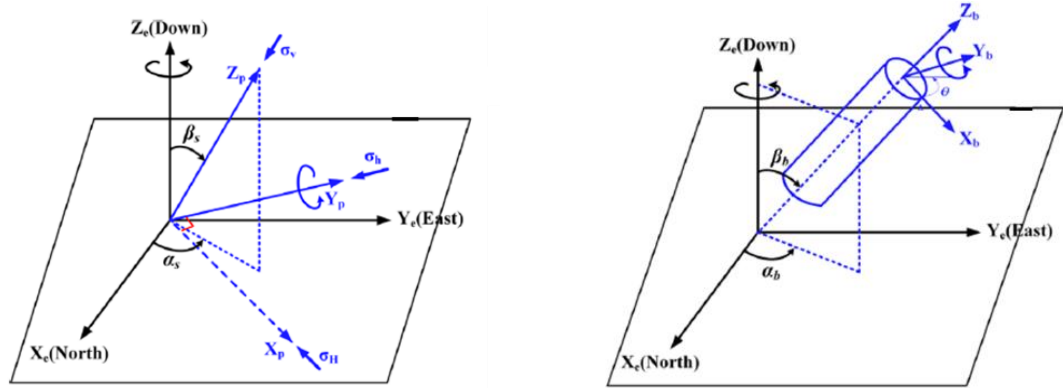


**Figure B1 – Illustration of coordinate system transformation from the principal stress coordinate system to the global coordinate system (left), and from the global coordinate system to borehole coordinate system(right)**